Signal Processing using Nonlinear Optical Eects in Single- and Few-Mode Fibers

Friis, Søren Michael Mørk; Rottwitt, Karsten

Publication date:
2016

Document Version
Publisher's PDF, also known as Version of record

DTU Fotonik
Department of Photonics Engineering

Signal Processing using Nonlinear Optical Effects in Single- and Few-Mode Fibers

PhD Thesis

Søren Michael Mørk Friis
Fiber Optics, Devices and Non-Linear Effects
Department of Photonics Engineering
Technical University of Denmark

August 30, 2016

Contents

Preface

This thesis is submitted in candidacy for the PhD degree at Technical University of Denmark (DTU). The project has been carried out between 2013 and 2016 at the Department of Photonics Engineering at DTU (DTU Fotonik) with Prof. Karsten Rottwitt as the main supervisor. The project has contributed to two fields of research but only the part concerning nonlinear optical effects in fibers is the subject of this thesis; the list of publications shows a number of works related to light propagation through diatom frustules, the other part of the project.

Four months work from October 2015 through January 2016 was carried out as a visiting student researcher at the Opto-Electronics Research Centre (ORC) at University of Southampton under supervision of Dr. Francesca Parmigiani and Prof. David J. Richardson; close collaboration with the ORC has remained during the rest of the project.

Acknowledgments

Firstly, I would like to thank my supervisor, Karsten Rottwitt, for encouraging me all the way through the PhD program at DTU Fotonik and even more for always giving me his time to discuss ideas, calculations, and physics (and the nature of drunk sailors upon the island where we are both born). Secondly, I'm very thankful to the people at ORC for giving me a warm welcome and namely to Peter Horak and John Begleris for helping me with theory and Yongmin Jung for his valuable assistance in the lab; I also wish to give a special thanks to Francesca Parmigiani for acting as my unofficial supervisor and for helping me extensively in the lab.

A number of people helped me on daily basis or occasionally with my research, whom I also wish to express gratitude to; among them are Lasse Mejling, Mario A. Usuga, Colin J. McKinstrie, Christian Maibohm, Yanyan Su, Marianne Ellegaard, Nina Lundholm, and especially Erik N. Christensen and Jacob G. Koefoed who did the actual measure-

ments that I included in this thesis in Sec. 4.4.

A final thanks goes to my dear girlfriend, Anine, who through three years has patiently listened to frustrated tales of miscarried calculations and experiments without giving away a single sign of boredom.

Søren M. M. Friis

Abstract

The stagnating increase in data transmission capacity in optical communication systems combined with the ever growing demand of transmission bandwidth is leading to an impending capacity crunch, referring to the point in time after which the available bandwidth of the individual user starts to decrease. To postpone this point in time, existing technologies in terms of data transmission through optical fibers must be optimized and new degrees of freedom must be introduced to continue the exponential increase in available bandwidth; space-division multiplexing is believed to be the strongest candidate for another degree of freedom in transmission fibers.

This thesis is two-fold: firstly, starting at Maxwell's equations and basic principles of quantum mechanics, a semi-classical model of the noise properties of fiber optical parametric amplifiers and frequency converters is presented. The model accounts for multiple effects present in nonlinear fibers such as four-wave mixing, Raman scattering, distributed loss, and dispersion, and it is valid in the depleted pump regime. After validating the model against well-known results of quantum models, the model is used to predict the impacts of Raman noise, loss, and pump depletion on the noise properties of parametric frequency conversion and phase-insensitive and phase-sensitive parametric amplification.

An important part of realizing space-division multiplexing is the ability of optical signal processing so the second part of this thesis addresses few-mode Raman fiber amplifiers and parametric amplifiers and frequency converters. A model of weak random linear mode coupling in the pump of a two-mode distributed Raman fiber amplifier is presented and it is shown that an amplification noise figure induced by mode coupling increases with the degree of mode coupling and that this tendency increases as the pump depletes. Also, a very low mode-dependent gain of 0.25 dB per 10 dB gain is experimentally demonstrated in a two-mode distributed Raman fiber amplifier by exciting the pump in a combination of two modes.

A comprehensive model of four-wave mixing in two-mode fibers ac-

counting for six simultaneous processes is derived, and the conversion efficiency from signal to idler in the four-wave mixing processes of phase conjugation and Bragg scattering in two two-mode fibers with different phase matching properties are experimentally investigated. A conversion efficiency of > -2.70 dB is demonstrated for Bragg scattering in the conversion of a signal in the LP01-mode to the idler in the LP11-mode; the signal-to-idler separation is ~ 25 nm. Good qualitative agreement between experiments and theory is found for both processes in both fibers.

Resume (in danish)

Den stagnerende forøgelse af datatransmissionskapacitet i optiske kommunikationssystemer kombineret med den stadigt stigende efterspørgsel på transmissionsbåndbredde er ved at føre til et forestående kapacitetsnedbrud, med hvilket menes det tidspunkt, hvorefter den enkelte brugers tilgængelige båndbredde begynder at falde. For at udskyde dette tidspunkt bør eksisterende teknologier i form af dataoverførsel i optiske fibre optimeres, og nye frihedsgrader skal indføres for at fortsætte den eksponentielle stigning i tilgængelig båndbredde; rum-fordelt multioverføring[1] menes at være den stærkeste kandidat til en ny frihedsgrad i transmissionsfibre.

Denne afhandling har to fokuspunkter. Det første, som starter ved Maxwells ligninger og grundlæggende kvantemekaniske principper, er en præsentation af en semi-klassisk model for støjegenskaberne af fiberoptiske parametriske forstærkere og frekvensomformere. Modellen tager højde for flere effekter, som er til stede i ikke-lineære fibre, såsom fire-bølgeblanding, Raman spredning, distribueret tab, og dispersion, og den er gyldig i det regime, hvor pumpen mætter. Efter validering af modellen imod kendte kvantemekaniske resultater er modellen anvendt til at forudsige virkningerne af Raman støj, tab, og pumpemætning på støjegenskaberne i parametrisk frekvenskonvertering og fase-ufølsom og fase-følsom parametrisk forstærkning.

En vigtig del af realiseringen af rum-fordelt multioverføring er muligheden for optisk signalbehandling, så den anden del af denne afhandling omhandler Raman fiber forstærkere og parametriske forstærkere og frekvensomformere i fibre med få tilladte optiske tilstande.[2] En model for svag tilfældig lineær kobling mellem optiske tilstande i pumpen i en distribueret Raman fiber forstærker med to tilladte optiske tilstande præsenteres, og det er vises, at et forstærkningsstøjtal fremkaldt af kobling mellem optiske tilstande stiger med graden af tilstandskobling, og

[1] Det engelske *space-division multiplexing* er oversat til rum-fordelt multioverføring.
[2] Det engelske begreb *mode* er her oversat til en *optisk tilstand*

at denne tendens øges i takt med, at pumpen mættes. Desuden påvises en meget lav tilstandsafhængig forstærkning på 0.25 dB pr 10 dB forstærkning eksperimentelt i en distribueret Raman fiber forstærker med to tilladte optiske tilstande med pumpen fordelt i en kombination af to optiske tilstande.

En omfattende model af fire-bølgeblanding i fibre med to tilladte tilstande, der tager højde for seks samtidige processer udledes, og overføringsgraden fra signal til *idler*[3] i de to fire-bølgeblandingsprocesser, fasekonjugering og Bragg-spredning, i to fibre med forskellige fasetilpasningsegenskaber bliver eksperimentelt undersøgt. En overføringsgrad på > -2.70 dB demonstreres for Bragg-spredning i overføringen af et signal i LP01-tilstanden til *idleren* i LP11-tilstanden. Signal-*idler* adskillelsen er ~ 25 nm. God kvalitativ overensstemmelse mellem eksperimenter og teori vises for begge processer i begge fibre.

[3] *idler* (den dovne) er det engelske begreb for en bølge som dannes i fire-bølgeblandingsprocessen som følge af energibevarelse.

List of publications

The basis of the thesis

Journal publications

[1] S. M. M. Friis, L. Mejling, and K. Rottwitt, "Effects of Raman scattering and attenuation in silica fiber-based parametric frequency conversion," in preparation for Opt. Express (2016).

[2] S. M. M. Friis, Y. Jung, I. Begleris, P. Horak, K. Rottwitt, P. Petropoulos, D. J. Richardson, and F. Parmigiani, " IMFWM paper," in preparation for Opt. Express (2016).

[3] S. M. M. Friis and K. Rottwitt, "Noise Contributions of Linear Pump Mode Coupling in Few-Mode Raman Fiber Amplifiers," Submitted to J. Lightwave Technol., Aug. (2016).

[4] E. N. Christensen, J. G Kofoed, S. M. M. Friis, M. A. Usuga, and K. Rottwitt, "Experimental characterization of Raman overlaps between mode-groups," Submitted, revised and re-submitted to Scientific Reports (2016).

[5] S. M. M. Friis, K. Rottwitt, and C. J. McKinstrie, "Raman and loss induced quantum noise in depleted fiber optical parametric amplifiers," Opt. Express **21,** 29320–29331 (2013)

The two papers that are submitted to journals are attached in Appendix B and C, respectively.

Conference proceedings

[6] F. Parmigiani, Y. Jung, S. M. M. Friis, Q. Kang, I. Begleris, P. Horak, P. Petropoulos, K. Rottwitt, and D. J. Richardson, "Study of Inter-Modal Four Wave Mixing in Two Few-Mode Fibres with Different Phase Matching Properties," Proceedings of European Conference on Optical Communication, Tu2D.4 (2016).

[7] S. M. M. Friis, Y. Jung, I. Begleris, P. Horak, K. Rottwitt, P. Petropoulos, D. J. Richardson, and F. Parmigiani, "Detailed phase matching char-

acterization of inter-modal four-wave mixing in a two-mode fiber," Proceedings of CLEO, JTu5A.49 (2016).

[8] I. Begleris, S. M. M. Friis, F. Parmigiani, and P. Horak "Conversion efficiency and bandwidth of inter-modal four wave mixing in two-mode optical fibres," Accepted at Photon 16, University of Leeds (20016).

[9] K. Rottwitt, K. Nielsen, S. M. M. Friis, and M. A. Usuga, "Challenges in higher order mode Raman amplifiers," OFC Technical Digest, Tu3C.6 (2015).

[10] S. M. M. Friis, L. Mejling, and K. Rottwitt, "Reducing Raman noise in parametric frequency conversion by varying the input pump power," in Advanced Photonics, OSA Technical Digest, NW4A.6 (2014).

[11] S. M. M. Friis, L. Mejling, M. A. Usuga, A. T. Pedersen, C. J. McKinstrie, and K. Rottwitt, "Effects of Raman scattering in quantum state-preserving frequency conversion," in CLEO: 2014, OSA Technical Digest, STu2I.2 (2014).

[12] S. M. M. Friis and K. Rottwitt, "Raman and loss induced quantum noise in a depleted phase-sensitive parametric amplifier," Proceedings of Australian and New Zealand Conference on Optics and Photonics (2013).

[13] S. M. M. Friis, K. Rottwitt, and C. J. McKinstrie, "Quantum and Raman Noise in a Depleted Fiber Optical Parametric Amplifier," Nonlinear Optics Technical Digest, NW4A.06 (2013).

Publications outside the scope of the thesis

Journal publications

[14] M. Ellegaard, T. Lenau, N. Lundholm, C. Maibohm, S. M. M. Friis, K. Rottwitt, and Y. Su, "The fascinating diatom frustule—can it play a role for attenuation of UV radiation?," Journal of Applied Phycology (2016).

[15] C. Maibohm, S. M. M. Friis, M. Ellegaard, K. Rottwitt, "Interference patterns and extinction ratio of the diatom Coscinodiscus *granii*," Opt. Express **23,** 9543–9548 (2015).

[16] Y. Su, N. Lundholm, S. M. M. Friis, and M. Ellegaard, "Implications for photonic applications of diatom growth and frustule nanostructure changes in response to different light wavelengths," Nano Research **8,** 2363–2372 (2015).

Conference proceedings

[17] C. Maibohm, S. M. M. Friis, and K. Rottwitt, "Comparing optical properties of different species of diatoms," Proceedings of SPIE, 93600B (2015).

[18] L. Mejling, S. M. M. Friis, D. V. Reddy, K. K. Rottwitt, M. G. Raymer, and C. J. McKinstrie, "Asymmetrically Pumped Bragg Scattering with the Effects of Nonlinear Phase Modulation," in Advanced Photonics, JTu3A.36 (2014).

[19] Y. Su, N. Lundholm, S. M. M. Friis, and M. Ellegaard, "Diatom elemental and frustule nanostructure changes in response to different light wavelengths," Proceedings of 23rd International Diatom symposium (2014).

Chapter 1

Introduction and motivation

During the past three decades, most of the world has undergone dramatic changes that have affected how people live their lives [1], one of the most important reasons being the development of the internet, which has made possible a number of applications that today seem impossible to live without: instant global communication, globalized economy and markets, social media, access to information and education in the developing world, and instantaneous distribution of all kinds of digital products such as software, banking, music and television. These highly valued services consists of many layers of technology but the physical infrastructure that binds the whole together today is fiber-optical communication.

Since the 1980's, information capacity in optical single-mode fibers has grown exponentially but during the most recent decade, the increase in capacity has started to saturate [2]. The reason is that the rate of data transmission is approaching the theoretical capacity limit of single-mode silica fibers, the nonlinear Shannon limit, which is a trade-off between maximizing capacity with as high a signal-to-noise ratio as possible and the penalties of nonlinear effects [3]. The combination of the stagnation in the increase of bandwidth supply and the ever growing demand eventually leads to the so-called capacity crunch [2, 4, 5], referring to the point in time after which the available bandwidth of the individual user starts to decrease. While the time horizon for the coming capacity crunch remains unknown [5] it is clear that new technologies for increasing transmission capacity must be developed.

The remainder of this introductory chapter motivates and puts this thesis into context: the basic components of an optical communication

system is presented with focus on fiber optical amplifiers and frequency converters, which are the topics of this thesis, and space-division multiplexing is introduced and the important properties of multi-mode amplifiers are emphasized.

1.1 Components of an optical communication system

Figure 1.1 shows a diagram of an optical communication system: a fiber-coupled light source provides coherent light at one or several wavelengths in the communication band (around 1550 nm); several wavelengths can be achieved from the same source by exploiting super continuum generation [6] or optical frequency combs [7,8]. A modulator applies data from the electrical domain to the optical domain using a chosen modulation format [9, 10]; intensity modulation formats encode the information by modulating the amplitude of the transmitted light and differential phase shift keyed modulation formats rely on a phase shift to distinguish 1's and 0's. Higher order modulation formats such as quadrature-amplitude modulation enables transmitting more than one bit per symbol. Before transmission, an optical amplifier, shown as the gray optical processing unit in Fig. 1.1, may be employed to reach high enough power that the signal can travel a long distance before regeneration or detection.

The modulated optical signal is then transmitted through extremely low-loss fibers (about 0.2 dB/km) towards its destination, which may be a few or thousands of kilometers away. Despite the low loss, the optical signal must be amplified or regenerated every 50–100 km [11] by either optical amplifiers or optical-electrical-optical repeaters. Since the invention of the Erbium-doped fiber amplifier (EDFA) in the 1990's repeaters are not as widely used due to the difficulties of operating them in wavelength-division multiplexed (WDM) systems and their high implementation costs. However, all amplifiers add excess noise to the amplified signal so in long-haul transmission the signal-to-noise ratio of any transmission eventually becomes too low for efficient detection and therefore a repeater must be used to regenerate the signal.

In addition to amplification, optical processing units may perform other tasks of interest in optical communication systems: wavelength conversion is a critical feature of WDM networks because a signal often has to pass through multiple network nodes on its way to its destination; however, the same wavelength channel may not be available between all nodes so fast and efficient wavelength conversion is desirable [12, 13]. Also, performance monitoring is important for amplifier control, channel

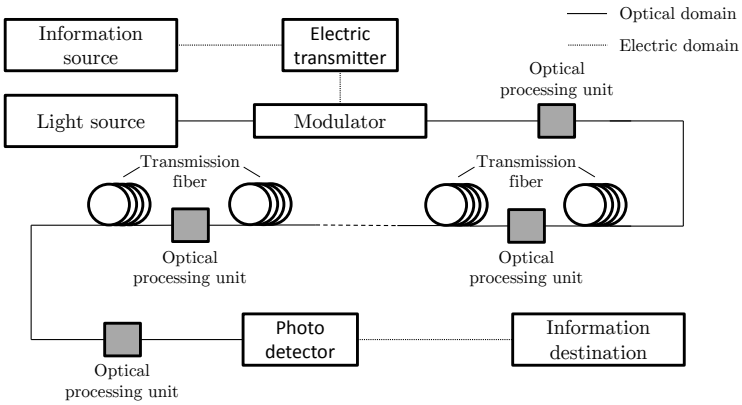

Fig. 1.1: Illustration of an optical communication system; the gray boxes are optical processing units, which are the focus of this thesis, and they may be amplifiers, repeaters, wavelength converters, or monitors.

identification, and signal quality assessment [14].

This thesis focuses on all-optical silica-based fiber signal processing units for optical communication, illustrated as the gray boxes in Fig. 1.1. The advantages of fiber-based solutions, compared to a chip-based Silicon or Aluminum arsenide solutions, are that optical signals arrive by fiber, which means that the signal is properly mode-matched to the fiber-based processing unit, thus reducing transition losses; secondly, drawing silica fibers is a mature technology that facilitates extremely low-loss fibers with high uniformity. As already mentioned, signal processing units may serve a number of purposes but this thesis studies only optical amplification and frequency conversion.

1.1.1 Optical fiber amplifiers

Three kinds of fiber optical amplifiers are available today: EDFAs, Raman amplifiers, and four-wave mixng (FWM) based parametric amplifiers. EDFAs offer high gain in a broad band in the low-loss window of silica fibers around wavelengths of 1550 nm [15] and are thus the most widely used fiber amplifier toady. Raman fiber amplifiers do not require doping in the fiber medium and is therefore used in a distributed configuration where stimulated Raman scattering compensates for fiber loss through the whole transmission fiber; this configuration has superior noise properties compared to discrete EDFAs [16]. Also, Raman amplifiers are not bound to a specific band but amplifies in a broad band at a certain frequency shift below the pump; 13.2 THz for silica fibers.

Fiber-opical parametric amplifers (FOPAs) offer a wide bandwidth

of high optical amplification [17, 18]. Some of the advantages of FOPAs are that the gain spectrum shape can be varied depending on the fiber dispersion properties and that the center frequency correspondingly can be decided through fiber design [19]; operated in a dual pump scheme, the optical gain can be made constant over a much wider bandwidth than EDFAs [20–23]; FOPAs can be operated both phase-insensitively and phase-sensitively [17, 24]; and finally, due to the ultra-fast response of the Kerr nonlinearity all of these properties are conserved even at high signal rates in the THz regime, which additionally enables the FOPA to effectively become an optical processing unit, e.g. ultra-fast monitor or switch.

FOPAs have been demonstrated to have excellent noise properties; a noise figure (NF) of 3.7 dB has been measured in a phase-insensitive amplifier (PIA) at $\sim$ 10 dB gain [25] and another NF of 3.8 dB was measured at 40 dB gain [26]. PIAs are limited by a 3-dB quantum induced NF [27] and the extra noise contribution in these measurements are from pump transferred noise and spontaneous Raman scattering [28]. To understand these excess noise sources, quantum models have been developed [29–32] but none of these models take into account all effects of dispersion, loss, Raman scattering, pump noise, and the depleted pump regime; therefore, one must rely on semi-classical models to get a full picture; an example is seen in Ref. [33]. Such a semi-classical model that describes all these effects is presented in Ch. 3 in this thesis.

1.1.2 Fiber parametric frequency conversion

Parametric processes in fibers also offer the possibility for frequency conversion in both the classical and the quantum regime [29, 34, 35]. The generation of the idler in the amplification process of FOPAs is sometimes in the literature referred to as frequency conversion [31, 36] but the processes does not create the idler to be a copy of the input signal but a copy of the output signal, both in terms of amplitude and noise statistics. Frequency conversion, in which the output idler is a copy of the input signal, is achieved by using a fundamentally different wave configuration, which is called Bragg scattering (BS) in the literature and has a special property: no additional noise is associated with the BS process, which means that the output idler is copy of the input signal [30]; the latter has the inherent property that BS enables frequency conversion of quantum states of light without altering the other quantum properties of the state [34]. However, the quantum descriptions behind this prediction do not take into account fiber loss and Raman scattering, just as is the case of the FOPA, so another of the goals of the semi-

classical model of Ch. 3 in this theses is to quantify how these effects distort the BS process.

The good noise properties of BS are widely recognized, and BS has been investigated experimentally through the last decade: 180 nm signal conversion has been shown [37] and it has indeed been demonstrated that BS has superior noise properties over frequency conversion by amplification [38] in the classical regime; in the quantum regime, frequency conversion of weak coherent states has been done using BS but Raman noise contaminates the purity of the conversion [39–41].

1.1.3 Multi-mode fiber amplifiers

Data transmission in single-mode and single-core fibers today use all degrees of freedom to maximize capacity; wavelength, polarization, amplitude, and phase. Hence, to continue the exponential growth in capacity new degrees of freedom must be introduced [42]; space-division multiplexing (SDM) is considered the foremost candidate for increasing the capacity per fiber [43]. SDM refers to using space to distinguish separate channels in shape of either parallel cores in the same fiber or a single core guiding multiple spatial modes; one crucial demand for SDM is that the cost per bit must be lower than simply distributing parallel fibers [44].

The realization of SDM is dependent on the ability to optically amplify transmission signals, and multi-mode fiber amplifiers are believed to be more pump power efficient than multi-core fiber amplifiers due to the denser packing of the fiber modes [45]. Equal gain in all modes is desirable [46] and it has already been demonstrated that it is possible to tailor both fiber design and pump power distribution among modes of Erbium-doped fiber amplifiers (EDFAs) to reduce mode-dependent gain [47] and indeed EDFAs with low mode-dependent gain has been demonstrated [48]. Also, few-moded distributed Raman fiber amplifiers have been used to compensate for fiber loss in a two-mode fiber with low mode-dependent gain by pumping in a higher order fiber mode [49]. It has been suggested that mode-equalized gain can be minimized in few-mode Raman fiber amplifiers by designing the transverse doping profile [50] or by pumping in a combination of modes [51]. The latter problem is addressed in Ch. 4 of this thesis where a record low mode-dependent gain is achieved experimentally by pumping in a specific combination of mode in a two-mode fiber. Another challenge of mode-multiplexed systems is random linear mode coupling; deterministic mode coupling can be mitigated by multiple-input-multiple-output techniques [52] but random mode coupling introduces a new source of

noise. Chapter 4 of this thesis also investigates the impact of weak random linear mode coupling in the pump of a two-mode Raman fiber amplifier.

On top of the advantageous pump power budget, multi-mode fibers also allow for nonlinear interaction among spectrally well separated wavelength components through FWM [53] due to the different propagation constants of the fiber modes. This property is interesting for optical communication because, as mentioned above, the noise properties of FOPAs are limited by pump transferred noise and Raman scattering. If the pumps and signals could be separated spectrally, the contributions from these noise source could be reduced. Also, quantum state preserving frequency conversion could be realized by using BS as already demonstrated in a dispersion shifted single-mode fiber over 4.7 nm [54]; multe-mode FWM could potentially enable much larger shifts. This thesis addresses multi-mode FWM in Ch. 5 both theoretically and experimentally and presents investigations of phase matching bandwidths of two inter-modal FWM processes in two different two-mode fiber.

1.2 Structure of thesis

The rest of the thesis is structures as follows:

Chapter 2 is an introduction to the theory that is needed as background for the rest of the thesis; Maxwell's equations are stated and the electric field and induced polarization are defined. The chapter provides a detailed review of how Maxwell's equations are manipulated to calculate both full vectorial and linearly polarized modes, and the modal properties of weakly guiding fibers are derived in the scalar regime. Further, a general nonlinear propagation equation for a continuous wave field in a specified mode is derived in detail.

Chapter 3 presents a semi-classical model of quantum noise in fiber parametric processes, which is used to predict the quantum noise properties of parametric amplifiers and frequency converters. The modeling includes the effects of Raman scattering, fiber loss, and higher order dispersion as well as being valid in the depleted pump regime.

Chapter 4 is a two-part discussion of few-moded fiber Raman amplifiers; firstly, the impact of weak random linear mode coupling in the pump of two-moded Raman fiber amplifiers are modeled and

analyzed using a statistical approach. Secondly, the problem of equal modal gain in a two-mode Raman fiber amplifier is investigated experimentally, and a record low mode-dependent gain of 0.25 dB per 10 dB gain is demonstrated.

Chapter 5 presents a detailed investigation of inter-modal four-wave mixing in a two mode fiber. Two theoretical models are presented; analytic solutions are derived for the simplest, and comprehensive numerical simulations are presented for the more complicated. The results of the more complicated model are then compared to the results of experiments also carried out for this chapter in two different two-mode fibers.

Chapter 6 concludes the thesis and gives an outlook from the results presented in Chs. 3–5.

Chapter 2

Electromagnetic field theory

This chapter reviews the classical theory of light that the reader must be familiar with before reading on to the following chapters; fundamental equations are derived and basic assumption are accounted for here. In optical fibers, Maxwell's equations are divided in a transverse part that describes the guiding of the light in the fiber including effective index, dispersion and other modal properties, and a longitudinal part that describes the evolution of the electric field amplitude through the fiber including linear effects such as attenuation and effects of dispersion as well as nonlinear effects such as self- and cross-phase modulation, four-wave mixing (FWM) and Raman scattering. Both schemes are important for the results of this thesis so a section is dedicated to each scheme in this chapter after a more general section that starts from the beginning: Maxwell's equations.

2.1 Maxwell's Equations

When electromagnetic waves propagate through a material they obey a set of equations that relate the electric and magnetic fields to bound and free charges as well as to the magnetizability of the medium. These equations can be derived from basic principles of electro- and magnetostatics [55] but here they are merely stated in the convenient form of free charges and SI units: [56]

$$\nabla \cdot \mathbf{D}(\mathbf{r}, t) = \rho_f, \tag{2.1a}$$

$$\nabla \cdot \mathbf{B}(\mathbf{r}, t) = 0, \tag{2.1b}$$

$$\nabla \times \mathbf{E}(\mathbf{r},t) = -\frac{\partial \mathbf{B}(\mathbf{r},t)}{\partial t}, \tag{2.1c}$$

$$\nabla \times \mathbf{H}(\mathbf{r},t) = \mathbf{J}(\mathbf{r},t) + \frac{\partial \mathbf{D}(\mathbf{r},t)}{\partial t}, \tag{2.1d}$$

where $\mathbf{E}$ and $\mathbf{B}$ are the electric and magnetic fields, respectively, $\mathbf{r} = (x, y, z)$ is the spatial coordinate vector, t is time, ρ_f is the density of free charges, $\mathbf{J}$ is the current density, and

$$\mathbf{D} = \epsilon_0 \mathbf{E} + \mathbf{P}, \tag{2.2}$$

$$\mathbf{H} = \frac{1}{\mu_0}\mathbf{B} - \mathbf{M}, \tag{2.3}$$

are the displacement and the auxiliary magnetic fields, respectively, ϵ_0 is the vacuum permittivity, μ_0 is the vacuum permeability, $\mathbf{P}$ is the electrical induced polarization, and $\mathbf{M}$ is the induced magnetization of the material. Silica-based optical fibers are absent of free charges and currents and are magnetizable to a negligible degree only, which means $\rho_f = 0$, $\mathbf{J} = 0$, and $\mathbf{M} = 0$. Note that the analysis already at this point is distinguished from semiconductor platforms such as Silicon and Aluminium Galium Arsenide, in which $\rho_f \neq 0$. Thus, as the starting point for the rest of this thesis, Maxwell's equations take the form

$$\nabla \cdot \mathbf{D}(\mathbf{r},t) = 0, \tag{2.4a}$$

$$\nabla \cdot \mathbf{H}(\mathbf{r},t) = 0, \tag{2.4b}$$

$$\nabla \times \mathbf{E}(\mathbf{r},t) = -\mu_0 \frac{\partial \mathbf{H}(\mathbf{r},t)}{\partial t}, \tag{2.4c}$$

$$\nabla \times \mathbf{H}(\mathbf{r},t) = \epsilon_0 \frac{\partial \mathbf{E}(\mathbf{r},t)}{\partial t} + \frac{\partial \mathbf{P}(\mathbf{r},t)}{\partial t}. \tag{2.4d}$$

The induced polarization $\mathbf{P}$ is not straightforward to determine so it is custom to write it as a Taylor expansion in the electric field where each term is easier to evaluate,

$$\mathbf{P}(\mathbf{r},t) = \mathbf{P}^{(0)}(\mathbf{r},t) + \mathbf{P}^{(1)}(\mathbf{r},t) + \mathbf{P}^{(2)}(\mathbf{r},t) + \mathbf{P}^{(3)}(\mathbf{r},t) + \ldots, \tag{2.5}$$

where $\mathbf{P}^{(0)}$ is the static polarization, $\mathbf{P}^{(1)}$ is the linear induced polarization, etc.. The n'th order induced polarization is written in terms of the electric field as [57]

$$\mathbf{P}^{(n)}(\mathbf{r},t) = \epsilon_0 \int_{-\infty}^{\infty} \cdots \int_{-\infty}^{\infty} \mathbf{R}^{(n+1)}(t-\tau_1, \ldots, t-\tau_n) \, | \, \mathbf{E}_1(\mathbf{r},\tau_1) \ldots \mathbf{E}_n(\mathbf{r},\tau_n) d\tau_1 \ldots d\tau_n, \tag{2.6}$$

where $\mathbf{R}^{(n+1)}$ is an (n+1)'th order tensor that holds real and causal response functions in its elements, and the vertical line denotes n'th order tensor product. In silica, there is no static polarization and all even ordered induced polarizations are zero due to silica being amorphous; also, in this thesis 5'th and higher order are disregarded. This leaves only the first and third order induced polarizations: the first order induced polarization is usually assumed to have an instantaneous response due to the response time of electrons in the few-femto second regime, and all but the diagonal elements of the first order tensor are approximated zero, which gives

$$\begin{aligned}\mathbf{P}^{(1)}(\mathbf{r},t) &= \epsilon_0 \int_{-\infty}^{\infty} \mathbf{R}^{(1)}(t-\tau_1) \,|\, \mathbf{E}_1(\mathbf{r},\tau_1) d\tau_1 \\ &= \epsilon_0 \chi^{(1)} \mathbf{E}_1(\mathbf{r},t),\end{aligned} \tag{2.7}$$

where $\chi^{(1)} \equiv \chi_{jj}$ for $j = x$, y, or z is the time independent common amplitude of the diagonal elements of the first order response function, which is often called the linear susceptibility. The frequency dependence of the linear susceptibility is disregarded by assuming the time-domain response to be instantaneous.

The third order induced polarization is written as

$$\begin{aligned}\mathbf{P}^{(3)}(\mathbf{r},t) = \epsilon_0 \iiint_{-\infty}^{\infty} \mathbf{R}^{(3)}(t-\tau_1, t-\tau_2, t-\tau_3) \,| \\ \mathbf{E}_1(\mathbf{r},\tau_1)\mathbf{E}_2(\mathbf{r},\tau_2)\mathbf{E}_3(\mathbf{r},\tau_3) d\tau_1 d\tau_2 d\tau_3,\end{aligned} \tag{2.8}$$

but further progress cannot be made without specifying a specific nonlinear process, which is done in later chapters. Inserting Eqs. (2.5), (2.7), and (2.8) into Eq. (2.4d) gives the final version of Maxwell's equations

$$\nabla \cdot \mathbf{D}(\mathbf{r},t) = 0, \tag{2.9a}$$

$$\nabla \cdot \mathbf{H}(\mathbf{r},t) = 0, \tag{2.9b}$$

$$\nabla \times \mathbf{E}(\mathbf{r},t) = -\mu_0 \partial_t \mathbf{H}(\mathbf{r},t), \tag{2.9c}$$

$$\nabla \times \mathbf{H}(\mathbf{r},t) = \epsilon_0 n^2(x,y) \partial_t \mathbf{E}(\mathbf{r},t) + \partial_t \mathbf{P}^{(3)}(\mathbf{r},t), \tag{2.9d}$$

where $n^2(x,y) = 1+\chi^{(1)}$ is the refractive index of silica, which is assumed to have no longitudinal (z) dependence in fibers. In the latter equations, the notation of the derivative was simplified for convenience so that $\partial/\partial t \to \partial_t$.

2.2 Transverse equations: fiber modes

Many waveguides including fibers have geometries that favor a separation of Maxwell's equations into a transverse and a longitudinal part;

the transverse part determines the modal properties such as effective area and waveguide dispersion and the longitudinal part determines the evolution of the electric field amplitude through the waveguide.

Fiber mode properties are integral parts of inter-modal nonlinear effects through amplitude and intensity field overlaps and phase matching so a thorough understanding of fiber modes is important. Therefore, the mode properties of circular symmetric fibers are reviewed in the following.

Rightfully, guided modes in fibers are of vectorial nature where each mode has three spatial components. However, for many purposes including communication, fibers are weakly guiding, which results in approximate modes with only one spatial component and that form mode groups of 2 or 4 degenerate modes; these modes are called linearly polarized (LP) modes. In this section, it is sketched how Maxwell's equations are manipulated to find the true vectorial modes and afterwards the approximate LP modes are analyzed in more detail. Even though the full-vectorial picture is not necessary to understand the results of this thesis because all waveguides considered are weakly guiding, it is important in many emerging waveguide structures to consider full-vectorial effects [58]; hence, a short section is devoted to the subject here.

2.2.1 Vectorial modes

In a waveguide in general, the electric and magnetic field do not follow the same equations due to the non-zero divergence of the electric field. Therefore, one has to choose which one to eliminate and which one to calculate; the other can always be calculated using Maxwell's equations. It turns out to be easiest to eliminate the electric field and calculate the magnetic field; there is also the advantage of working with the magnetic field that it is continuous over boundaries in the dielectric function, which makes a numerical implementation of the equations easier.

The mode properties of a waveguide are calculated for a CW field and nonlinear contributions are neglected; since communication fibers are often circular symmetric, polar coordinates are preferred to take advantage of the circular symmetry. With a harmonic time dependence

$$\mathbf{E}(\mathbf{r},t) = \mathbf{A}_n(\mathbf{r})\exp(-i\omega_n t) \tag{2.10}$$

$$\mathbf{H}(\mathbf{r},t) = \mathbf{H}_n(\mathbf{r})\exp(-i\omega_n t), \tag{2.11}$$

then taking the curl of Eq. (2.9d) and inserting (2.9c), the following equation is achieved for the magnetic field

$$\nabla\times\nabla\times\mathbf{H}_n(\mathbf{r}) = k_0^2 n^2(\mathbf{r})\mathbf{H}_n(\mathbf{r}) + \frac{1}{n^2(\mathbf{r})}\nabla n^2(\mathbf{r})\times\nabla\times\mathbf{H}_n(\mathbf{r}), \tag{2.12}$$

where $k_0 = 2\pi/\lambda_0$ and λ_0 is the vacuum wavelength. Changing the equation to polar coordinates $(x, y) \to (r, \phi)$, where r is the radial coordinated and ϕ is the angular, assuming a harmonic dependence on the longitudinal component z in all components of the magnetic field, i.e. $\exp(i\beta_n z)$ where β_n is the propagation constant at frequency ω_n, and using the divergence constraint of Eq. (2.9b) the equation for the radial component of the magnetic field $H_r(r, \phi)$ (the subscript n now left out) becomes

$$\partial_r^2 H_r + \frac{1}{r}\partial_r H_r + \frac{1}{r^2}\left(\partial_\phi^2 H_r - H_r\right) - \frac{2}{r^2}\partial_\phi H_\phi + k_0^2 \epsilon H_r = \beta^2 H_r, \quad (2.13)$$

where H_ϕ is the angular component of the magnetic field. Because of the circular symmetry of the waveguide in consideration it is assumed that the angular dependence of all components of the magnetic field is either $\cos(m\phi)$ or $\sin(m\phi)$ where m is an integer. From Eq. (2.13) and the divergence constraint it is clear if $H_r \sim \cos(m\phi)$, then $H_\phi \sim \sin(m\phi)$ and $H_z \sim \cos(m\phi)$ and vice versa where H_z is the longitudinal component of the magnetic field. Inserting these angular dependencies the equations for the radial and angular components of the magnetic field become

$$\partial_r^2 H_r + \frac{1}{r}\partial_r H_r + k_0^2 n^2 H_r - \left(m^2 + 1\right)\frac{H_r}{r^2} \pm \frac{2m}{r^2} H_\phi = \beta^2 H_r \quad (2.14)$$

$$\partial_{rr} H_\phi + \frac{1}{r}\partial_r H_\phi - \frac{m^2+1}{r^2} H_\phi \pm \frac{2m}{r^2} H_r + k_0^2 n^2 H_\phi + \frac{1}{r}\frac{\partial_r n^2(r)}{n^2}\left(\pm m H_r - H_\phi - r\partial_r H_\phi\right) = \beta^2 H_\phi, \quad (2.15)$$

where ∂_{rr} means two times differentiation with respect to r, and '+' denotes $H_r \sim \sin(m\phi)$ and '−' denotes $H_r \sim \cos(m\phi)$. The z component of the magnetic field is determined through the divergence constraint and the electric field is calculated using Eq. (2.9d) (without the nonlinear induced polarization), and these components are

$$H_z = \frac{i}{\beta}\left(\frac{1}{r}\partial_r\left\{r H_r\right\} \mp \frac{m}{r} H_\phi\right) \quad (2.16)$$

$$E_r = \frac{i}{\omega\epsilon_0\epsilon}\left(\pm\frac{m}{r} H_z - i\beta H_\phi\right) \quad (2.17)$$

$$E_\phi = \frac{i}{\omega\epsilon_0\epsilon}\left(i\beta H_r - \partial_r H_z\right) \quad (2.18)$$

$$E_z = \frac{i}{\beta}\left[E_r\frac{\partial_r\epsilon}{\epsilon} + \frac{1}{r}\left(\partial_r\left\{r E_r\right\} \pm m E_\phi\right)\right] \quad (2.19)$$

The boundary conditions at the center of the circular symmetric fiber for the magnetic field are [59]

$$\partial_r[H_r(0), H_\phi(0)] = [0,0], \quad \text{for} \quad m = 1 \tag{2.20}$$

$$[H_r(0), H_\phi(0)] = [0,0], \quad \text{for} \quad m \neq 1. \tag{2.21}$$

Far away from the fiber core all guided modes have per definition zero amplitude. With Eqs. (2.14)–(2.19) and boundary conditions (2.20)–(2.21) established, the full solution to the vectorial problem of electromagnetic modes in circular symmetric fibers is established. No restrictions has been put on the dielectric function in the radial direction.

2.2.2 Linearly polarized modes

Many waveguides including most silica fibers support only weak guidance and the scalar approximation accounted for in this section therefore turns out to very useful, which is widely appreciated because of the simpler interpretation of the resulting modes.

By assuming harmonic time dependencies of both the electric and magnetic fields, as in Eqs. (2.10) and (2.11), taking the curl of Eq. (2.9d) (again neglecting the nonlinear induced polarization), inserting Eq. (2.9c), and applying simple rules of calculus, the combined equation becomes

$$\begin{aligned} &\nabla \times \nabla \times \mathbf{H}_n(\mathbf{r}) = \\ &\quad - i\omega\epsilon_0 \left(n^2(\mathbf{r})[\nabla \times \mathbf{E}_n(\mathbf{r})] - \mathbf{E}_n(\mathbf{r}) \times [\nabla n^2(\mathbf{r})] \right). \end{aligned} \tag{2.22}$$

The second term on the right hand side is complicated to evaluated but it is also small for weakly guiding structures; for example in a step index fiber it is zero except exactly at the boundary. Doing the scalar approximation means to neglect that term. Doing so and using Eq. (2.9c), Eq. (2.22) becomes the well-known Helmholtz equation

$$\left[\nabla^2 + \frac{\omega^2}{c^2} n^2(\mathbf{r}) \right] \mathbf{H}_m(\mathbf{r}) = 0, \tag{2.23}$$

where also the vector identity $\nabla \times \nabla \times \mathbf{V} = \nabla(\nabla \cdot \mathbf{V}) - \nabla^2 \mathbf{V}$ where $\mathbf{V}$ is a vector was used together with the divergence constraint of the magnetic field. It is notable that if the magnetic field is eliminated instead of the electric field, the same equation emerges under the scalar approximation. Therefore, it is common to use the symbol Ψ instead of either the electric or magnetic field. Changing to polar coordinates and, as for the vectorial modes above, assuming a harmonic dependence on z and separating the

radial and angular dependencies as $\Psi = R_m(r)\cos(m\phi)\exp(i\beta z)$, the Helmholtz equation takes the form

$$r^2\frac{\partial^2 R_m}{\partial r^2} + r\frac{\partial R_m}{\partial r} + \left[r^2 k_0^2 n(r)^2 - m^2\right] R_m = \beta^2 R_m, \tag{2.24}$$

where it should be noted that the angular index m is not the same as in the full-vectorial description. This equation is valid for all circular symmetric refractive index profiles as long as the scalar approximation is valid but it is difficult to get any further insight analytically from here. However, if the fiber is assumed to be a step index fiber then n^2 does not depend on the radius r and Eq. (2.24) readily reduces to Bessel's equation. More precisely, the radial position r can be either smaller or larger than the step index fiber core radius, a, which leaves two cases

$$r^2\frac{\partial^2 R_m}{\partial r^2} + r\frac{\partial R_m}{\partial r} + \left[r^2\kappa^2 - m^2\right] R_m = 0, \quad r < a \tag{2.25}$$

$$r^2\frac{\partial^2 R_m}{\partial r^2} + r\frac{\partial R_m}{\partial r} - \left[r^2\sigma^2 + m^2\right] R_m = 0, \quad r > a, \tag{2.26}$$

where

$$\kappa = \sqrt{k_0^2 n_c^2 - \beta^2} \tag{2.27}$$

$$\sigma = \sqrt{\beta^2 - k_0^2 n_{cl}^2} \tag{2.28}$$

and n_c and n_cl are the core and cladding refractive indexes, respectively. Equation (2.25) is Bessel's equation and Eq. (2.26) is Bessel's modified equation [60]; the physically interesting solutions here are the Bessel function of the first kind, $J_m(\kappa r)$ for $r < a$, and the modified Bessel function of the second kind, $K_m(\sigma r)$ for $r > a$.

The propagation constant β is determined by matching the fields at either side of the refractive index step using proper boundary conditions, which in the scalar approximation are that the field Ψ is continuous and differentiable across the boundary; this constraint leads to the condition [61]

$$\frac{J_m(\kappa a)}{\kappa a J_{m-1}(\kappa a)} = -\frac{K_m(\sigma a)}{\sigma a K_{m-1}(\sigma a)} \tag{2.29}$$

from which β must be determined numerically.

2.2.3 Waveguide and mode properties

With the solutions to Eqs. (2.25) and (2.26) known to be Bessel functions and the propagation constant determined from Eq. (2.29), both

the waveguide dispersion (not material dispersion) and all modal properties of a given fiber is known under the scalar approximation. In the following sections, basic properties of waveguide dispersion, field distributions and overlaps, and higher order modes are reviewed.

Waveguide dispersion

Waveguide dispersion means that the propagation constant changes as a function of the wavelength of the propagating light, which manifests itself in the simplest form by causing propagating pulses to broaden in the time domain, which is caused by the different frequency components of the pulse traveling with different velocities. This thesis, however, only considers CW fields but as will become evident later FWM requires phase matching for which dispersion is a crucial concept. Dispersion is quantified in terms of the propagation constant β but since a full spectrum of β values is rarely needed in fiber optics for communication it is custom to write β in a Taylor expansion around some central frequency ω_0

$$\begin{aligned}\beta(\omega) \approx \beta_0 + \beta_1(\omega-\omega_0) + \frac{\beta_2}{2!}(\omega-\omega_0)^2 \\ + \frac{\beta_3}{3!}(\omega-\omega_0)^3 + \frac{\beta_4}{4!}(\omega-\omega_0)^4 + \dots\end{aligned} \tag{2.30}$$

where $\beta_0 = \omega_0 n_{\text{eff}}/c$ and n_{eff} is the effective index at ω_0 of the mode that β represents, and β_1 is the inverse group velocity. The rest of the coefficients do not have common names but are generally referred to as higher order dispersion terms. However, in the wavelength domain it is common to define a dispersion coefficient; making a Taylor expansion of both sides of

$$\beta(\omega) = \frac{\omega n_{\text{eff}}(\omega)}{c} \tag{2.31}$$

one may derive the dispersion coefficient, defined as $D = -\frac{\lambda}{c}\partial_{\lambda\lambda} n_{\text{eff}}$,

$$\beta_2 = -\frac{2\pi c}{\omega^2} D \tag{2.32}$$

where the usual reciprocal relationship between frequency and vacuum wavelength is implied, $\lambda\omega = 2\pi c$. It proves useful later to also relate the third order dispersion β_3 to parameters in the wavelength domain; hence, one can further derive that

$$\beta_3 = \frac{\lambda^4}{(2\pi c)^2}\left(S + \frac{2D}{\lambda}\right), \tag{2.33}$$

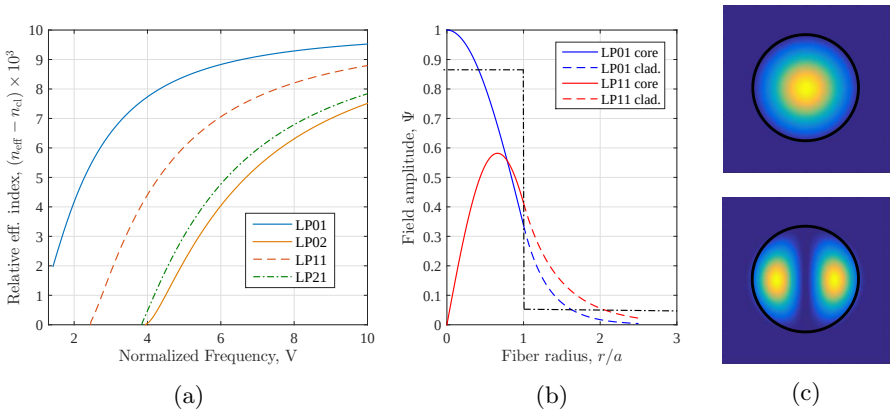

Fig. 2.1: (a) Effective indexes for scalar modes LP01, LP11, LP21, and LP02 vs. normalized frequency, V; (b) field amplitudes of LP01 and LP11 in a step index fibe vs. normalized radial position in the fiber; the black dash-dotted line is a sketch of the refractive index profile that has core radius a; (c) 2D intensity distribution in a step index fiber of LP01 (top) and LP11 (bottom) corresponding to (b); the black ring denotes the step in refractive index.

where $S = \partial_\lambda D$. Figure 2.1(a) shows plots of the n_{eff} of the first four guided modes, which were found numerically from Eq. (2.29) and (2.31), vs. the normalized frequency $V = \frac{2\pi a}{\lambda}\sqrt{n_{\text{c}}^2 - n_{\text{cl}}^2}$ in a weakly guiding step index fiber with core radius a and a numerical aperture of $\text{NA} = \sqrt{n_{\text{c}}^2 - n_{\text{cl}}^2} = 0.17$, where n_{c} and n_{cl} are the core and cladding index of the fiber, respectively; the modes are labeled LPml, where m is the angular order defined above and l is an index referring to a specific solution (β) given a defined m; there may be zero or many β-values for every m depending on the waveguide geometry. The plot shows that all dispersion curves of the four modes have the same effective index values at very different normalized frequencies (or wavelengths). This property leads to the possibility of phase matching FWM where the participating waves are separated in wavelength by hundreds of nanometers [62]. In Ch 5., FWM among waves in different modes is investigated.

In the scalar approximation of circular symmetric fibers each solution (set of m and l) come with both a $\sin(m\phi)$ and a $\cos(m\phi)$ solution and they apply to two states of polarization, which means that all solutions are four-fold degenerate; the LP0l solutions are only two-fold degenerate, however, since they do not have a $\sin(m\phi)$ solution. Generally in this thesis, only one state of polarization is considered but light couples between the $\sin(m\phi)$ and $\cos(m\phi)$ solutions, usually designated by a and b, on a short length scale in fibers due to fabrication imperfec-

tions. For purposes of nonlinear interactions the coupling between the two solutions does not matter for phase matching but the nonlinear field overlap discussed below is affected significantly.

Field distribution and overlaps

Different modes have different field distributions as well as different propagation constants; Fig. 2.1(b) and (c) show the field distributions of LP01 and LP11a, which are the modes of most interest in this thesis, in a step-index fiber. In a graded index fiber, the field distributions are slightly different but qualitatively much alike. Field distributions are important for nonlinear effects such as FWM and Raman scattering because these processes depend on the amplitude of the interacting light; when two modes have different field distributions their degree of interaction is not trivial. When inserting a nonlinear induced polarization into the general propagation equation (2.50) (in the scalar approximation) as derived in the next section a term containing the field distributions appears,

$$f_{ijkl}^{(\mu\nu\xi\zeta)} = \frac{\iint F_i^{(\mu)} F_j^{(\nu)} F_k^{(\xi)} F_l^{(\zeta)} dxdy}{\left(\iint {F_i^{(\mu)}}^2 dxdy \iint {F_j^{(\nu)}}^2 dxdy \iint {F_k^{(\xi)}}^2 dxdy \iint {F_l^{(\zeta)}}^2 dxdy \right)^{1/2}}, \tag{2.34}$$

where $f_{ijkl}^{(\mu\nu\xi\zeta)}$ is the nonlinear field overlap and $F_n^{(\alpha)}(x,y)$ is the real field distribution at frequency ω_n in mode α corresponding to the plots in Fig. 2.1(c); in terms of the description above, $F_n^{(\alpha)}(x,y)$ is defined as $\Psi(\mathbf{r})_n^{(\alpha)} = F_n^{(\alpha)}(x,y)\exp(i\beta_n^{(\alpha)}z)$. The denominator is a normalization term and the nominator determines the strength of the nonlinear interaction among the four fields. In circular symmetric fibers it is convenient to write $f_{ijkl}^{(\mu\nu\xi\zeta)}$ in polar coordinates, so

$$f_{ijkl}^{(\mu\nu\xi\zeta)} \sim \iint r R_i^{(\mu)}(r) R_j^{(\nu)}(r) R_k^{(\xi)}(r) R_l^{(\zeta)}(r) \times \sin(m_\mu\phi)\sin(m_\nu\phi)\sin(m_\xi\phi)\sin(m_\zeta\phi) dr d\phi, \tag{2.35}$$

from which it is clear that $f_{ijkl}^{(\mu\nu\xi\zeta)}$ is non-zero only if all of $(m_\mu, m_\nu, m_\xi, m_\zeta)$ are equal or pairwise equal. This selection rule is very useful and reduces the number of FWM terms considerably. For the rest of this thesis, the only modes considered are those with $l = 1$ and all frequencies are in

the communication band, which justifies neglecting the frequency dependence of $F_n^{(\alpha)}(x,y)$, so the nonlinear field overlap can be reduced to

$$f^{(\mu\nu)} = \frac{\iint {F^{(\mu)}}^2 {F^{(\nu)}}^2 dxdy}{\iint {F^{(\mu)}}^2 dxdy \iint {F^{(\nu)}}^2 dxdy}. \tag{2.36}$$

If all four waves are in the same mode, $f^{(\mu\nu)}$ reduces to the the inverse effective area $A_{\text{eff}}^{(\mu)} = 1/f^{(\mu)}$.

2.3 Propagation equation: nonlinear effects

In this section, the propagation equation that describes the longitudinal evolution of the electrical field is derived. This may be done in different ways where the most straightforward approach [56, 57] is to take the curl of Eq. (2.9c) and insert Eq. (2.9d) into the resulting expression; hence, the magnetic field is eliminated. A second approach is to use the reciprocity theorem [63], which has been deployed earlier [58, 64]. A third approach is offered by Kolesik and Moloney [65] and used by others [66–69], which turns out to be advantageous when the waveguide supports multiple modes and this approach is thus the one followed here.

The derivation starts by expanding the real electric field in N CW waves

$$\mathbf{E}(\mathbf{r},t) = \frac{1}{2}\sum_n^N \left[\mathbf{A}_n(\mathbf{r})\mathrm{e}^{-i\omega_n t} + \text{c.c.}\right], \tag{2.37}$$

where n is the frequency index and the time independent electric field $\mathbf{A}_n$ [V/m] is a sum of guided mode fields

$$\mathbf{A}_n(\mathbf{r}) = \sum_\mu \frac{\mathbf{F}_n^{(\mu)}(x,y)}{N_n^{(\mu)}} E_n^{(\mu)}(z)\mathrm{e}^{i\beta_n^{(\mu)}z}, \tag{2.38}$$

where μ is the mode index, $\mathbf{F}_n^{(\mu)}$ is the electrical vectorial transverse mode distribution function, $E_n^{(\mu)}$ $[\sqrt{\text{W}}]$ is the common (electric and magnetic) field amplitude, and $\beta_n^{(\mu)}$ is the propagation constant of mode μ and frequency ω_n. The normalization factor $N_n^{(\mu)}$ $[\text{m}/\sqrt{\Omega}]$ makes sure that $|E_n^{(\mu)}|^2$ is the power in watts carried by the electric field in mode μ, and it is defined as [66]

$$\frac{1}{4}\iint \left[\mathbf{F}_n^{(\nu)*} \times \mathbf{H}_n^{(\mu)} + \mathbf{F}_n^{(\mu)} \times \mathbf{H}_n^{(\nu)*}\right] \cdot \hat{\mathbf{z}}\, dxdy = \delta_{\mu,\nu} {N_n^{(\mu)}}^2, \tag{2.39}$$

where $H_n^{(\mu)}$ is the vectorial transverse mode distribution function of the magnetic field defined in the same way as $F_n^{(\mu)}$ is for the electric field, $\hat{\mathbf{z}}$ is a unit vector pointing in the longitudinal direction in the waveguide, $\delta_{\mu,\nu}$ is the Kronecker delta, and the integration is performed over all transverse space.

The derivation of the propagation equation is somewhat complicated but outlined here: if (2.38) is inserted into (2.37) the term

$$\mathcal{E}_m^{(\nu)}(\mathbf{r},t) = \mathbf{F}_m^{(\nu)}(x,y)\mathrm{e}^{-i\omega_m t + i\beta_m^{(\nu)} z} \tag{2.40}$$

may be identified; that term is complex conjugated and multiplied onto Eq. (2.9d) and the corresponding term for the magnetic field $\mathcal{H}_m^{(\nu)} = \mathbf{H}_m^{(\nu)}\mathrm{e}^{-i\omega_m t + i\beta_m^{(\nu)} z}$ is complex conjugated and multiplied onto Eq. (2.9c). Using simple rules of calculus one gets [65]

$$\nabla\cdot\left(\mathbf{H}\times\mathcal{E}_m^{(\nu)^*}\right) + \mathbf{H}\cdot\left(\nabla\times\mathcal{E}_m^{(\nu)^*}\right) = \epsilon_0 n^2 \mathcal{E}_m^{(\nu)^*}\cdot\partial_t\mathbf{E} + \mathcal{E}_m^{(\nu)^*}\cdot\partial_t\mathbf{P}^{(3)} \tag{2.41}$$

$$\nabla\cdot\left(\mathbf{E}\times\mathcal{H}_m^{(\nu)^*}\right) + \mathbf{E}\cdot\left(\nabla\times\mathcal{H}_m^{(\nu)^*}\right) = -\mu_0\mathcal{H}_m^{(\nu)^*}\cdot\partial_t\mathbf{H}, \tag{2.42}$$

where all implicit space and time dependencies were left out for clarity. Maxwell's equations are then used on the second term on the left hand side of each equations so

$$\nabla\cdot\left(\mathbf{H}\times\mathcal{E}_m^{(\nu)^*}\right) - \mu_0\mathbf{H}\cdot\partial_t\mathcal{H}_m^{(\nu)^*} = \epsilon_0 n^2 \mathcal{E}_m^{(\nu)^*}\cdot\partial_t\mathbf{E} + \mathcal{E}_m^{(\nu)^*}\cdot\partial_t\mathbf{P}^{(3)} \tag{2.43}$$

$$\nabla\cdot\left(\mathbf{E}\times\mathcal{H}_m^{(\nu)^*}\right) + \epsilon_0 n^2\mathbf{E}\cdot\partial_t\mathcal{E}_m^{(\nu)^*} = -\mu_0\mathcal{H}_m^{(\nu)^*}\cdot\partial_t\mathbf{H}, \tag{2.44}$$

where it is noted that $\mathbf{F}_m^{(\nu)}(x,y)$ does not depend on z and hence the small contribution from the nonlinear induced polarization is neglected (as is custom for calculating waveguide modes). Next, the two equations are subtracted and integration over a large window T in time is performed; the window is finite but much larger than any period of time considered otherwise, which makes it fair to assume that the fields that are otherwise considered CW have decayed at the boundaries of the window. With this assumption the terms $\mu_0\mathbf{H}\cdot\partial_t\mathcal{H}_m^{(\nu)^*}$ and $\mu_0\mathcal{H}_m^{(\nu)^*}\cdot\partial_t\mathbf{H}$ cancel when using integration by parts; the same goes for the terms $\epsilon_0 n^2\mathcal{E}_m^{(\nu)^*}\cdot\partial_t\mathbf{E}$ and $\epsilon_0 n^2\mathbf{E}\cdot\partial_t\mathcal{E}_m^{(\nu)^*}$. Then integration over all transverse

space is performed and one gets

$$\int_T \iint \nabla \cdot \left(\mathbf{H} \times \mathcal{E}_m^{(\nu)*} \right) - \nabla \cdot \left(\mathbf{E} \times \mathcal{H}_m^{(\nu)*} \right) dxdy\, dt = \int_T \iint \mathcal{E}_m^{(\nu)*} \cdot \partial_t \mathbf{P}^{(3)}\, dxdy\, dt. \tag{2.45}$$

The salient point of this approach to getting a propagation equation is the integral theorem [63]

$$\iint \nabla \cdot \mathbf{V}\, dxdy = \partial_z \iint \mathbf{V} \cdot \hat{\mathbf{z}}\, dxdy + \oint \mathbf{V} \cdot \hat{\mathbf{n}}\, dl, \tag{2.46}$$

where $\mathbf{V}$ is a vector, the two double integrals are surface integrals over all transverse space as in (2.45), and the closed integral is a line integral along the boundary of the transverse space. For waveguides it is safe to assume that all fields are zero along any boundary far away from the waveguide, which means that in this thesis the second term on the right hand side is always zero. With Eq. (2.46), Eq. (2.45) becomes

$$\partial_z \int_T \iint \left[\mathcal{E}_m^{(\nu)*} \times \mathbf{H} + \mathbf{E} \times \mathcal{H}_m^{(\nu)*} \right] \cdot \hat{\mathbf{z}}\, dxdy\, dt = -\int_T \iint \mathcal{E}_n^{(\nu)*} \cdot \partial_t \mathbf{P}^{(3)}\, dxdy\, dt. \tag{2.47}$$

Inserting (2.37) and (2.38) along with the same expressions for the magnetic field (not shown) into Eq. (2.47), using the orthogonality condition (2.39) and that only terms with no explicit time dependence are non-zero when integrating over time, Eq. (2.47) becomes

$$\partial_z E_m^{(\nu)} = -\frac{1}{2TN_m^{(\nu)}} \int_T \iint \mathrm{e}^{i\omega_n t - i\beta_m^{(\nu)} z} \mathbf{F}_m^{(\nu)*} \cdot \partial_t \mathbf{P}^{(3)}\, dxdy\, dt. \tag{2.48}$$

Lastly, the induced polarization is written in a complex expansion like the electric field

$$\mathbf{P}^{(3)} = \frac{1}{2} \sum_n^N \left[\mathbf{P}_n^{(3)}(\mathbf{r}) \mathrm{e}^{-i\omega_m t} + \text{c.c.} \right]. \tag{2.49}$$

After differentiating, only the frequency component in the sum that leaves a time independent term is non-zero when integrating over time and the final propagation equation for the field amplitude at frequency ω_m in mode ν becomes

$$\partial_z E_m^{(\nu)} = \frac{i\omega_m \mathrm{e}^{-i\beta_m^{(\nu)} z}}{4N_m^{(\nu)}} \iint \mathbf{F}_m^{(\nu)*} \cdot \mathbf{P}_m^{(3)}\, dxdy. \tag{2.50}$$

In the following chapters where different processes are considered, the corresponding nonlinear induced polarizations are derived and hence specific propagation equations. It is at this point noted that it has not so far been assumed that the waveguide is weakly guiding; the result (2.50) is valid for vectorial modes as well as in the scalar regime. So combined with Sec. 2.2.1, a complete framework for simulating nonlinear propagation of full-vectorial modes in in-magnetizable waveguides without free carriers is the result of this chapter.

2.4 Propagation equations for single mode parametric amplifiers

This section provides an example of how to derive specific propagation equations from the general equation (2.50). The degenerate parametric amplifier is considered, see Fig. 3.1(a), and consists of one strong pump p and to side bands; a signal s and an idler i; furthermore, stimulated Raman scattering is included to be used in Ch. 3. The configuration called modulation interaction (MI) has energy conservation $2\omega_\mathrm{p} = \omega_\mathrm{s} + \omega_\mathrm{i}$ so two pump photons are annihilated while creating a signal and an idler photon. The nonlinear induced polarization at the signal frequency is found by inserting (2.37) into (2.8); it is assumed that the electric field is polarized along the x direction only that only the $\chi^{(3)}_{xxxx}$ component of the third order susceptibility is non-zero; this simple picture means that $\mathbf{A}_n = \mathbf{x}A_n = \hat{\mathbf{x}}(F/N_n)E_n \exp(i\beta_n z)$. Using Eq. (2.49) the nonlinear induced polarization in Eq. (2.50) becomes

$$\begin{aligned}\mathbf{P}_\mathrm{s}^{(3)} = \hat{\mathbf{x}}\frac{\epsilon\chi^{(3)}}{4}\int R(t-\tau)\Big[&2\left(|A_\mathrm{s}|^2 + |A_\mathrm{p}|^2 + |A_\mathrm{i}|^2\right)A_\mathrm{s} + A_\mathrm{s}^2 A_\mathrm{s}^* \mathrm{e}^{2i\omega_\mathrm{s}(t-\tau)} \\ &+ A_\mathrm{p}^2 A_\mathrm{i}^* \mathrm{e}^{-i(2\omega_\mathrm{p}\tau - \omega_\mathrm{s}t - \omega_\mathrm{i}t)} + 2A_\mathrm{p}^2 A_\mathrm{i}^* \mathrm{e}^{-i(\omega_\mathrm{p}(t+\tau) - \omega_\mathrm{s}t - \omega_\mathrm{i}\tau)} \\ &+ 2A_\mathrm{s}|A_\mathrm{p}|^2 \mathrm{e}^{-i(\omega_\mathrm{p}-\omega_\mathrm{s})(t-\tau)} + 2A_\mathrm{s}|A_\mathrm{i}|^2 \mathrm{e}^{-i(\omega_\mathrm{i}-\omega_\mathrm{s})(t-\tau)} \\ &+ 2A_\mathrm{s}|A_\mathrm{p}|^2 \mathrm{e}^{i(\omega_\mathrm{p}+\omega_\mathrm{s})(t-\tau)} + 2A_\mathrm{s}|A_\mathrm{i}|^2 \mathrm{e}^{i(\omega_\mathrm{i}+\omega_\mathrm{s})(t-\tau)}\Big]\, d\tau,\end{aligned} \tag{2.51}$$

where the response tensor $\mathbf{R}^{(3)}(\tau_1, \tau_2, \tau_3) = \chi^{(3)} R(\tau_1)\delta(\tau_2)\delta(\tau_3)$ was used. To proceed, the response function $R(\tau)$ is specified to include both the Kerr effect and stimulated Raman scattering [66]

$$R(\tau) = (1 - f_R)\delta(\tau) + \frac{3}{2} f_R h_R(\tau) \tag{2.52}$$

where $f_R \approx 0.18$ is the Raman fraction of the total susceptibility and thus the nonlinear induced polarization becomes

$$\begin{aligned}\mathbf{P}_{\mathrm{s}}^{(3)} = \hat{\mathbf{x}}\frac{3\epsilon\chi^{(3)}}{4}\Big[&(1-f_R)\left(|A_{\mathrm{s}}|^2+2|A_{\mathrm{p}}|^2+2|A_{\mathrm{i}}|^2\right)A_{\mathrm{s}}+(1-f_R)A_{\mathrm{p}}^2A_{\mathrm{i}}^*\\&+f_R(|A_{\mathrm{s}}|^2+|A_{\mathrm{p}}|^2+|A_{\mathrm{i}}|^2)A_{\mathrm{s}}\\&+f_R\left(|A_{\mathrm{p}}|^2\tilde{h}_R(\Omega_{\mathrm{ps}})+|A_{\mathrm{i}}|^2\tilde{h}_R(\Omega_{\mathrm{is}})\right)A_{\mathrm{s}}\Big],\end{aligned} \tag{2.53}$$

where the Fourier transform of the time domain response function

$$\tilde{h}_R(\Omega_{\mathrm{ps}}) = \int_{-\infty}^{\infty} h_R(t-\tau)\mathrm{e}^{-i\Omega_{\mathrm{ps}}(t-\tau)}d\tau, \tag{2.54}$$

where $\Omega_{\mathrm{ps}} = \omega_{\mathrm{p}} - \omega_{\mathrm{s}}$. By inserting the obtained nonlinear induced polarization into the general propagation equation (2.50), the final propagation equations for the signal in the MI configuration including Raman scattering becomes

$$\begin{aligned}\partial_z E_{\mathrm{s}} = i\gamma_{\mathrm{s}}\Big[&|E_{\mathrm{s}}|^2E_{\mathrm{s}}+(2-f_R)\left(|E_{\mathrm{p}}|^2+|E_{\mathrm{i}}|^2\right)E_{\mathrm{s}}+(1-f_R)E_{\mathrm{p}}^2E_{\mathrm{i}}^*\mathrm{e}^{-i\Delta\beta z}\\&+f_R\left(|E_{\mathrm{p}}|^2\tilde{h}_R(\Omega_{\mathrm{ps}})+|E_{\mathrm{i}}|^2\tilde{h}_R(\Omega_{\mathrm{is}})\right)E_{\mathrm{s}}\Big]-\frac{\alpha_{\mathrm{s}}}{2}E_{\mathrm{s}},\end{aligned} \tag{2.55}$$

where $\gamma_{\mathrm{s}} = \omega_{\mathrm{s}}n_2/(cA_{\mathrm{eff}})$ [1/(W m)] and $n_2 = 3\chi^{(3)}\epsilon_0/(4n_{\mathrm{eff}}^2c)$ [m^2/W] is the nonlinear refractive index. The linear loss term $\alpha_{\mathrm{s}}/2$ is not derived but added in the end. During the derivation of (2.55) it was also assumed that the normalization factor N_n is independent of frequency and that it for linearly polarized modes is calculated to be [66]

$$N^2 \approx \frac{c\epsilon_0 n_{\mathrm{eff}}}{2}\iint F(x,y)^2dxdy. \tag{2.56}$$

Lastly, the phase mismatch parameter for degenerate parametric amplification was introduced,

$$\Delta\beta = \beta_{\mathrm{s}} + \beta_{\mathrm{i}} - 2\beta_{\mathrm{p}}, \tag{2.57}$$

and it is calculated in Ch. 3. By completely similar approaches the equations for the pump and idler are derived,

$$\begin{aligned}\partial_z E_{\mathrm{p}} = i\gamma_{\mathrm{p}}\Big[&|E_{\mathrm{p}}|^2E_{\mathrm{p}}+(2-f_R)\left(|E_{\mathrm{s}}|^2+|E_{\mathrm{i}}|^2\right)E_{\mathrm{p}}+2(1-f_R)E_{\mathrm{s}}E_{\mathrm{i}}E_{\mathrm{p}}^*\mathrm{e}^{i\Delta\beta z}\\&+f_R\left(|E_{\mathrm{s}}|^2\tilde{h}_R(\Omega_{\mathrm{sp}})+|E_{\mathrm{i}}|^2\tilde{h}_R(\Omega_{\mathrm{ip}})\right)E_{\mathrm{p}}\Big]-\frac{\alpha_{\mathrm{p}}}{2}E_{\mathrm{p}},\end{aligned} \tag{2.58}$$

$$\partial_z E_\mathrm{i} = i\gamma_\mathrm{i}\Big[|E_\mathrm{i}|^2 E_\mathrm{i} + (2-f_R)\left(|E_\mathrm{p}|^2 + |E_\mathrm{s}|^2\right)E_\mathrm{i} + (1-f_R)E_\mathrm{p}^2 E_\mathrm{s}^* \mathrm{e}^{-i\Delta\beta z} + f_R\left(|E_\mathrm{p}|^2\tilde{h}_R(\Omega_\mathrm{pi}) + |E_\mathrm{s}|^2\tilde{h}_R(\Omega_\mathrm{si})\right)E_\mathrm{i}\Big] - \frac{\alpha_\mathrm{i}}{2}E_\mathrm{i}, \tag{2.59}$$

The Raman response function in the frequency domain $\tilde{h}_R(\Omega)$ can be parameterized [70] from a measured curve [71].

Chapter 3

Raman and loss-induced quantum noise of fiber parametric processes

As already presented in the introduction, fiber parametric processes (PP) have many potential applications in optical communication systems. Therefore it is an important task to analyze the noise properties of PP since they determine how useful any application can be. Naturally, much works has already been carried out in this regard and since the main noise sources are of quantum nature, quantum optics approaches have been widely deployed. Semi-classical descriptions have also been developed and they are generally more simple than quantum approaches and it is easier to include other processes that distort the PP. This chapter presents such a semi-classical model that simultaneously describes four-wave mixing (FWM), Raman scattering, fiber loss, dispersion, and the regime of pump depletion, the combination of which no quantum model so far has described.

This chapter is based on Refs. [72–76].

3.1 Quantum noise in parametric processes

Figure 3.1 shows a number of fiber PP with different pump(s), signal, and idler configurations that have different properties in terms of amplitude and phase evolution of the signal and idler: parametric amplification is the signature of diagrams (a) modulation interaction (MI), (b) inverse MI, (c) outer band phase conjugation (PC), and (d) inner band PC, in which the two pump photons annihilate and create a signal and an idler photon (or two signal photons in (b)). The separate processes

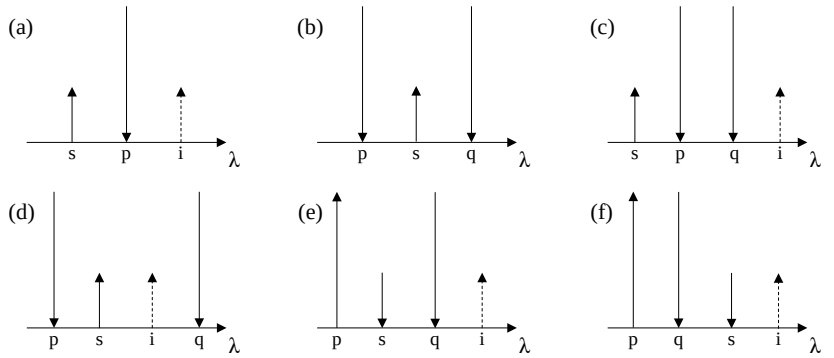

Fig. 3.1: Different configurations of FWM using two pumps, p and q, a signal, s , and an idler, i; (a) modulation interaction (MI), (b) inverse MI, (c) and (d) phase conjugation (PC), outer and inner band, respectively, (e) and (f) Bragg scattering (BS), distant and nearby, respectively; (a)–(d) do amplification and (e)–(f) do frequency conversion. The arrows indicate gaining (up) and losing (down) energy.

of (e) distant Bragg scattering (BS) and (f) nearby BS, however, do frequency conversion since here a pump and a signal photon are annihilated creating an idler photon and a photon in the other pump. The idler wave is dotted in all diagrams because it may be present at input or not; if it is not present the processes are phase-insensitive but if it is present the evolution of the fields in the fiber depends on the relative phases of the four input fields. In process (b), the idler and signal are frequency-degenerate so inverse MI is always phase-sensitive.

A critical parameter of any amplifier is of course the magnitude of gain achievable and the bandwidth of that gain. However, for many purposes including optical communication a measure for the amount of noise added in the amplification process is just as important. In single-mode fiber amplifiers, the most significant noise sources are related to pump-signal interactions and therefore an integrated part of the gain mechanism; this applies to all of EDFAs, Raman amplifiers, and FOPAs. The quantum noise properties of parametric processes have been described thoroughly in the literature: a phase-insensitive parametric amplifier (PIA) is a linear amplifier, and it was showed early on that linear amplifiers are associated with a 3-dB quantum induced reduction in the signal-to-noise ratio [27, 77]. During the 2000's, the quantum noise properties of all the parametric processes in Fig. 3.1(a)–(f) have been studied thoroughly by C. McKinstrie [29, 30, 78–80] in idealized cases without loss and Raman scattering and no pump depletion. For the results presented in the following sections, one of the most important

results is the quantum induced noise figure (NF) for phase-insensitive MI and PC that depends only on the PIA gain, G, as also showed by P. Voss *et al.* [29–31]

$$\mathrm{NF}_{\mathrm{PIA}} = \frac{1}{G} + \frac{2(G-1)}{G}, \tag{3.1}$$

which is easy to compare the modeling here to; $\mathrm{NF}_{\mathrm{PIA}}$ is 1 for $G = 1$ and converges toward 2 for $G \to \infty$. Equation (3.1) sets a fundamental quantum induced NF of PIAs. A similar expression for the NF of an undepleted phase-sensitive parametric amplifier (PSA) (Fig. 3.1(b) and (a) and (c)–(d) with idler input) can be derived and it depends on the relative phases of all participating waves as well as on the PSA gain [30]; the NF of a PSA may be as low as 0 dB in the high gain limit.

Another conclusion from C. McKinstrie that is important for the sections below is the conversion NF of BS that is expressed only in terms of the conversion efficiency; if converting from a signal to the idler in Fig. 3.1(e)–(f) with conversion efficiency CE, the NF is [30]

$$\mathrm{NF}_{\mathrm{BS}} = \frac{1}{\mathrm{CE}}, \tag{3.2}$$

which implies that the NF is ∞ for $\mathrm{CE} = 0$ and 1 for $\mathrm{CE} = 1$; i.e. if full conversion is achieved, the statistics of the output state equal those of the input state. Naturally, one must expect that phase mismatch, loss, and Raman scattering affects this results, which is demonstrated in the following sections. The impact of stimulated and spontaneous Raman scattering in both PIA and PSA have been investigated in the linear gain regime [31, 81] using quantum approaches; it is found for MI (Fig. 3.1(a)) that Raman scattering induces a spectrally asymmetric increase in the NF around the pump, and that the increase has a magnitude of 0.1–1 dB depending on the phase matching conditions of the FWM. For PSAs, the NF increase due to Raman scattering is approximately the same but it is symmetric around the pump.

It is generally accepted that semi-classical methods can reproduce the quantum results of Eqs. (3.1) and (3.2) in the large photon approximation [78] and indeed such methods has been used to predict the quantum noise properties of cascaded PIA and PSAs [33, 82]. Semi-classical methods has the advantage over quantum approaches that it is simple to include multiple effects simultaneously, such as FWM, Raman scattering, fiber loss, higher order dispersion, and pump depletion, which remains difficult if not analytically impossible for quantum approaches (quantum approaches have the advantage that they are superior models of the quantum nature of light; thus the semi-classical models must be

validated against quantum approaches). However, to the knowledge of the author, no one has presented a semi-classical model of the effects of quantum noise in parametric processes that includes all these effects; such a model is presented in the following section.

In the 1990's and early 2000's, FOPAs with very good noise properties were experimentally demonstrated [25, 83, 84] (compared to the noise properties of EDFAs) operating closer to the fundamental quantum limit; in the early 2010's, much work was carried out to understand the origin of the remaining excess noise in FOPAs [28, 82, 85], and four sources of noise were identified: 1) quantum noise (amplified vacuum fluctuations), 2) spontaneous Raman scattering, 3) pump residual noise, and 4) pump transferred noise. Number 1) quantum noise is included in the modeling presented here by defining an ensemble of fields that simulates vacuum fluctuations; 2) spontaneous Raman scattering is included by adding fluctuations terms from the pump to the propagating signal through the fiber; 3) pump residual noise is additional noise that stems from generating a high power pump, e.g. amplified spontaneous emission in a preceding EDFA, but it can be reduced significantly by proper filtering so it will not be considered any further here; 4) pump transferred noise is a results of large pump amplitude fluctuations that gives rise to fluctuations in the signal amplitude (and phase) through the amplification process; the effect is in principle included in the modeling presented here but focus is put on the effects of 1) and 2).

3.2 Semi-classical modeling of quantum noise

In this section, a semi-classical model of quantum noise in parametric processes is presented. FWM, stimulated Raman scattering, classical loss, and dispersion are included through the deterministic equations that were derived in the previous chapter. The quantum nature of loss, i.e. coupling to the vacuum state, vacuum fluctuations on the input coherent states, and spontaneous Raman scattering are included in the model as described below. But firstly, a brief review of quantum optics is given.

3.2.1 Brief review of quantum optics

In the completely separate quantum description of optics, the modeling of light is inspired by classical theory in terms of energy: the total field energy of classical a single-mode field (mode refers here to all of polarization, spatial mode, and frequency) that propagates in the z-

direction is [86]

$$H = \frac{1}{2}\int_V \epsilon_0 |E_x(z,t)|^2 + \frac{1}{\mu_0}|B_y(z,t)|^2 dxdydz, \tag{3.3}$$

where V denotes all space. By stating the time dependence of E_x and B_y explicitly in the functions $k(t)$ and $q(t)$ proportional to the amplitudes of E_x and B_y, respectively, and with proper normalizations, the total field energy reduces to

$$H = \frac{1}{2}\left(k^2 + \omega^2 q^2\right), \tag{3.4}$$

where ω is the frequency of the single-mode field and k and q can be identified as the position and momentum of an oscillator (like light is an oscillator in classical Maxwellian optics). Using the quantum mechanical correspondence principle, the total energy of the field must be the same in the low energy regime described by quantum optics so the scalar observable values of H, k and q can be replaced with operators

$$\hat{H} = \frac{1}{2}\left(\hat{k}^2 + \omega^2 \hat{q}^2\right). \tag{3.5}$$

The Hamiltonian $\hat{H}$ here proves more useful if put in a different form: the two non-observable operators $\hat{a} = (2\hbar\omega)^{-1/2}(\omega\hat{q} + i\hat{k})$ and $\hat{a}^\dagger = (2\hbar\omega)^{-1/2}(\omega\hat{q} - i\hat{k})$ are introduced and the Hamiltonian becomes

$$\hat{H} = \hbar\omega\left(\hat{a}^\dagger\hat{a} + \frac{1}{2}\right). \tag{3.6}$$

The eigenvectors of the Hamiltonian are called number states, $|n\rangle$, and the corresponding eigenvalue is the energy, $E_n = \hbar\omega(n + 1/2)$, where n is the number of photons in the given number state. It is from this expression that one notices the so-called vacuum energy by considering the case of zero photons, $n = 0$, where the total energy is still $E_0 = \hbar\omega/2$.

Even though the photon is commonly used in conceptual explanations of many optical phenomena, the photon number state is a quantum mechanical state that cannot be understood in terms of classical electromagnetism. Unlike electromagnetic waves, the photon does not have a phase; in terms of quantum fluctuations, the energy of the photon is completely determined while its phase is completely undetermined. Electromagnetic waves always have both a phase and an amplitude so it proves difficult to simulate such a quantum mechanical state in a semi-classical manner, which is the goal here. Therefore, a different state is studied: the much more classical coherent state.

The two operators, $\hat{a}$ and $\hat{a}^\dagger$, are called the annihilation and creation operators, respectively, due to their properties [86]

$$\hat{a}|n\rangle = \sqrt{n}|n-1\rangle \tag{3.7}$$

$$\hat{a}^\dagger|n\rangle = \sqrt{n+1}|n+1\rangle. \tag{3.8}$$

Evidently, the photon number state is not an eigenstate of either of the two operators but it turns out that the actual eigenstate of the annihilation operator is very useful. Initially, one may write

$$\hat{a}|\alpha\rangle = \alpha|\alpha\rangle, \tag{3.9}$$

which defines the coherent state $|\alpha\rangle$ and its eigenvalue α. Remembering that the Hamiltonian must be a hermitian operator due to the demand of real eigenvalues (the energy is an observable), the photon number states form an orthonormal basis in which the coherent state is expanded,

$$|\alpha\rangle = \sum_{n=0}^{\infty} C_n|n\rangle, \tag{3.10}$$

where C_n are expansion coefficients. By operating on this state with the annihilation operator, using its property (3.7), and enforcing the normalization $\langle\alpha|\alpha\rangle = 1$, it may be shown that the coherent state can be expressed in terms of photon number states and its eigenvalue, α,

$$|\alpha\rangle = \mathrm{e}^{-\alpha/2} \sum_{n=0}^{\infty} \frac{\alpha^n}{\sqrt{n!}}|n\rangle. \tag{3.11}$$

Calculating the probability of measuring n photons in a coherent state, one finds

$$P_n = |\langle n|\alpha\rangle|^2 = \mathrm{e}^{-\bar{n}} \frac{\bar{n}^n}{n!}, \tag{3.12}$$

which shows the commonly known property of shot noise, i.e. that the number of photons in a coherent state is random and follows a Poisson distribution with mean value $\bar{n} = |\alpha|^2$. A special property of the Poisson distribution is that the ratio of mean number to standard deviation squared is equal to the mean number,

$$\left(\frac{\bar{n}}{\sigma_n}\right)^2 = \frac{\bar{n}^2}{\mathrm{Var}_n} = \bar{n}, \tag{3.13}$$

where σ_n is the standard deviation on the number of photons and Var_n is the variance, which means that expected number of photons becomes

relatively increasingly more determined with increasing photon number; this is in accordance with the correspondence principle. Correspondingly, it may be shown that the phase of $|\alpha\rangle$ also follows a localized distribution around some mean value, ϕ, and that also the expected value of the phase becomes relatively increasingly more determined with increasing photon number. For these reasons the coherent state is commonly known as "the most classical" state.

Looking a bit more into the quantum mechanics of the coherent state, one may define the quadrature operators,

$$\hat{x} = \frac{1}{2}\left(\hat{a} + \hat{a}^\dagger\right) \tag{3.14}$$

$$\hat{p} = \frac{1}{2i}\left(\hat{a} - \hat{a}^\dagger\right), \tag{3.15}$$

which readily correspond to the real and imaginary parts if $\hat{a}$ and $\hat{a}^\dagger$ had been complex numbers. Operating with $\hat{x}$ and $\hat{p}$ on the coherent state, the variance of the electric field in each quadrature can be calculated [86],

$$\mathrm{Var}(\hat{x}) = \mathrm{Var}(\hat{p}) = \frac{1}{4}, \tag{3.16}$$

which is the same as the variance of the electric field in vacuum (independent on the amplitude α); conclusively, the coherent state can also be viewed as vacuum displaced in a phase-space diagram (or ultimately as a classical field with an amplitude and a phase with vacuum fluctuations on top). This property and the ones outlined above are used to define the semi-classical model of quantum fluctuations presented below.

3.2.2 Simulation of a coherent state

In the semi-classical scheme, a coherent state of light is simulated by defining an ensemble of classical fields that exhibits the same statistics in terms of amplitude and phase fluctuations as those associated with quantum fluctuations. The field ensemble has a mean amplitude corresponding to α above and mean phase ϕ; for large values of α, the ensemble mean values should be interpreted directly as the classical amplitude and phase of an electromagnetic wave, respectively.

The classical field ensemble that resembles a coherent state can be defined as [72, 73]

$$A_{\mathrm{ens}} = x_0 + \delta x + i(p_0 + \delta p), \tag{3.17}$$

where the variables x_0 and p_0 are the quadrature mean values (real and imaginary part of the classical electric field) and δx and δp are the

quadrature fluctuation variables that resemble the vacuum fluctuations of the coherent state. They follow Gaussian distributions with zero mean value and variance of 1/4 in photon number units in accordance with (3.16); however, since the field amplitude has the unit of $\sqrt{\mathrm{W}}$ the variance of δx and δp is rightfully

$$\mathrm{Var}(\hat{x}) = \mathrm{Var}(\hat{p}) = \frac{1}{4}\hbar\omega B_0, \tag{3.18}$$

where B_0 is a small frequency bandwidth of consideration for which 12 GHz is used. It is then straight forward to calculate the mean photon number in the ensemble (3.17),

$$n_{\mathrm{ens}} = \frac{\langle |A_{\mathrm{ens}}|^2 \rangle}{\hbar\omega B_0} = (x_0^2 + p_0^2)/(\hbar\omega B_0) + \frac{1}{2}, \tag{3.19}$$

where the 1/2 term denotes the explicit inclusion of the vacuum energy, which results from adding the fluctuation terms δx and δp in (3.17). To compare with the quantum result of Eq. (3.13), the variance of the ensemble absolute value squared, $\mathrm{Var}_{\mathrm{ens}}$, is calculated and the signal-to-noise ratio (SNR) is defined as

$$\mathrm{SNR}_{\mathrm{ens}} = \frac{\langle |A_{\mathrm{ens}}|^2 \rangle^2}{\mathrm{Var}_{\mathrm{ens}}}. \tag{3.20}$$

With $\mathrm{Var}_{\mathrm{ens}} = \langle |\mathrm{A}_{\mathrm{ens}}|^4 \rangle - \langle |\mathrm{A}_{\mathrm{ens}}|^2 \rangle^2$ the SNR of a coherent state ensemble in the large photon number regime becomes

$$\mathrm{SNR}_{\mathrm{ens}} \approx \frac{x_0^2 + p_0^2}{\hbar\omega B_0}, \tag{3.21}$$

which is the photon number n_{ens} for large photon numbers. Note that to obtain reliable statistics ensembles of $5 \cdot 10^4$ elements are used in all simulations. In all of the following, the usual definition of the NF is used,

$$\mathrm{NF} = \frac{\mathrm{SNR}_{\mathrm{in}}}{\mathrm{SNR}_{\mathrm{out}}}, \tag{3.22}$$

where $\mathrm{SNR}_{\mathrm{in}}$ and $\mathrm{SNR}_{\mathrm{out}}$ are the SNRs of the input and output ensembles, respectively.

3.2.3 Fiber loss

In classical electromagnetic theory, fiber loss is usually modeled with a linear loss term in the differential equations describing the propagation of

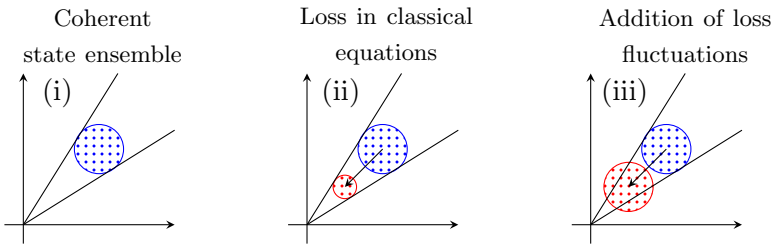

Fig. 3.2: (i) A coherent state ensemble visualized in a phase-space diagram, (ii) how the ensemble is affected by loss in the classical equations, and (iii) the effect of adding loss fluctuations.

the field. In quantum optics, loss can be modeled as a beam splitter [32] that couples the propagating field to the vacuum state. However, for the purpose here it is simpler to consider the variance of each quadrature, which may not decrease below 1/4 due to loss alone. In purely classical modeling, large losses implies that all fields decay asymptotically to zero, hence also the quadrature variances of the ensembles. A semi-classical model that takes vacuum fluctuations into account must therefore add a fluctuation term to all propagating fields. This fluctuation term is added in each numerical step to both the real and imaginary parts of all ensembles and the statistical properties of the term are

$$\langle \delta a_{\text{loss}} \rangle = 0, \tag{3.23}$$

$$\text{Var}(\delta a_{\text{loss}}) = \hbar\omega B_0 \alpha \Delta z/4, \tag{3.24}$$

where Δz is the step size and α is the loss coefficient. This value of the fluctuation variance ensures that the quadrature variances decay to 1/4 in the limit of large losses. It is also noted that a passive device (e.g. a fiber with attenuation) is well-known to influence a transmitted signal with a signal-to-noise degradation equal to the loss. It was subsequently verified that the model of LIN presented here captures this result correctly.

The effect of adding fluctuations during propagation is visualized in Fig. 3.2: in diagram (i), a coherent state ensemble of Eq. (3.17) is visualized in phase space and in (ii), the ensemble is attenuated (blue→red) through the classical, e.g. Eq. (2.55). Loss is classically a linear and phase-insensitive process, so all elements of the ensemble are translated directly towards the origo of the phase space; of course this process is not physical because the coherent state is squeezed in all directions. In diagram (iii), the effect of adding the loss fluctuation of Eqs. (3.23)–(3.24) is seen to undeterministically keep the shape of the coherent state. The addition of the fluctuation ensures at the same time automatically

that the change of the SNR is equal to the loss as expected of a passive device.

3.2.4 Spontaneous Raman scattering

Spontaneous Raman scattering has been studied earlier [87], and a model for the accumulation of amplified spontaneous emission (ASE) seeded by the Raman process at frequency ω_m on the Stokes (S) side of a given pump at frequency ω_n of power P_n is

$$P_{\mathrm{ASE,S}}(z) = \hbar\omega_m B_0 (n_{\mathrm{T}}^{(nm)} + 1) g_R^{(nm)} P_n \, z, \tag{3.25}$$

where B_0 is the bandwidth at frequency ω_m, $g_R^{(nm)} = 2\gamma_m f_R \tilde{h}_R(\Omega_{nm})$ is the Raman gain coefficient, and $n_{\mathrm{T}}^{(nm)}(\Omega_{nm}) = [\exp(\hbar|\Omega_{nm}|/k_{\mathrm{B}}T) - 1]^{-1}$ is the phonon equilibrium number at a pump-signal frequency separation of Ω_{nm}, where $\hbar$ is Plancks reduced constant, k_{B} is Boltzmanns constant, and T is the temperature [88]. On the anti-Stokes (AS) side, the corresponding expression is

$$P_{\mathrm{ASE,AS}}(z) = \hbar\omega_m B_0 n_{\mathrm{T}}^{nm} |g_R^{(nm)}| P_n \, z. \tag{3.26}$$

The $(n_{\mathrm{T}}^{(nm)} + 1)$-term in (3.25) means that SpRS on the S side does not require any phonons present but on the AS side the $n_{\mathrm{T}}^{(nm)}$-term gives SpRS a proportional dependence on the number of phonons. The rates of SpRS for the S and AS processes are defined as $(n_{\mathrm{T}}^{(nm)} + 1) g_R^{(nm)}$ and $n_{\mathrm{T}}^{(nm)} |g_R^{(nm)}|$, respectively, and they are plotted in Fig. 3.3, which shows these quantities at room temperature (solid blue) and at liquid nitrogen temperature (dashed red) vs. frequency shift Ω_{nm} from one of the pumps, p or q. Contrary to SRS, the rate of SpRS is asymmetric around the pump, which is important to consider when small signals are situated simultaneously on both sides of the pump, e.g. as they may be in FWM. Lowering the temperature reduces the rate of SpRS significantly on the AS side as expected, whereas on the S side a significant reduction occurs only close to the pump.

Because the rates of spontaneous Raman scattering on the S and AS sides are unequal, different fluctuation terms must be assigned to them: on the S side of a wave component n of power P_n, in every numerical step of size Δz the fluctuation $\delta a_{\mathrm{Raman,S}}$ must be added to each quadrature of a field m with the properties (calculated in Appendix A.1)

$$\langle \delta a_{\mathrm{Raman,S}} \rangle = 0, \tag{3.27}$$

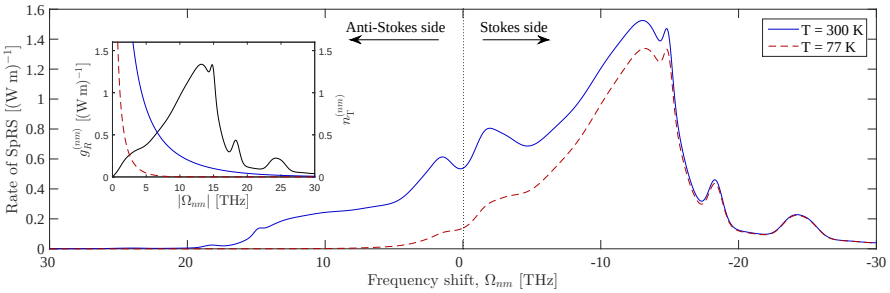

Fig. 3.3: Rate of SpRS vs. frequency shift Ω_{ij} from a pump p or q for temperatures $T = 300$ K (solid blue) and $T = 77$ K (dashed red). The inset shows the Raman gain coefficient g_{R} for silica core fibers (solid black) and the phonon equilibrium numbers n_{T} for the same temperatures as in the main plot (with same line styles).

$$\langle \delta a^2_{\mathrm{Raman,S}} \rangle \approx \left[g_{\mathrm{R}}^{(nm)} P_n \Delta z (n_{\mathrm{T}}^{(nm)} + 1)/2 - g_R^{(nm)} P_n \Delta z/4 \right] \hbar \omega_m B_0, \tag{3.28}$$

where $n_{\mathrm{T}}^{(nm)}$ and $g_{\mathrm{R}}^{(nm)}$ depend on the frequency shift as explained above and Δz is assumed small. On the AS side of wave component n, the corresponding fluctuation, $\delta a_{\mathrm{Raman,AS}}$, has the properties

$$\langle \delta a_{\mathrm{Raman,AS}} \rangle = 0, \tag{3.29}$$

$$\langle \delta a^2_{\mathrm{Raman,AS}} \rangle \approx \left(|g_{\mathrm{R}}^{(nm)}| P_n \Delta z \, n_{\mathrm{T}}^{(nm)}/2 + |g_R^{(nm)}| P_n \Delta z/4 \right) \hbar \omega_m B_0. \tag{3.30}$$

The addition of Raman fluctuations can be visualized in the same way as done for loss fluctuations in Fig. 3.2, only the Raman fluctuation will increase the size of the ensemble and hence the variance. It was confirmed in subsequent simulations (not shown here) and calculations that adding the fluctuations of Eqs. 3.27 and (3.28) produces the correct NF of a single-mode Raman amplifier (see Eq. (3.48) and Ref. [31]).

3.3 Degenerate parametric amplification

Degenerate parametric amplification, MI in see Fig. 3.1(a), is the simplest way of realizing a PIA experimentally, and it has the simplest theoretical description. Inverse MI of Fig. 3.1(b) is on the other hand a phase-sensitive process that despite the similar mathematical appearance turn out to be much more difficult to describe. In this section, the basic properties of MI are given initially; secondly, the semi-classically

model presented above is applied to a case of MI and fiber loss and Raman scattering are included in turn and their impacts are explored; thirdly, it is investigated how the field fluctuations behave in the depleted pump regime.

3.3.1 Analytic solutions

The three equations of MI are given in Eqs. (2.55)–(2.58) and (2.59) along with the phase mismatch in (2.57); in the case of a PIA and by disregarding loss and the stimulated Raman term (but keeping the $(1 - f_R)$-factor on the FWM term), they are solved in the undepleted pump regime as showed in Appendix A.2

$$G_{\text{PIA}} = \frac{P_s(z)}{P_s(0)} = 1 + \frac{\eta_{\text{s}}\eta_{\text{i}}}{g^2}\sinh^2(gz), \tag{3.31}$$

where $\eta_j = \gamma_j(1 - f_R)P_{\text{p}}$ is the nonlinear coefficient for pump, signal and idler, $j = \text{p, s, and i}$, P_p is the constant pump power, and

$$g^2 = \eta_{\text{s}}\eta_{\text{i}} - \left(\frac{\kappa}{2}\right)^2 \tag{3.32}$$

is the gain coefficient, where $\kappa = \Delta\beta + 2\eta_{\text{p}}$. In the absence of comprehensive dispersion data from the nonlinear fiber in question, the phase mismatch is readily calculated to [17]

$$\Delta\beta = -\frac{2\pi c}{\lambda_0^2}\frac{\partial D}{\partial \lambda}(\lambda_p - \lambda_0)(\lambda_p - \lambda_s)^2, \tag{3.33}$$

where λ_0 is the zero dispersion wavelength, $\partial D/\partial\lambda$ is the dispersion slope, λ_p is the pump wavelength, and λ_s is the signal wavelength. Figure 3.4 shows plots of the analytic PIA gain (3.31) and the analytic NF of Eq. (3.1) for typical parameters for a dispersion shifted highly nonlinear fiber (given in Tab. 3.1 in the next section) at the signal wavelength of optimal phase matching, $\Delta\beta = -2\eta_{\text{p}}$. Figure 3.4(a) shows the expressions through the fiber; as the gain increases the NF converges towards 3 dB. Fig. 3.4(b) has a fixed length of $L = 500$ m and varies the signal wavelength λ_s in Eq. (3.33).

More complicated expressions for the PSA gain are derived in [82] for the linear gain regime; in general the phase-sensitive amplification process depends also on the input idler phase and amplitude, whereas the phase-insensitive process does not. However, if ideal phase matching, $\Delta\beta = -2\eta_{\text{p}}$ (which determines the signal wavelength relative to the pump wavelength for a specific fiber) is assumed, and the relative phase

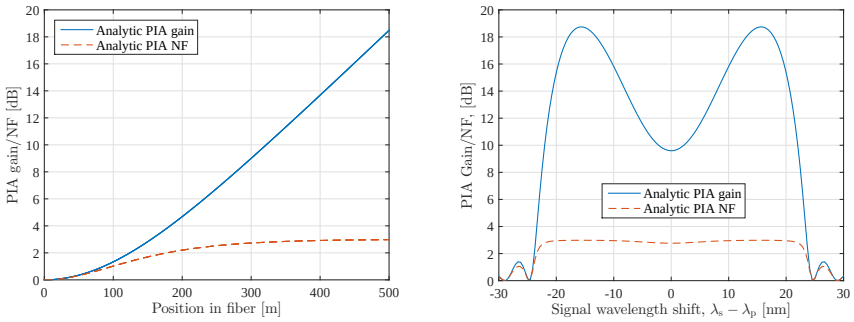

(a) (b)

Fig. 3.4: (a) Analytic PIA gain and NF vs. position in the fiber, Eq. (3.31), at the signal wavelength of optimal phase matching; (b) analytic PIA gain and NF spectrum; parameters are taken from Tab. 3.1.

of the pump, signal and idler is chosen to be $\theta_{rel} = 2\phi_p - \phi_s - \phi_i = -\pi/2$, the signal and idler grow according to

$$P_{\rm s}(z) = \left(\sqrt{G_{\rm PIA}(z)P_{\rm s,0}} + \sqrt{(G_{\rm PIA}(z)-1)P_{\rm i,0}}\right)^2, \tag{3.34}$$

$$P_{\rm i}(z) = \left(\sqrt{G_{\rm PIA}(z)P_{\rm i,0}} + \sqrt{(G_{\rm PIA}(z)-1)P_{\rm s,0}}\right)^2, \tag{3.35}$$

where $P_{\rm s,0}$ and $P_{\rm i,0}$ are the signal and idler input powers, respectively. The PS parametric gain is then $G_{\rm PSA}(z) = P_{\rm s}(z)/P_{\rm s,0}$.

3.3.2 Effect of fiber loss

Light attenuation in silica fibers is a relatively small effect with loss coefficients < 1 dB/km in highly nonlinear fibers and < 0.25 dB/km in standard single-mode fibers. It may however be useful in some cases to know some qualitative trends of the effects of loss on the NF of a PIA; for example higher order spatial modes can be used to achieve phase matching outside the Raman spectrum of the pump in silica, and if the pump, signal and idler are separated more than 20 THz it is likely that at least one of them resides in a part of the spectrum where silica has a high attenuation. In this section, Raman scattering is disregarded.

To simulate the gain and NF vs. position in a PIA of Fig. 3.1(a), Eqs. (2.55) and (2.58)–(2.59) are solved using a 4th order Runge Kutta method with a step size of 5 m; the process has energy conservation $2\omega_{\rm p} = \omega_{\rm s} + \omega_{\rm i}$. At the input, ensembles of Eq. (3.17) are prepared for each of pump signal and idler and each element in all three ensembles are

propagated in parallel. During propagation, loss fluctuations are added as described in Sec. 3.2.3 to each quadrature of the field ensembles. Realistic parameters for a nonlinear fiber are used, and table 3.1 shows the parameters used for all simulations in this section; the fiber nonlinearity $n_2/(cA_{\text{eff}}) = 8.223 \times 10^{-3}$ ps/(W km) corresponds to a nonlinear coefficient of 10 (W km)$^{-1}$ at the pump frequency; the signal wavelength is chosen to fulfill optimal phase matching, $\Delta\beta = -2\eta_{\text{p}}$, and the signal input power is -20 dBm, which is so low that any pump depletion effects due to FWM is avoided. This phase matching condition has two solutions (S and AS) for the signal wavelength but in the absence of Raman scattering they give identical results so the solution on the AS side is chosen.

Figure 3.5(a) shows the PIA gain G_{PIA} (blue) and NF (red) vs. position in the fiber z for two different losses, $\alpha = 1$ db/km and $\alpha = 5$ dB/km; recall that the quantum induced NF of a PIA is 3 dB in the high gain limit. The gain of the low loss simulation (dots) is 8 dB higher at $z = 500$ m than the high loss simulation (empty circles), which is due to the high loss reducing the pump powers. From expanding the analytic solution Eq. (3.31) one finds $G_{\text{PIA}} - 1 \propto (P_{\text{p}}L)^2$, which means the fiber loss has more than a linear effect on the gain. The two corresponding NF curves (stars and empty squares), however, are only ~ 0.4 dB different so even a large loss of 5 dB/km does not induce a significant NF in a relatively short PIA; this is because the loss only impacts the NF linearly.

In Fig. 3.5(b), the loss coefficient is varied to find out how much larger losses affect the NF; two different signal wavelengths are simulated to investigate if the former conclusion only holds for optimal phase matching. The gain of the optimally phase matched curve at $\lambda_{\text{s}} \cong \lambda_{\text{p}} - 17$ nm (blue dots) is naturally higher than that of the slightly

	Symbol	Value
Fiber length	L	500 m
Fiber nonlinearity	$n_2/(cA_{\text{eff}})$	8.223×10^{-3} ps/(W km)
ZDW	λ_0	1559 nm
Dispersion slope	S	0.03 ps/(nm^2 km)
Pump wavelength	λ_{p}	1561 nm
Pump power	P_{p}	0.7 W

Table 3.1: Nonlinear fiber parameter values used in this section for degenerate PA; ZDW, zero-dispersion wavelength.

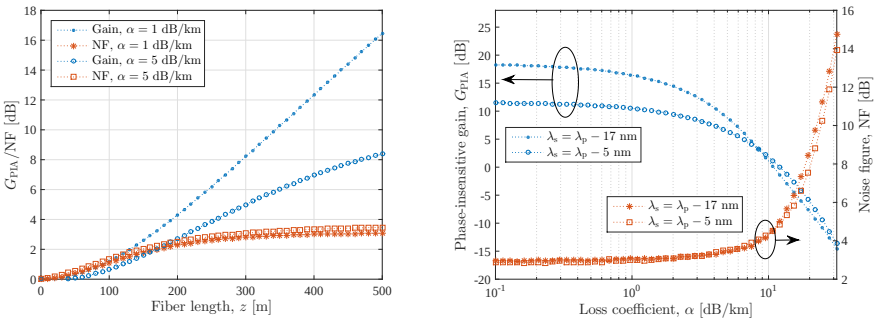

(a) (b)

Fig. 3.5: (a) PIA gain and NF vs. position in fiber for two different loss coefficients; the difference in gain is 8 dB but the difference in induced NF is only ~ 0.4 dB; (b) PIA gain and NF vs. loss coefficient for two signal wavelengths with different phase matching.

phase mismatched curve at $\lambda_s = \lambda_p - 5$ nm (blue empty circles), but they decay off to negative gain values more similarly; in fact, the curves are crossing at $\alpha \approx 10$ dB/km, which is most likely due to the nonlinear phase modulation also being affected by the loss.

Like in Fig. 3.5(a), the NFs in Fig. 3.5(b) are not affected by low losses (NF = 3 dB), and they are affected less by the increasing loss that the gain; but above $\alpha \approx$ 5–10 dB/km the NFs increase because the losses become so high that the signal and idler essentially do not experience any gain. Hence, the signal should have a NF going towards the loss like any passive device, which is seen as the steep increase in Fig. 3.5(b). Most notably, the NFs of the two cases of phase matching are very equal as long as the loss is small. After the NF starts to increase a difference of up to 1 dB is observed. In conclusion, realistic values of the loss coefficient in nonlinear silica fibers have only a minor effect on the parametric gain and no observable effect on the NF.

3.3.3 Effect of Raman scattering

Stimulated and spontaneous Raman scattering are important to consider when doing FWM; especially in silica because of its broad (~ 20 THz) and strong (Raman fraction of the third order susceptibility $f_R = 0.18$) Raman response. In this section, the Raman contribution to the gain and NF of MI operated as a PIA of Fig. 3.1(a) is simulated. In the same fashion as in the previous section, Eqs. (2.55) and (2.58)–(2.59) are solved numerically for three field ensembles now including Raman scattering and Raman fluctuations are added in every step. To isolate

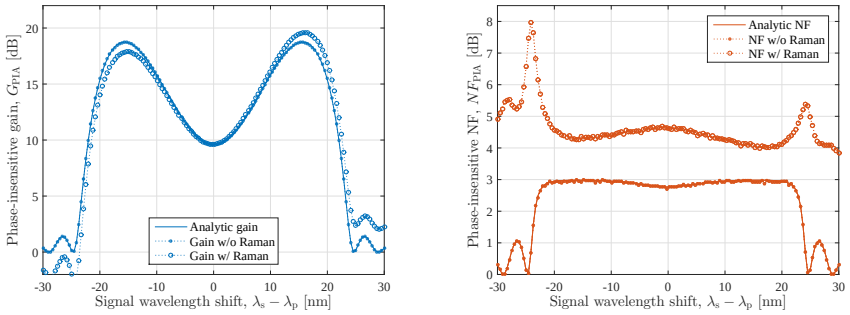

(a) (b)

Fig. 3.6: (a) PIA gain and (b) NF spectra with and without Raman scatteing; parameters taken from Tab. 3.1.

the effect of Raman scattering, fiber loss is disregarded. Simulation parameters are taken from Tab. 3.1.

The phase matching of the PIA and both stimulated and spontaneous Raman scattering depend on the signal wavelength shift from the pump so to understand their interaction, gain and NF spectra are plotted. Figure 3.6(a) shows the PIA gain with and without Raman scattering in a fiber of the parameters shown in Tab. 3.1. The analytic curve is a plot of Eq. (3.31). The effect of Raman scattering is a slightly asymmetric gain spectrum where the parametric gain is increased/decreased on the S/AS side by up to 2 dB with these parameters. The wider the bandwidth of phase matching is, the larger the effect of Raman scattering becomes (until a signal–pump shift of ~ 13 THz, which is a very large shift for FWM applications in single-mode fibers).

Figure 3.6(b) shows the NF spectrum corresponding to the gain spectrum in Fig. 3.6(a) with and without Raman scattering. Without Raman scattering (dots) the simulated NF agrees very well with the analytic quantum NF of Eq. (3.1), which confirms that a semi-classical model like the one used here can predict the quantum noise properties of PP accurately. Including Raman scattering induces an asymmetric NF, which remarkably is lower on the S side where more Raman noise is present, which is in accordance with earlier measurements [89]. The asymmetry of the Raman-induced NF is expected since the rate of spontaneous Raman scattering is asymmetric as shown in Fig. 3.3. However, to understand why the NF is largest on the AS side one must appreciate why a NF is induced by the PIA in the first place: as stated in Ref. [30] the SNR of the signal is degraded because of coupling to the vacuum fluctuations present in the idler. In classical terms, this coupling can be

viewed as the PIA operating as a semi-PSA because inputs are now in principle present in all of pump, signal, and idler; the vacuum fluctuations in the idler have a small amplitude and a random phase which makes the gain slightly random; hence, the variance of the output signal is a factor 2 larger than if no vacuum fluctuations were present in the idler, thus giving a NF of 3 dB.

The larger NF on the AS side can thus be explained by a larger amount of spontaneous Raman scattering going into the idler on the S side. The larger random fluctuations in the idler in the first meters of the fiber leads to a more random gain in the signal and hence a larger output power variance. The observed asymmetric Raman-induced NF is thus a combined Raman and FWM effect.

The local increase in the NF around the pump does not agree with existing results from quantum models [28, 31] in which the Raman contribution to the NF is vanishing near the pump. There is, however, an explanation why the local increase exists: the input signal has a circular shaped ensemble of a certain size in phase space, being a coherent state, and when it is amplified by the PIA the ensemble is moved to a larger amplitude while at the same time blown up; this is a simple consequence of the process being phase-insensitive. The amplified ensemble has a larger variance than the input ensemble so adding a Raman fluctuation of a certain variance has a smaller effect than adding the fluctuation to the input ensemble. Since the signal is phase matched differently at different wavelengths and thus increases in amplitude and variance with different rates through the fiber, adding the same amount of Raman fluctuations through the fiber has different impacts; if the PIA is phase matched, the signal ensemble is amplified within a short distance in the fiber and the distributed addition of Raman fluctuations has only a significant impact within that distance. If the PIA is not optimally phase matched, which is the case close to the pump, the signal ensemble is amplified through a longer distance in the fiber and more Raman fluctuations are thus added. At the time of writing, the author of this thesis does not know the reason why the quantum models do not show the increase in NF around the pump.

The higher peaks on the edges of the NF spectrum are due to poor phase matching in the PIA for which Raman scattering naturally has a more pronounced effect.

3.3.4 Phase-sensitive operation

A special characteristic of PP is that they can operate phase-sensitively [24, 82]; if all four fields participating in the FWM are present at the

input, the transfer of energy between pumps and side bands depends on the relative phases of the fields. This property makes it possible to control the gain of the amplifier by varying the input phases [24] thus realizing a PSA. In terms Fig. 3.1, the (a) and (c)–(f) are PS if both signal and idler are present at input; (b) is signal-degenerate and therefore always phase sensitive. PSAs have been predicted to have a 0-dB NF when the relative phase is such that maximum gain is achieved [82].

PSAs are more difficult to analyze numerically but Tong *et al.* [82] have calculated the PSA NF using a semi-classical approach and assuming that the FWM process is phase matched and that the relative phase of the pump, signal and idler is $\theta = 2\phi_\mathrm{p} - \phi_\mathrm{s} - \phi_\mathrm{i} = -\pi/2$, so

$$\mathrm{NF}_\mathrm{PSA}(z) = \frac{(P_{\mathrm{s},0} + P_{\mathrm{i},0})}{(P_\mathrm{s} + P_\mathrm{i})^2} \cdot \left[\left(\sqrt{GP_\mathrm{s}} + \sqrt{(G-1)P_\mathrm{i}} \right)^2 + \left(\sqrt{G_\mathrm{PIS} P_\mathrm{i}} + \sqrt{(G_\mathrm{PIA} - 1)P_\mathrm{s}} \right)^2 \right]. \tag{3.36}$$

This NF is based on the SNR being defined for combined signal and idler inputs, i.e. [81]

$$\mathrm{SNR} = \frac{\langle |A_\mathrm{ens,s}|^2 + |A_\mathrm{ens,i}|^2 \rangle^2}{\mathrm{Var}(|A_\mathrm{ens,s}|^2 + |A_\mathrm{ens,i}|^2)}. \tag{3.37}$$

Note that in the case of equal signal and idler input powers, the PS NF reduces to 1 (0 dB) independent of the gain. A PSA is simulated here by solving Eqs. (2.55) and (2.58)–(2.59) for MI of Fig. 3.1 but this time preparing an ensemble for the idler at input with the same amplitude as the signal; the relative phases of the input waves are chosen such that $\theta = -\pi/2$. Loss is disregarded to isolate the effect of Raman scattering. Fluctuations of spontaneous Raman scattering are added during propagation. The parameters used are the same as in the previous section of the PIA.

Figure 3.7 shows the PS gain and NF spectra with and without Raman scattering for the same parameters as used in Fig. 3.6; the PI analytic gain and NF are also shown for reference. At the wavelength shifts of optimal phase matching, $\Delta\beta = -2\eta_\mathrm{p}$ (maximum gain), the simulations of gain and NF agree well with the analytic predictions of Eq. (3.34) and Eq. (3.36), respectively. In the high gain limit the gain of the PSA is $4\times$ the gain of the PIA as expected from Eq. (3.34). Stimulated Raman scattering causes an asymmetric gain spectrum similar to the PIA but the NF is now symmetric around the pump. This latter feature

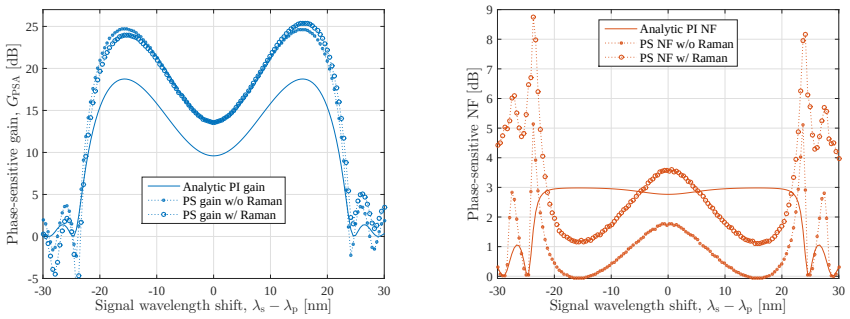

(a) (b)

Fig. 3.7: (a) PSA gain and (b) NF spectra with and without Raman scatteing; parameters taken from Tab. 3.1.

is no surprise since the evaluation of the SNR, Eq. (3.37), is symmetric in signal and idler.

It is notable that besides the NF being zero at the point of optimal phase matching, which only allows for one channel to be amplified, the PS NF is below the 3-dB limit of the PIA at all other wavelengths inside the gain spectrum as well; including Raman scattering only increases the PS NF above the 3-dB limit very close to pump.

3.3.5 Quantum fluctuations in pump depletion

One characteristic common for all quantum models of quantum noise is that they fail to describe the depleted pump regime. This is due to the difficulties of solving the quantum version of the complete set of coupled equations that describe FWM; the pumps are always assumed to be classical and of constant amplitude. In the classical equations used in this semi-classical model, however, pump depletion is an integral part that is included in the numerical solution.

To explore the depleted pump regime a PIA with parameters from Tab. 3.1 is simulated in the same manner as above, only the signal input power is changed to 0 dBm and the fiber length is increased to $L = 1000$ m; Raman scattering and loss are omitted. Figure 3.8(a) shows the power of the pump (blue), signal (red), and idler (green) through the fiber; the signal wavelength was chosen to fulfill optimal phase matching in terms of maximum undepleted gain, but as is clearly visible in Fig. 3.8(a) maximum gain before depletion does not mean maximum achievable gain in depletion. The phase matching condition for full conversion from pump to signal and idler must be found by analytically studying the set of equations (2.55) and (2.58)–(2.59) without making

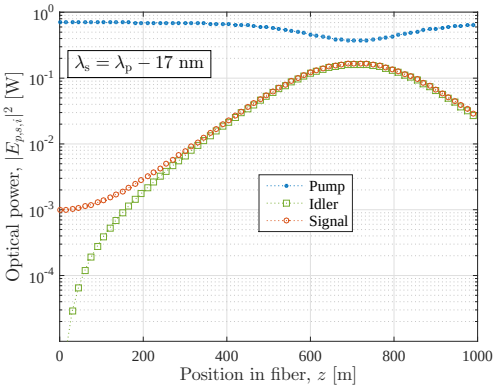

Fig. 3.8: Power of pump (blue dots), signal (red empty circles), and idler (green empty squares) vs. position in the fiber in a PIA operated in the depleted pump regime. Parameters taken from Tab. 3.1 except $L = 1000$ m.

the undepleted pump approximation.

The NF of the signal is plotted in Fig. 3.9(a) vs. position in the fiber; the PIA gain is included for reference: in the linear gain regime, the NF is 3 dB as expected but as the pump start to deplete the NF drops to large negative values. After the signal and idler starts giving back to the pump the NF returns to 3 dB. The explanation for the drastic decrease in NF is found in Fig. 3.9(b) where constellation diagrams of the signal are shown; (i) in the linear gain regime, (ii) and (iv) in intermediate positions around maximum depletion, and (iii) at the point of maximum depletion; the black dotted lines point toward the origo of the phase spaces. The mechanism behind the decreasing NF is amplitude squeezing of the signal ensemble when pump depletion is approached. Notice however that as the signal enters the depleted regime after being amplified, its fluctuations are much larger than those of vacuum. Therefore, the squeezed states shown in diagrams ii)-iv) do not show quantum squeezing in which the fluctuations of one quadrature are smaller than the vacuum fluctuations at the cost of larger fluctuations in the other quadrature. The results of Fig. 3.9 of the semi-classical model are already known as the concept of amplitude regeneration of optical signals; in gain-saturated parametric amplifiers it has been demonstrated several times [90–93].

It was verified in Ref. [72] that Raman scattering has no significant effect on the results above before and specifically at the point of maximum; after this point, however, the S and AS sides of the pump behave very different. It was further shown in [72] that also the pump ensem-

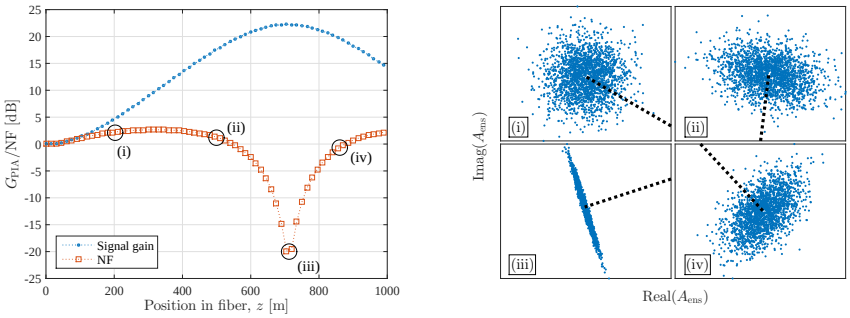

(a) (b)

Fig. 3.9: (a) Gain and NF vs. position in fiber in a PIA operated in the depleted pump regime; (b) constellation diagrams of the signal ensemble at the designated points (i)–(iv); the black dottes lines point toward the origo of the phase spaces

ble changes shape and gets squeezed when the regime of depletion is engaged.

3.4 Parametric frequency conversion

As explained above, BS is a noise-less process that enables frequency conversion of quantum states. However, other physical effects are present in silica fibers, which distort the performance of BS. In this section, the impacts of fiber loss and Raman scattering on BS is simulated. Both nearby and distant BS was shown in Fig. 3.1 but in this section only nearby BS is investigated. Figure 3.10 shows the two possible cases of nearby BS, one where the signal and idler are on the S side of the pumps, case (i), and one where the signal and idler are on the AS side of the pumps, case (ii). Cases (i) and (ii) have the same FWM properties but different Raman interaction. The parameters δ and Δ are the frequency separations between the signal and idler (and between the two pumps) and the separation between the zero dispersion frequency ω_0 and the closet wave component on either side, respectively. The symmetry $\omega_{\mathrm{s}} - \omega_0 = \omega_0 - \omega_{\mathrm{q}} \equiv \Delta$ is implied.

3.4.1 Propagation equations and analytic solutions

In Sec. 2.4 in Ch. 2, the propagation equations for MI were derived. Using the same approach but instead considering the energy conservation $\omega_{\mathrm{p}} + \omega_{\mathrm{s}} = \omega_{\mathrm{q}} + \omega_{\mathrm{i}}$ valid for BS as shown in Fig. 3.1(e)–(f), the propagation equations for the electric field amplitude at frequency ω_n

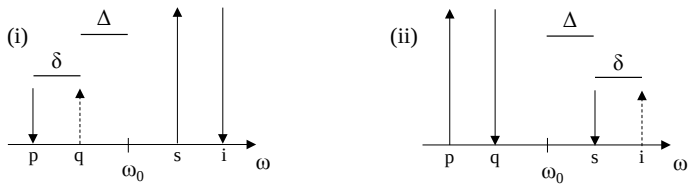

Fig. 3.10: Wave configurations of the two BS processes investigated in Sec. 3.4; (i) and (ii) have the same FWM properties but different Raman interactions.

becomes

$$\partial_z E_\mathrm{p} = i\gamma_\mathrm{p}\left[|E_\mathrm{p}|^2 E_\mathrm{p} + (2-f_R)\left(\sum_{k=\mathrm{s,q,i}}|E_k|^2\right)E_\mathrm{p} + 2(1-f_R)E_\mathrm{q}E_\mathrm{i}E_\mathrm{s}^*\mathrm{e}^{i\Delta\beta z} + f_R E_\mathrm{p}\left(\sum_{k=\mathrm{s,q,i}}|E_k|^2\tilde{h}_R(\Omega_{k\mathrm{p}})\right)\right], \tag{3.38}$$

$$\partial_z E_\mathrm{s} = i\gamma_\mathrm{s}\left[|E_\mathrm{s}|^2 E_\mathrm{s} + (2-f_R)\left(\sum_{k=\mathrm{p,q,i}}|E_k|^2\right)E_\mathrm{s} + 2(1-f_R)E_\mathrm{q}E_\mathrm{i}E_\mathrm{p}^*\mathrm{e}^{i\Delta\beta z} + f_R E_\mathrm{s}\left(\sum_{k=\mathrm{p,q,i}}|E_k|^2\tilde{h}_R(\Omega_{k\mathrm{s}})\right)\right], \tag{3.39}$$

$$\partial_z E_\mathrm{q} = i\gamma_\mathrm{q}\left[|E_\mathrm{q}|^2 E_\mathrm{q} + (2-f_R)\left(\sum_{k=\mathrm{p,s,i}}|E_k|^2\right)E_\mathrm{q} + 2(1-f_R)E_\mathrm{s}E_\mathrm{p}E_\mathrm{i}^*\mathrm{e}^{-i\Delta\beta z} + f_R E_\mathrm{q}\left(\sum_{k=\mathrm{p,s,i}}|E_k|^2\tilde{h}_R(\Omega_{k\mathrm{q}})\right)\right], \tag{3.40}$$

$$\partial_z E_\mathrm{i} = i\gamma_\mathrm{i}\left[|E_\mathrm{i}|^2 E_\mathrm{i} + (2-f_R)\left(\sum_{k=\mathrm{p,s,q}}|E_k|^2\right)E_\mathrm{i} + 2(1-f_R)E_\mathrm{s}E_\mathrm{p}E_\mathrm{q}^*\mathrm{e}^{-i\Delta\beta z} + f_R E_\mathrm{i}\left(\sum_{k=\mathrm{p,s,q}}|E_k|^2\tilde{h}_R(\Omega_{k\mathrm{i}})\right)\right]. \tag{3.41}$$

If only the FWM terms is considered, it is instructive to express the CE in terms of the phase mismatch. It is assumed the two strong pumps to have constant amplitudes such that

$$E_{\rm p}(z) = \sqrt{P_{\rm p}}\exp(i\gamma_p[P_{\rm p}+(2-f_R)P_{\rm q}]z), \quad (3.42)$$
$$E_{\rm q}(z) = \sqrt{P_{\rm q}}\exp(i\gamma_q[P_{\rm q}+(2-f_R)P_{\rm p}]z), \quad (3.43)$$

where $P_{\rm p}$ and $P_{\rm q}$ are the constant pump powers and $\gamma_j = n_2\omega_j/(cA_{\rm eff})$. By solving the resulting equations for the signal and idler, neglecting loss and Raman scattering, one easily finds

$$\mathrm{CE}(z) = \frac{|E_{\rm i}(z)|^2}{|E_{\rm s}(0)|^2} = \frac{\eta_{\rm i}^2}{(\kappa/2)^2+\eta_{\rm i}\eta_{\rm s}}\sin^2(gz) \quad (3.44)$$

where $\eta_j = 2(1-f_R)\gamma_j\sqrt{P_{\rm p}P_{\rm q}}$ is the effective nonlinear strength, $g^2 = \eta_{\rm i}\eta_{\rm s}+(\kappa/2)^2$ is the phase-mismatched conversion coefficient, and $\kappa = \Delta\beta+(1-f_R)(\gamma_p+\gamma_q)(P_{\rm q}-P_{\rm p})-(1-f_R)(\gamma_{\rm i}P_{\rm q}-\gamma_{\rm s}P_{\rm p})$. The phase mismatch, $\Delta\beta$, can be expressed in terms of δ and Δ as

$$\Delta\beta \approx -\frac{\beta_4}{12}\delta(2\Delta+\delta)\left(2\Delta^2+2\Delta\delta+\delta^2\right). \quad (3.45)$$

where β_4 is the fourth order dispersion; all odd ordered dispersion terms fall away due to the symmetry of the BS configurations (i) and (ii). Maximum conversion from signal to idler is achieved for $\kappa = 0$, which gives $\mathrm{CE} = \eta_{\rm i}/\eta_{\rm s}$, which further is the same as full conversion in photon numbers. This condition can be met experimentally by adjusting the difference in pump powers to counter-balance the phase mismatch if the values of δ and Δ are not too large relative to the fourth-order dispersion. Alternatively, a broad bandwidth of phase matching can be achieved through dispersion engineering, as demonstrated recently in a dispersion shifted fiber [54], or special phase matching properties across small [94] or large [62] bandwidths can be achieved using higher order modes. If $\kappa \approx 0$ is valid, one may derive an approximate analytic expression for the CE, where Raman scattering and loss are included. By assuming no energy exchange among the pumps, disregarding the effect of loss on the phase modulation terms in the pump equations, and neglecting the Raman interaction between the signal and idler, the CE becomes (after some calculations)

$$\mathrm{CE} = \frac{|E_{\rm i}(z)|^2}{|E_{\rm s}(0)|^2} = \frac{\eta_{\rm i}^2}{\mu^2}\exp\left[(f_{\rm s}+f_{\rm i})z_{\rm eff}\right]\exp(-\alpha z)\sin^2\left(\mu z_{\rm eff}\right) \quad (3.46)$$
$$\approx \frac{\eta_{\rm i}^2}{\mu^2}\exp\left[(f_{\rm s}+f_{\rm i}-\alpha)z\right]\sin^2(\mu z), \quad (3.47)$$

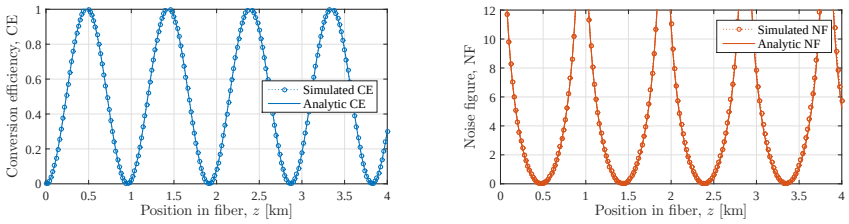

(a) (b)

Fig. 3.11: (a) CE va. position in fiber of BS for perfect phase matching; (b) corresponding NF. Parameters are seen in Tab. 3.2.

where $\mu^2 = \eta_\mathrm{i}\eta_\mathrm{s} - (f_\mathrm{i} - f_\mathrm{s})^2/4$ is the phase matched conversion coefficient, $z_\mathrm{eff} = (1 - \exp[-\alpha z])/\alpha$ is the effective position in the fiber, and $f_\mathrm{i} = i\gamma_\mathrm{i} f_R(\tilde{h}_R(\Omega_\mathrm{pi})P_\mathrm{p} + \tilde{h}_R(\Omega_\mathrm{qi})P_\mathrm{q})$ and $f_\mathrm{s} = i\gamma_\mathrm{s} f_R(\tilde{h}_R(\Omega_\mathrm{ps})P_\mathrm{p} + \tilde{h}_R(\Omega_\mathrm{qs})P_\mathrm{q})$ are the Raman contributions to the signal and idler, respectively. In expression (3.47), it was assumed that $\alpha z \ll 1$.

3.4.2 Quantum fluctuations—conservation of statistics

As another validation of the semi-classical model of this thesis, the noise properties of BS are simulated without any distorting effects. Equations (3.38)–(3.41) are solved numerically with field ensembles for p, s, and q as input like described in the previous section but no fluctuations are added; loss and Raman scattering are disregarded. Phase matching is forced numerically by setting $\beta_4 = 0$ and having equal pump powers so $\kappa \approx 0$ is valid; hence, the performance of BS does not depend on which frequency configuration (i) or (ii) (or any other BS configuration) is considered.

Figure 3.11 shows the analytic and simulated CE (a) and NF (b) of BS. The CE oscillates between 0 and (approximately) 1, meaning that light is transferred efficiently between signal and idler. At the same time the same amount of light is transferred between the pumps. The NF oscillates in phase with the CE between infinity and 0. The fact that the NF becomes zero at every full conversion is a signature of the noise-less conversion property of BS. The simulated CE agrees well with the analytic result of Eq. (3.44), and the simulated NF equally well with the quantum result of Eq. (3.2); hence, it is again confirmed that the present semi-classical model can predict quantum noise properties of fiber PP. The parameters used in this section are seen in Tab. 3.2.

	Symbol	Value
Fiber length	L	4 km
Fiber nonlinearity	$n_2/(cA_{\text{eff}})$	8.223×10^{-3} ps/(W km)
Frequency shift	$\Delta/2\pi$	1 THz
Frequency shift	$\delta/2\pi$	1 THz
4th order dispersion	β_4	0 ps^4/km
Pump p power	P_{p}	0.2 W
Pump q power	P_{q}	0.2 W
Temperature	T	300 K

Table 3.2: Nonlinear fiber parameter values used in this section for BS.

3.4.3 Effect of fiber loss

As explained above, fiber loss couples the propagating field to the vacuum state, which not only results in a reduction of the average number of photons but also an addition of fluctuations from the vacuum state. In the context of realizing quantum state preserving frequency conversion, it is of interest to investigate how fiber loss affects the performance of BS, so Raman scattering is excluded and it is assumed that $\kappa \approx 0$ by one of the approaches discussed above.

Figure 3.12 shows the results of a simulation of the set of Eqs. (3.38)–(3.41) and the addition of fluctuations during propagation with $\alpha =$ 1 dB/km for all wave components, which implies that the results do not depend on which case (i) or (ii) is considered and only slightly on the values of δ and Δ through the frequency dependence of γ_j for $j \in \{\text{p}, \text{q}, \text{s}, \text{i}\}$, which is usually neglected [56]. The CE vs. position in the fiber is plotted in Fig. 3.12(a) (blue dots) together with the analytic result of Eq. (3.46) (solid black), where excellent agreement is found. The red-dashed line compares the simulated CE to the approximation of Eq. (3.47), which gives the same as if losses on the pumps are neglected entirely; for small αz the approximation is seen to be reasonable. The importance of the solid-red line, the loss factor, is seen in Fig. 3.12(b) in which the loss-induced NF is plotted: the blue dots show the simulated NF vs. position in the fiber where each local minimum corresponds to maximum CE in Fig. 3.12(a). The solid-red line thus marks a loss-induced noise floor that equals $\exp(\alpha z)$. However, increasing the pump powers gives a shorter conversion distance since the conversion coefficient is $\mu^2 = \eta_{\text{i}}\eta_{\text{s}} \propto P_{\text{p}}P_{\text{q}}$, thus the accumulated signal and idler losses become

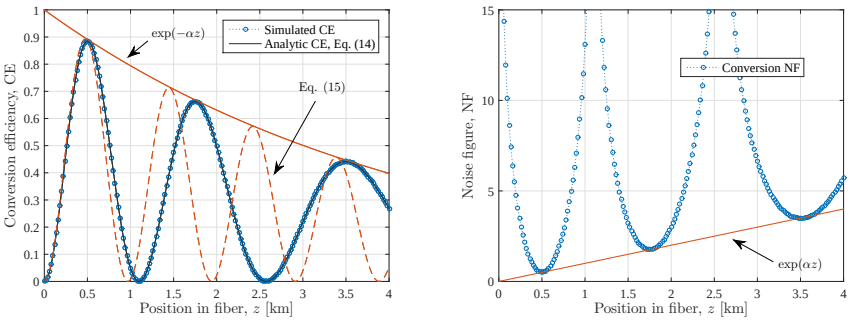

(a) (b)

Fig. 3.12: (a) CE vs. fiber length with optimal phase matching and without Raman scattering. The red lines visually illustrate the effects of loss on the CE. (b) The same for the conversion NF. Parameters are seen in Tab. 3.2.

smaller.

To investigate how the loss-induced noise couples between the signal, the idler, and the two pumps, the loss coefficient is set to zero at the different components in turn and repeat the simulation above (not shown graphically). If the losses of the signal and idler are excluded while keeping the losses of both pumps, the CE oscillates between 0 and 1 as if no loss was present, but the oscillation is still slowed by the loss in the pumps. The NF follows the CE, thus oscillating between infinity and 0. Hence, the loss-induced fluctuations in the pumps do not couple to the signal and idler. Turning on the loss in either of the signal or idler gives indistinguishable results, the characteristics of which are intermediate between turning the losses on or off in both. Consequently, the loss-induced fluctuations in the signal couple to the idler. If only the losses of the pumps are excluded, the slowing of the CE and NF oscillation disappears and the solution of Eq. (3.47) is very accurate, but the NF observed in Fig. 3.12(b) is not decreased, which confirms that no pump fluctuations were coupled to the signal and idler through FWM.

3.4.4 Effect of Raman scattering

SRS and FWM have a complicated interplay because they depend differently on the frequency shifts Δ and δ: FWM requires phase matching, while SRS, which is anti-symmetric around the pumps, has a complicated material response in the frequency domain; furthermore, SpRS is asymmetric around the pumps. To isolate the effects of SRS and SpRS in the FWM process, loss is disregarded henceforth and it is assumed again that $\kappa \approx 0$.

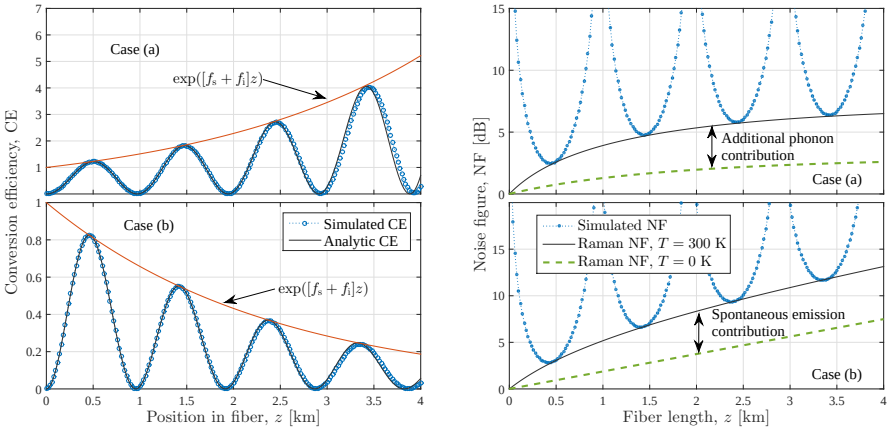

(a) (b)

Fig. 3.13: (a) CE vs. fiber length for case (i) (top) and (ii) (bottom); both simulation (dotted blue) and analytic result (3.46) are shown; the legend applies to both plots, and the thick red line is the Raman amplification term. (ii) The same for the NF; the analytic Raman NF (solid black) is Eq. (3.48) and Eq. (3.49) for the top and bottom plots, respectively; the dashed green line is the Raman NF at 0 K. Parameters are seen in Tab. 3.2.

Figure 3.13 shows the results of solving Eqs. (3.38)–(3.41) and adding Raman fluctuations at $T = 300$ K during propagation in cases (i) (top) and (ii) (bottom); Fig. 3.13(a) shows the CE vs. position in the fiber, and the simulated (dotted blue) and the analytic (solid black) results agree very well. After ~ 2 km the two curves start differing significantly because no energy exchange among the pumps was assumed in the analytic expression. The actual energy exchange between the pumps in form of Raman scattering taking place in the simulation has two impacts on the conversion efficiency due to SRS transferring energy to the lowest frequency pump, which is p in these cases: firstly, the difference in pump power causes a phase mismatch cf. the definition of κ; secondly, the conversion coefficient $\mu^2 \approx \eta_\mathrm{i}\eta_\mathrm{i} \propto P_\mathrm{p}P_\mathrm{q}$ becomes smaller because the product of two functions that have a constant sum is largest when values of the functions are equal.

In case (i), where the signal and idler are on the S side of the pumps, the CE grows through the fiber, essentially experiencing Raman amplification. That is, a CE higher than unity means that the signal and idler have been amplified by SRS to a higher output than the signal input. The red curve denotes the Raman amplification term. The NF oscillates in phase with the CE, but the lowest achievable point increases

according to the S side Raman-induced NF (calculated in Appendix A.1)

$$\mathrm{NF_S} = \frac{1}{G} + \frac{2[G-1](n_\mathrm{T}(\Omega_\mathrm{pi})+1)}{G}, \tag{3.48}$$

where $G = \exp[g_\mathrm{R}^\mathrm{pi}(P_\mathrm{p}+P_\mathrm{q})z]$ is the mean Raman gain of the signal and idler from the two pumps as explained in the Appendix. The dashed green line of Fig. 3.13(b) (top plot) marks the Raman-induced NF at 0 K, so the region between that curve and the solid black curve is the NF induced by the existence of thermally excited phonons.

In case (b), where the signal and idler are on the AS side of the pumps, the CE drops exponentially off because energy flows towards the pumps through SRS. The NF on the AS side is different from that on the S side for two reasons: firstly, since the AS process requires the presence of phonons, AS SpRS cannot occur at 0 K (as discussed above), and secondly, Raman depletion removes photons from a wave component so the SNR must change accordingly (much like the effect of losses). Hence, the AS Raman-induced NF is (also calculated in Appendix A.1)

$$\mathrm{NF_{AS}} \;=\; \frac{1}{L} + \frac{2[1-L]n_\mathrm{T}(\Omega_\mathrm{ip})}{L}, \tag{3.49}$$

where $L = \exp[-g_\mathrm{R}^\mathrm{ip}(P_\mathrm{p}+P_\mathrm{q})z]$. The dashed green line of Fig. 3.13(b) (bottom plot) represents the minimum Raman NF of the AS side as caused by Raman depletion, and the region between that curve and the analytic curve is the entire SpRS contribution.

Having established that Eq. (3.46) is a good description of phase matched BS in the presence of loss and Raman scattering and that the S and AS NFs of Eqs. (3.48) and (3.49) accurately predicts the NF of BS at the points of optimal conversion, these analytic expressions are used to analyze the frequency and temperature dependencies of the BS CE and NF. Figure 3.14(a) and (b) shows the CE of Eq. (3.46) vs. Δ of cases (i) and (ii) of Fig. 3.10, respectively, at the fiber length of the first optimal conversion point, $L = \pi/(2\mu)$; κ was assumed to be zero and the other parameters were taken from Tab. 3.2 (except the temperature T, the frequency shift Δ, and the fiber length L). In Fig. 3.14(a) and (b), the CE is in both cases essentially showing the signal and idler average Raman amplification (a) and depletion (b) that they receive from the two pumps; for these realistic parameter values, stimulated Raman scattering is a significant effect (in both cases up to a factor $\times 2.5$) that must be taken into account in silica fibers. Note that the frequency separation between the pump and the side band that are closest together is 2Δ.

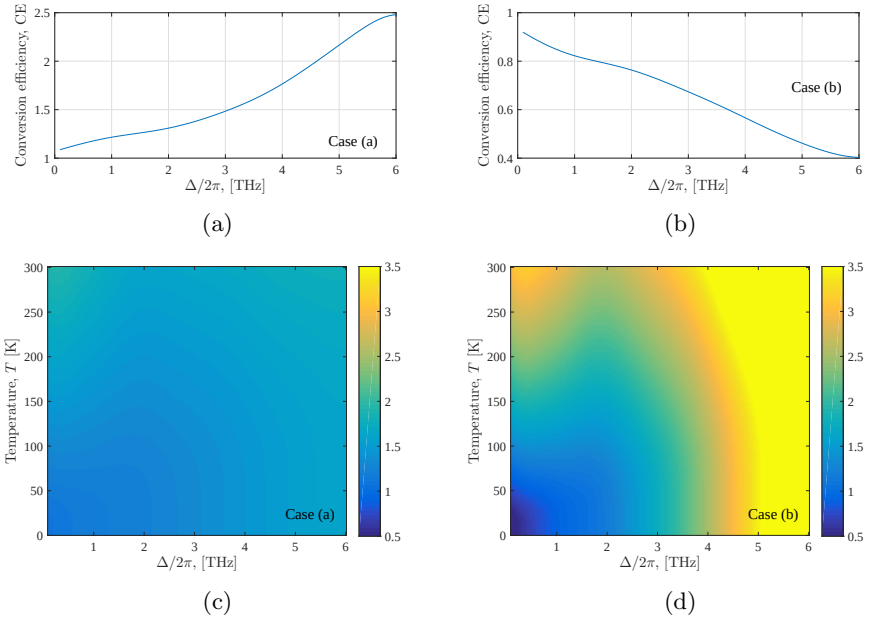

Fig. 3.14: (a) and (b) CE of Eq. (3.46) of cases (i) and (ii) of Fig. 3.10, respectively; (c) and (d) NFs of Eqs. (3.48) and (3.49), respectively, color scales are in dB.

Figure 3.14(c) and (d) show the NF of cases (i) and (ii), respectively, i.e. Eqs. (3.48) and (3.49) vs. Δ and the temperature, T; the color scalings on the two plots are equal. On the S side of the pumps, case (a), the NF does not vary much with neither Δ nor T; for low T and low Δ (lower left corner) the NF takes values around 1 dB, for $T \sim 300$ K and small Δ (upper left corner) the NF takes values around 1.9 dB, and for high Δ the NF is approximately 1.7 dB for all T (right side). This behavior is expected from the explanation of the rates of SpRS in Fig. 3.3: the rate of SpRS does not converge to 0 with decreasing temperature but towards the Raman gain coefficient, and even for $\Delta \to 0$ one of the side bands is still separated δ and 2δ from the two pumps, respectively, thus receiving SpRS from them.

On the AS side of the pumps, on the other hand, the NF depends much more on both Δ and T. For low T, the rate of SpRS is zero and the induced NF is only due to Raman depletion; even for $\Delta \to 0$, the signal and idler are depleted slightly by the furthest separated pump. For higher T, Raman depletion still increases with Δ but the rate of SpRS decreases with Δ so a trade-off resulting in a local minimum in NF around $\Delta = 2$ THz is observed. In the minimum at $T = 300$ K, the NF is approximately 2.6 dB. Given these numbers, the S side seems

advantageous with lower NF but an important note on the difference in origin between the S and AS NFs should be taken. The S NF is solely induced by SpRS, which increases the power variance of a signal ensemble due to the random phase of the spontaneous decay; the AS NF is composed of both SpRS and the effect of Raman depletion. The rate of SpRS is always smallest on the AS side so the power variance increases less there and in the total NF of 2.6 dB at 300 K in Fig. 3.14(d), SpRS is only responsible for 1.4 dB of the total NF. This number is found using Eq. (3.49) by setting $n_T = 0$ and recognizing the remaining part as the Raman depletion contribution, and then subtracting that number from the total NF.

Specific, realistic parameters where chosen in all simulations conducted in this chapter but it has been verified in subsequent simulations that the presented results do not change notably by changing the γ_j and the pump powers by an order of magnitude. Changing δ significantly naturally leads to a different Raman interaction, especially between the pump and the side bands that are separated the most.

3.5 Partial conclusion

In this chapter, the quantum noise properties of parametric amplification using degenerate four-wave mixing and parametric frequency conversion in form of Bragg scattering in silica fibers were investigated. A versatile semi-classical model that accounts for all of four-wave mixing, Raman scattering, fiber loss, and dispersion, which no quantum model to the knowledge of the author does, was presented and it was demonstrated to a great extend that the semi-classical model agrees with existing quantum models.

It was demonstrated that while loss plays a minor role for phase insensitive parametric amplifiers, Raman scattering has an important impact on the noise properties. An asymmetric noise figure spectrum was predicted and it was explained why the spectrum is reverse asymmetric compared to what might be expected from the asymmetry of spontaneous Raman scattering. An increased NF around degenerate pump was observed which is not predicted by quantum approaches. In the depleted pump regime, the semi-classical model predicts amplitude regeneration of the signal ensemble even in the presence of Raman scattering. The special noise properties of phase-sensitive parametric amplification was also investigated and it was shown that even in the presence of Raman scattering, phase-sensitive amplification still has a < 3 dB noise figure, which is the lower quantum limit of phase-insensitive amplifiers.

For Bragg scattering, it was shown that loss in the signal and idler reduces the conversion efficiency and induces a noise floor equal to the common loss factor, and that loss in the pumps reduces the angular velocity of the energy oscillation between the signal and idler. Further elaboration showed that the pump losses do not induce a noise figure in the signal and idler; on the other hand, loss in either of the signal and idler induces a noise figure in the other component.

Both stimulated and spontaneous Raman scattering were shown to have a significant impact on the frequency conversion of Bragg scattering: stimulated Raman scattering affects the conversion efficiency as one would expect from Raman amplifiers, the higher wavelength components receive energy from the lower wavelength components. SpRS, which is asymmetric around the pumps, induces a noise figure of 1.7–1.9 dB on the Stokes side of the pumps, case (i) of Fig. 3.10, for one full conversion from signal to idler at room temperature; on the anti-Stokes sides of the pumps, case (ii), a total noise figure of 2.6 dB to > 3.5 dB is predicted for the same conditions. Lowering the temperature reduces SpRS on the Stokes side of the pumps but does not remove it; on the anti-Stokes side, SpRS is removed completely when lowering the temperature but the effect of Raman depletion is still present. Thus, the theoretical predictions confirm that the presence of Raman scattering in silica fiber-based four-wave mixing in form of Bragg scattering contaminates the quantum noise-less frequency conversion to a significant degree that is comparable to the 3-dB noise figure induced by amplifiers such as parametric amplifiers, Raman and Erbium-doped fiber amplifiers.

Chapter 4

Linear mode coupling and mode dependent gain in few-mode Raman fiber amplifiers

Individual spatial modes in few-mode fibers (FMF) have been shown to hold great promise as a means to enhance the capacity in an optical communication system since they form a basis in a space division multiplexed (SDM) communication system. Each individual mode is ideally orthogonal to all other modes and capable of carrying information. However, one challenge in such systems is optical amplification. An amplifier in an SDM system must preferably be able to amplify individual modes with the same gain and with the same noise performance in all modes and at multiple wavelengths at the same time. This chapter deals with two aspects of Raman fiber amplifiers that are introduced along with the presence of multiple propagation modes: the distortion of unwanted linear mode coupling and the challenge of achieving equal gain in all modes. The first is investigated theoretically by stochastic modeling in forward pumped distributed Raman fiber amplifiers; for the second task, an experimental framework for measuring the Raman intensity overlaps in a fiber is presented and it is shown how this data is used for achieving record low mode-dependent gain (MDG) in a backward pumped distributed Raman fiber amplifier.

This chapter is based on Refs. [95–97]

4.1 Review of recent work on multi-mode Raman fiber amplifiers

Recent SDM transmission system experiments have included discrete few-moded Erbium-doped fiber amplifiers (EDFAs) and distributed Raman fiber amplifiers. In 2012, N. Bai *et al.* investigated in [98] a few-moded EDFA that supported three spatial modes, LP01, LP11a and LP11b. Here and in the following, the notion of LP modes refer to scalar linearly polarized modes as they exist in weakly guiding stepindex optical fibers [61]. The amplifier was used to boost the signal just before the input of the receiver. The impact of using different spatial pump modes was considered and the MDG, i.e. the difference in gain between the LP01 and the LP11a and LP11b modes across the entire C-band, was shown to be 1 dB when the pump power was in the LP21 mode for an average modal gain of $\sim$ 7 dB. V.A.J.M Sleiffer *et al.* demonstrated in [99] the use of an in-line few-moded EDFA, providing gain for the spatial modes: LP01, LP11a and LP11b. The amplifier provided a modal gain of around 17 dB across the full C-band with a MDG close to 2 dB.

R. Ryf and co-workers demonstrated in 2011 [49] the use of distributed Raman amplification to counteract loss in a 137 km long FMF. The signals were situated in both the LP01-mode and the LP11-mode while the pump was launched only into the LP11-mode. The Raman fiber amplifier used in their experiment provided a maximum gain of about 8 dB in the wavelength range from 1550 nm to 1570 nm with a variation in gain between modes of less than 0.5 dB. In 2012, R. Ryf and *et al.* [52] showed a transmission through a 209 km long FMF using distributed Raman gain to counterbalance intrinsic fiber loss. The signal consisted of polarization multiplexing of the three spatial modes LP01, LP11a and LP11b. The backward pumped distributed Raman fiber amplifier provided around 10 dB of gain at 1550 nm, obtained by using 800 mW of pump power coupled into the LP11 mode.

As already pointed out, one challenge in using optical FMF amplifiers is the MDG. In discrete Erbium-doped fiber amplifiers, Q. Kang *et al.* [100] have proposed a fiber design that has enabled a 6 mode group amplifier providing a gain around 25 dB for all 6 modes with a maximum gain difference among the 6 modes of only 0.6 dB. R. Ryf *et al.* analyzed MDG theoretically in a distributed Raman fiber amplifier in [101]. Among four mode groups a MDG of 0.13 dB, for a Raman gain of 10 dB on each signal mode group, was predicted. To achieve this result, the pump power was distributed among two different mode groups.

The task of minimizing the difference in gain among different signal modes at different signal wavelengths is a challenging problem. The solution is either to optimize the fiber design for minimum MDG [102] or to adjust the configuration of the pump at the amplifier input; for example distributing the pump power among different wavelengths or spatial modes. For the latter solution, a numerical approach to optimizing the pump power distribution in different spatial modes has been proposed by J. Zhou in [51], and an experimental approach has been proposed by Christensen *et al.* where a minimum MDG of 0.25 dB per 10 dB gain was demonstrated [97].

In analogy to the MDG, the noise performance of few-mode amplifiers is also mode dependent. However, evaluating the gain and noise performance is further complicated since the power distribution within individual modes, be it signal or pump modes, may shift during propagation. This linear and distributed mode coupling is not caused by the amplifying mechanism but for example due to small perturbations in the fiber, splices between fiber segments, or due to the fact that scalar LP modes, as is considered in the following, are composed of several spatial and polarization degenerate modes that couple strongly to each other during propagation. Thus, mode coupling exist in space division multiplexed systems even without amplification. This type of coupling is deterministic in nature and may be mitigated by using MIMO techniques [103]. However, the complexity of using MIMO scales quadratically with the number of modes and even though the impact of mode coupling may be mitigated, mode coupling still results in a transmission penalty [104]. Consequently low linear mode coupling is desirable [104–106].

Another class of mode coupling is random linear mode coupling (RLMC) that happens because of stochastic perturbations along the fiber, as for example stochastic mechanical perturbations or temperature perturbations; the impact of RLMC in a single amplifier is a new noise source introduced in multi-mode systems. RLMC cannot be mitigated by MIMO and its impact is enhanced in amplifiers as for example a Raman fiber amplifier [107]. The reason for this is that in a system relying on distributed Raman amplification, the random mode coupling not only impacts the statistics of the output power of the signal due to mode dependent loss but even more dramatically, the signal is impacted by a random distributed mode coupling of the pump power as it couples between different modes each having a different Raman gain coefficient to individual modes.

As a means to minimize linear mode coupling, deterministic as well as random mode coupling, a fiber may be designed with a large separation between the effective refractive index of each mode. This has been

investigated by L. Grüner-Nielsen *et al.* [104] and K. Jespersen *et al.* [108] and likewise its impact on the Raman gain [69] by C. Antonelli *et al.*. It has been demonstrated that the linear mode coupling decreases with increasing mode index difference, and it has been demonstrated that an index difference of $\Delta n = 1.3 \cdot 10^{-3}$ result in a linear mode coupling of -18.2 dB, measured in a 500 m fiber, whereas an index difference of $\Delta n = 2.8 \cdot 10^{-3}$ reduces the linear mode coupling to -25 dB, measured in a 30 km long fiber [104, 108].

4.2 Random linear mode coupling in a two-mode Raman fiber amplifier

In this section, a model for calculating the induced excess noise of distributed few-mode Raman fiber amplifiers due to linear mode coupling in the pump is presented. A scheme with parameters that may be derived from experimental data is presented, and the results are quantified in terms of mode differential gain and an induced noise figure (NF). Since deterministic mode coupling in the signal can be well mitigated by MIMO processing [103], only mode coupling among the pump modes is included; and because little is usually known about where in the fiber mode coupling takes place, the pump mode coupling is as a first approximation regarded to be of random nature. Amplified spontaneous emission is omitted from the investigation for simplicity and should thus be considered an additional source of noise. The model of linear mode coupling is defined to represent the weak coupling regime where only a small amount of electromagnetic energy is expected to couple from one pump mode to another while propagating through the fiber; this is in contrast to earlier works that focus on the strong coupling regime [109–111].

4.2.1 Theory of inter-modal Raman amplification

Inter-modal stimulated Raman scattering is described using the general propagation equation Eq. (2.50). The nonlinear induced polarization is written as [66]

$$\mathbf{P}^{(3)}(\mathbf{r},t) = \epsilon_0 \chi^{(3)} \mathbf{E}(\mathbf{r},t) \int R(t-\tau) |\mathbf{E}(\mathbf{r},t)|^2 d\tau \tag{4.1}$$

where only one component of the susceptibility tensor $\chi^{(3)}_{ijkl}$ is included, i.e. the $\chi^{(3)}_{iiii} \equiv \chi^{(3)}$ where $i = x$ or y and $\chi^{(3)}$ is the total susceptibility (sum of Kerr and Raman susceptibilities). The response function is $R(t) = \frac{3}{2} f_R h_R(t)$ where $f_R = 0.18$ is the Raman fraction of the total

susceptibility and $h_R(t)$ is the normalized time domain Raman response, which is parameterized as shown in Ref. [70]. The analysis is simplified if it assumed that all electric fields are linearly polarized such that $\mathbf{F}_n^{(\mu)} = F_n^{(\mu)}\hat{\mathbf{x}}$ where $\hat{\mathbf{x}}$ is a unit vector in the x direction; this simplification is convenient for communication fibers, which are often weakly guiding. First inserting the electric field expansions Eqs. (2.37) and (2.38) into Eq. (4.1) and only collecting terms that oscillate at ω_n; then inserting Eq. (4.1) into the general propagation equations and using that terms that require phase matching fall out, the final propagation equation becomes (see Ref. [112] for a similar process)

$$\frac{\partial E_n^{(\mu)}}{\partial z} = \frac{i\omega_n n_2 f_R}{c} E_n^{(\mu)} \sum_m \sum_\nu f^{(\mu,\nu)} |E_m^{(\nu)}|^2 \tilde{h}_R(\Omega_{mn}) \tag{4.2}$$

where $n_2 = 3\chi^{(3)}/(4\epsilon_0 c n_{\text{eff}}^2)$ where n_{eff} is the effective index of mode μ at frequency ω_n, $f^{(\mu,\nu)}$ is the nonlinear mode overlap integral defined as in Ch. 2

$$f^{(\mu,\nu)} = \frac{\int |F^{(\mu)}|^2 |F^{(\nu)}|^2 dxdy}{\int |F^{(\mu)}|^2 dxdy \int |F^{(\nu)}|^2 dxdy}, \tag{4.3}$$

where the subscript on $F_{(\mu)}$ was removed, thus assuming that the field distribution functions are equal at all wavelengths; since no wave components in this work (and for Raman amplifiers in silica in general) are separated by more than ca. 100 nm, this is a decent approximation. The function $\tilde{h}_R(\Omega_{mn})$ [70] is the frequency domain Raman response function; $\Omega_{mn} = \omega_m - \omega_n$ is the frequency shift from ω_n to ω_m. The set of equations (4.2) are readily converted to power by multiplying with the complex conjugate modal field amplitude $E_n^{(\mu)^*}$ and adding the complex conjugate of the resulting equation to itself, i.e.

$$\begin{aligned} \frac{\partial P_n^{(\mu)}}{\partial z} = &-\alpha_n^{(\mu)} P_n^{(\mu)} + \frac{2i\omega_n n_2 f_R}{c} P_n^{(\mu)} \\ &\times \sum_m \sum_\nu f^{(\mu,\nu)} P_m^{(\nu)} \text{Im}\{\tilde{h}_R(\Omega_{mn})\}, \end{aligned} \tag{4.4}$$

where $|E_n^{(\mu)}|^2 = P_n^{(\mu)}$ was used. The usual linear loss term with attenuation coefficient $\alpha_n^{(\mu)}$ was added by hand to account for distributed fiber losses. The two degenerate modes LP11a and LP11b form a mode group, which makes them more strongly coupled to each other than to modes outside the mode group. To take this unavoidable mode coupling into account one may average the Raman terms of the LP11a and LP11b in

Eq. (4.4) by assuming that through a small piece of fiber, the propagating light has spent approximately equal time in both modes [69]. Such an averaging is not necessary in our modeling since an ensemble that approximately represents the whole LP11 mode space (i.e. all combinations of LP11a and LP11b) is propagated through the fiber; thus, the average of the ensemble represents the same value that comes out of the averaged Raman propagation equations of Ref. [69].

4.2.2 Two mode-group system

Several experiments of transmitting data through few-mode fibers have been conducted [52, 113] and distributed Raman amplification has been used to mitigate fiber attenuation [49]. Based on Eq. (4.4) conditions for achieving equal modal gain in a system of two mode groups, LP01 and LP11, are derived. As stated above, only one state of polarization is considered. If a signal s at a single wavelength is amplified by a pump p at a single wavelength both occupying the three spatial mode in a loss-less fiber, then in the undepleted pump regime, the solutions for the signal modes are all on the form

$$P_{\mathrm{s}}^{(\mu)}(z) = P_{\mathrm{s}}^{(\mu)}(0)\mathrm{e}^{G^{(\mu)}z}, \tag{4.5}$$

where

$$G^{(\mu)} = \frac{2\omega_s n_2 f_R}{c}\mathrm{Im}\{\tilde{h}_R(\Omega_{\mathrm{ps}}\}\sum_{\nu} f^{(\mu,\nu)}P_{\mathrm{p}}^{(\nu)} \tag{4.6}$$

and $P_{\mathrm{p}}^{(\mu)}$ is the constant power of pump mode μ. Equating the gain of the LP11a and LP11b modes and using that $f^{(11a,11a)} = f^{(11b,11b)} \equiv f^{(11,11)}$ one gets

$$\left(f^{(11,11)} - f^{(11a,11b)}\right)\left(P_{\mathrm{p}}^{(11a)} - P_{\mathrm{p}}^{(11a)}\right) = 0, \tag{4.7}$$

from which it is immediately concluded that $P_{\mathrm{p}}^{(11a)} = P_{\mathrm{p}}^{(11b)}$ since $f^{(11,11)}$ and $f^{(11a,11b)}$ are rarely similar. Then equating the gains of the LP01 and LP11a modes, the condition for equal gain in all three modes becomes

$$P_{\mathrm{p}}^{(11a)} = \frac{f^{(01,01)} - f^{(01,11)}}{f^{(11,11)} + f^{(11a,11b)} - 2f^{(01,11)}}\,P_{\mathrm{p}}^{(01)} \tag{4.8}$$

where $f^{(01,11a)} = f^{(01,11b)} \equiv f^{(01,11)}$ was used. It follows from this results that $f^{(11,11)} + f^{(11a,11b)} > 2f^{(01,11)}$ is a requirement for equal gain to be possible, since $f^{(01,01)} > f^{(01,11)}$ always applies in circular symmetric

fibers; if this condition is not met in a given fiber, equal gain among LP11a and LP11b is still achievable for $P_{\mathrm{p}}^{(11a)} = P_{\mathrm{p}}^{(11b)}$.

In a situation where the equal gain condition is not met by the fiber but equal gain among LP01 and LP11a(b) is desired, the power of LP11b(a) must be zero, and the power of LP11a(b) becomes

$$P_{\mathrm{p}}^{(11a)} = \frac{f^{(01,01)} - f^{(01,11)}}{f^{(11,11)} - f^{(01,11)}} P_{\mathrm{p}}^{(01)}. \tag{4.9}$$

A transparent transmission line, i.e. each of the output signal modal powers equal each of the input signal modal powers, is achieved by using Eq. (4.8), equating the LP01 signal gain and the total loss, and assuming that all pump and signal modes have the same attenuation coefficient, α_{p} and α_{s}, respectively. The LP01 pump input power is then found to be

$$P_{\mathrm{p}}^{(01)} = \frac{\alpha_{\mathrm{s}} L}{\bar{\gamma} L_{\mathrm{eff}}}, \tag{4.10}$$

where L is the fiber length, $L_{\mathrm{eff}} = [1 - \exp(-\alpha_{\mathrm{p}} L)]/\alpha_{\mathrm{p}}$ is the effective fiber length, and

$$\bar{\gamma} = \frac{2 n_2 \omega_{\mathrm{s}}}{c} \left[f^{(01,01)} + \frac{2\left(f^{(01,01)} - f^{(01,11)}\right) f^{(01,11)}}{f^{(11,11)} + f^{(11a,11b)} + 2 f^{(01,11)}} \right] \times f_R \mathrm{Im}\{\tilde{h}_R(\Omega_{\mathrm{ps}}\}. \tag{4.11}$$

The two mode-group system described here is investigated numerically by solving the set of equations (4.4) using a 4th order Runge-Kutta algorithm through an $L = 100$ km fiber in 50 steps with a nonlinear index $n_2 = 2.6 \times 10^{-20}$ m^2/W, an LP01 effective area $A_{\mathrm{eff}}^{(01)} = 80$ μm^2, realistic nonlinear mode overlaps $f^{(01,11)} = 0.5 f^{(01,01)}$, $f^{(11,11)} = 0.76 f^{(01,01)}$, $f^{(11a,11b)} = 0.3 f^{(01,01)}$ [114], common attenuation coefficients $\alpha_{\mathrm{p}} = \alpha_{\mathrm{p}} = 0.2$ dB/km, pump and signal wavelengths $\lambda_{\mathrm{p}} = 1450$ nm and $\lambda_{\mathrm{s}} = 1550$ nm, and LP01 and LP11a and b pump powers from Eq. (4.10) and (4.9), respectively.

The result is shown in Figure 4.1: the top plot shows the power evolution of all six fields in the undepleted pump regime; all the signal modes are indistinguishable in the plot as a consequence of the equal gain condition calculated above, and the LP11a and LP11b pumps are indistinguishable because they follow identical equations when their attenuation coefficients and all signal powers are equal. In the top plot, a signal input power of $P_{\mathrm{s}}^{(01)} = P_{\mathrm{s}}^{(11a)} = P_{\mathrm{s}}^{(11b)} = P_{\mathrm{s,in}} = -10$ dBm was used and since the pumps remain essentially undepleted by the signals,

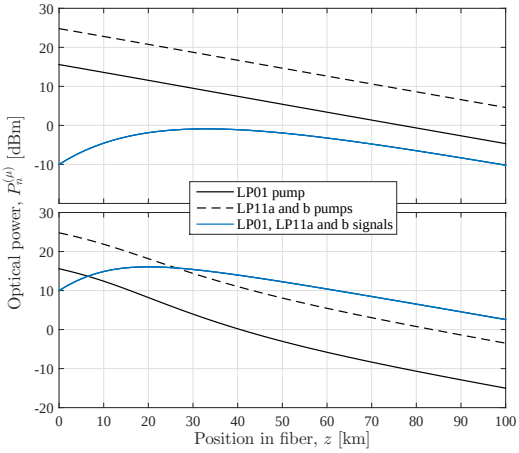

Fig. 4.1: Power evolution through fiber operated in the linear gain regime (top) and in the depleted pump regime (bottom); the curves for the LP11a and b pumps, and the curves for the LP01, LP11a and b signals, repsectively, are indistinguishable in the plot.

the transmission line is transparent as dictated by Eq. (4.10). In the bottom plot, the signals were initiated with a power of $P_{\mathrm{s,in}} = 10$ dBm and the pumps are immediately affected and start to deplete; consequently, not enough energy remain in the pumps to compensate for the attenuation in the rest of the fiber, and hence the signals arrive with almost 10 dB lower power than at input.

4.2.3 Random linear mode coupling

Mode coupling has been modeled in different ways [110, 115, 116] but the mechanisms behind mode coupling are presently not well understood [117]. Therefore, it is difficult to define properties of couplings taking place at specific positions in the fiber. In practice one needs to measure the output modal contents—e.g. by S^2 measurements [118]—with little knowledge about where in the fiber the coupling has taken place. Hence, a numerical investigation of the statistical properties of the mode coupling must treat the fiber as a series of statistically identical sections. Since the pump must be assumed to take many different modal combinations through the fiber—due to both deterministic and random mode coupling—and an amplified signal experiences many of these, it is assumed that all mode coupling in the pump can be viewed as random. Thus, mode coupling in the pump is modeled as a transfer of a random proportion of the total mode power to other modes; since the weak coupling regime is considered it is implied that only a fraction

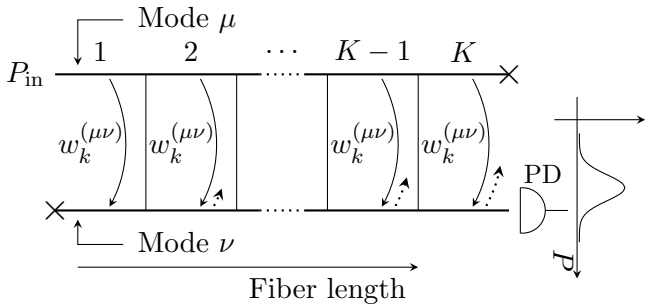

Fig. 4.2: Illustration of the random linear mode coupling model: the two horizontal lines represent two fiber modes in which the fields couple with mean rate $w_k^{(\mu\nu)}$ in each section. The plot is a sketch of the power probability density in mode ν given the overall coupling degree $w^{(\mu\nu)}$ and standard deviation $\sigma^{(\mu\nu)}$. The dashed arrows indicate possible backcoupling, which is neglected in the model. PD, photo detector.

of the light in a given mode has changed to another mode through the entire fiber. The fiber sections are assumed uncorrelated, which implies that the correlation length of the perturbations that are responsible for mode coupling is much shorter than the length of one section. By choosing a suitable coupling probability distribution, the parameters of the individual, identical sections are calculated directly from the measurable output power statistics of the modes that were coupled to. Hence, the degree of mode coupling between two modes is a stochastic variable but it is calculated through a well-defined mean and variance.

The model of RLMC is illustrated in Figure 4.2: light is initiated only in mode μ and in each step a random proportion with mean value $w_k^{(\mu\nu)}$ of the power in mode μ couples to mode ν. The random proportion of power that couples must be chosen from a probability distribution that has support on the continuous interval $[0, 1]$; the Beta distribution is often used to model random proportions [119],

$$\text{Beta}(x|a,b) = \frac{x^{a-1}(1-x)^{b-1}}{B(a,b)}, \tag{4.12}$$

where $B(a,b)$ is a normalization constant. The stochastic variable x is the random proportion of power that changes mode, and it has the properties

$$\langle x \rangle = \frac{a}{a+b} \equiv w_k^{(\mu\nu)} \tag{4.13}$$

$$\langle (x - \langle x \rangle)^2 \rangle = \frac{ab}{(a+b)^2(a+b+1)} \equiv \sigma_k^{(\mu\nu)^2}, \tag{4.14}$$

where $w_k^{(\mu\nu)}$ and $\sigma_k^{(\mu\nu)}$ are the mean value and the standard deviation of the random coupling in the identical sections, and a and b are positive shape parameters. At the output of the fiber, the power mean value and standard variation in mode ν can be measured, and relative to the mean input power they are named the overall coupling degree $w^{(\mu\nu)}$ and overall standard deviation $\sigma^{(\mu\nu)}$, where superscript $(\mu\nu)$ denotes that the parameter belongs to coupling between mode μ and ν. This procedure may be repeated for any number of modes. The connection between $w^{(\mu\nu)}$, $\sigma^{(\mu\nu)}$, $w_k^{(\mu\nu)}$, and $\sigma_k^{(\mu\nu)}$ is simple because the output in mode ν is a sum of a large number of independent, identically distributed random numbers so due to the Central Limit Theorem, the output is normally distributed and the mean value and variance are the sums of the mean values and variances of each section, so

$$w_k^{(\mu\nu)} = w^{(\mu\nu)}/K \tag{4.15}$$

$$\sigma_k^{(\mu\nu)} = \sigma^{(\mu\nu)}/\sqrt{K}, \tag{4.16}$$

where K is the number of sections, which is a numerical parameter that must be assumed to be large, e.g equal to the number of steps in the numerical algorithm for solving the set of equations (4.4). In the relations (4.15) and (4.16), it was assumed that no significant amount of light couples back to the initial mode as shown by the dashed arrows in Figure 4.2 that points from mode ν to mode μ. From simulations not shown here, it is found that this approximation is fair as long as $w^{(\mu\nu)} < 0.1$, which underlines that the simple interpretation of $w^{(\mu\nu)}$ and $\sigma^{(\mu\nu)}$ is valid only in the weak coupling regime. The linearity of the random mode couplings implies that the model is valid in the depleted pump regime as well as in the undepleted pump regime.

4.3 Impacts of pump mode coupling and pump depletion

To quantify the amount of noise that mode coupling in the pump adds during amplification, the input signal must be initiated with a well defined signal-to-noise ratio (SNR). The number of photons in a coherent state follows a Poisson distribution [86], so an input ensemble of fields in every mode of both pump and signal is generated by calculating the mean number of photons, $\bar{n}_n^{(\mu)}$, pull out 20×10^3 numbers from a Poisson distribution with $\bar{n}_n^{(\mu)}$ as the mean number, and then convert every element back to optical power units as done in Sec. 3.2.1.

The signal-to-noise ratio, SNR, is defined at every point in the fiber as

$$\mathrm{SNR}_n^{(\mu)} = \frac{\langle P_n^{(\mu)} \rangle^2}{\mathrm{Var}\left(P_n^{(\mu)}\right)} \tag{4.17}$$

and the mode coupling-induced noise figure (NF) is defined as the relative change in SNR, $\mathrm{NF} = \mathrm{SNR}_{\mathrm{input}}/\mathrm{SNR}_{\mathrm{output}}$. In the two mode-group case already considered, six ensembles are propagated in parallel through Eqs. (4.4).

4.3.1 Mode-dependent Gain

Recent works have focused on the possibilities of achieving mode equalized gain [49, 51, 102] using theory similar to what is presented above. However, it remains unclear what the impacts of pump depletion and pump mode coupling are on the NF and the prospects of achieving mode-equalized gain in Raman fiber amplifiers, which is what is investigated here: simulations both with and without inter-mode-group mode coupling is conducted such that firstly only the LP11a and LP11b in the pump couples (intra-mode-group mode coupling); secondly, also the LP01 mode couple to the LP11 mode-group (inter-mode-group mode coupling).

In the model of weak RLMC, all modes need not couple to the same overall degree, and indeed intra-mode-group mode couplings in the LP11 mode-group are expected to be stronger than inter-mode-group mode couplings between LP01 and LP11 mode-groups. Initially, it is assumed that inter-mode-group mode coupling is negligible and simulations in the same fashion as in Figure 4.1 is done; both the signal input power and the degree of intra-mode-group mode coupling, $w^{(11a,11b)}$, are varied; the pump mode powers are again chosen to satisfy equal modal gain in all signal modes and to make the transmission line transparent.

Figure 4.3 shows the MDG, i.e. the signal gain of LP11a (blue solid) and LP11b (green dashed) relative to the gain of LP01, respectively. The many curves of each mode represent a range of different $w^{(11a,11b)}$ values from -40 dB to -10 dB; no significant difference can be observed in this interval. In the undepleted gain regime, the MDG is fluctuating around zero as expected from the equal modal gain conditions; in the depleted pump regime ($P_{\mathrm{s,in}} > -5$ dBm), an increasing MDG is observed but it is still somewhat smaller than the lowest MDG of few-mode Raman amplifiers measured in the undepleted pump regime toady of 0.25 dB per 10 dB gain [97]. Our analysis shows that intra-mode-group mode

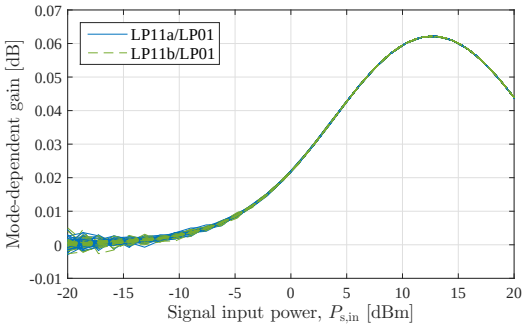

Fig. 4.3: lP11a (blue solid) and LP11b (green dashed) relative to LP01 mode-dependent signal gain vs. signal input power, $P_{\mathrm{s,in}}$; the many curves in each mode represents a range of different $w^{(11a,11b)}$ values from -40 dB to -10 dB.

coupling in the pump plays a minor role for MDG even in the depleted pump regime.

Next, inter-mode-group mode coupling is included by setting the degree of inter-mode-group mode coupling, $w^{(01,11)}$, to be non-zero. The degree of intra-mode-group mode coupling $w^{(11a,11b)}$ is kept at the maximum value of -10 dB since in all cases the intra-mode-group couplings must be stronger than the inter-mode-group couplings. Figure 4.4 shows the MDG of all three signal modes at $w^{(01,11)} = -40$ dB, $w^{(01,11)} = -25$ dB, and $w^{(01,11)} = -10$ dB relative to the LP01 signal gain at $w^{(01,11)} = -40$ dB, which is so low that all behavior is expected to be the same as if it was not present. These values of $w^{(01,11)}$ are equivalent to those demonstrated in the literature of -18.2 dB [108] and -25 dB [104].

Indeed, the MDG curves of LP11a and LP11b (middle and bottom plots) at $w^{(01,11)} = -40$ dB are very similar to those in Figure 4.3; the same are those at $w^{(01,11)} = -25$ dB, which means that an inter-mode-group mode coupling degree of -25 dB in the pump is not detectable in the LP11 mode-group in our analysis even in pump depletion. For the LP01 mode (top plot), however, a slight increase in gain relative to the $w^{(01,11)} = -40$ case is observed; at $w^{(01,11)} = -10$, the increase in MDG is 0.3 dB, which cf. [97] might be detectable experimentally. The reason for this increase in gain for larger values of $w^{(01,11)}$ is that light is transferred between the to mode groups; indeed, light couples between the LP01 mode and the LP11 mode group to the same degree in our model but the LP11 pumps are initiated much stronger than the LP01 pump, as is evident in Figure 4.1, to obey the equal modal

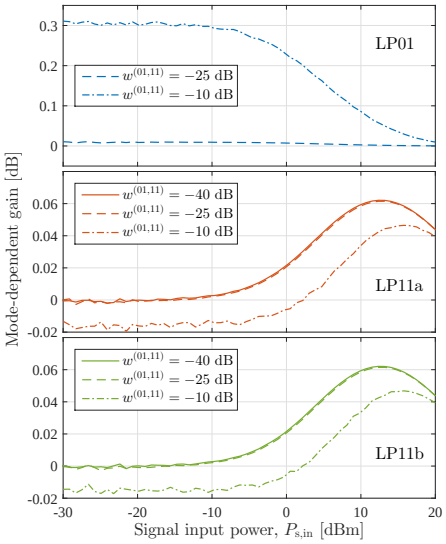

Fig. 4.4: Mode-dependent gain vs. signal input power $P_{\mathrm{s,in}}$ in modes LP01 (top), LP11a (middle), and LP11b (bottom) for different degrees of inter-mode-group mode coupling $w^{(01,11)}$ relative to the LP01 gain at $w^{(01,11)} = -40$ dB.

gain condition. Hence, effectively light is coupled from the LP11 mode group to the LP01 mode and that causes the gain in the LP01 signal to increase. That is also the reason that the LP11a and LP11b MDG have decreased in Figure 4.4 for increased values of $w^{(01,11)}$. As the pump depletes, however, these tendencies disappear because the pumps are saturated before the mode coupling effectively takes place.

The effects described in Figs. 4.3 and 4.4 are clearly visible in the plots but are of very modest magnitude. Hence our analysis has shown that weak linear mode coupling in the pump (coupling degrees between modes up to -10 dB) has only a minor impact on the conditions for equal modal gain in distributed Raman amplifiers even in the depleted pump regime.

4.3.2 Pump mode coupling induced noise figure

The noise properties of few-mode Raman fiber amplifiers are important for their potential in future optical communication systems; one of the great advantages of backward-pumped single-mode Ramam fiber amplifiers is their superior noise properties to EDFAs [16] If few-mode Raman fiber amplifiers are to be used in communication systems, the presence of mode coupling should not introduce too much excess noise.

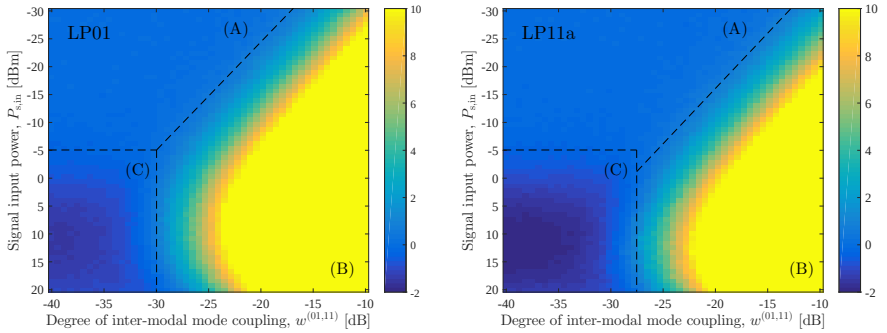

(a) (b)

Fig. 4.5: NF vs. overall degree of inter-modal mode coupling w_2 and input signal power $P_{\mathrm{s,in}}$ (undepleted pump regime top, and depleted pump regime bottom) for LP01 (a) and LP11a(b). Three separate regions (A)–(C) with different characteristics are identified; see the text.

In this section, only a forward pumped few-mode Raman fiber amplifiers is modeled due to the difficulties of applying statistical models in the backward pumped configuration.

The NFs of all three signal modes are evaluated using Eq. (4.17); if inter-mode-group mode coupling is neglected, i.e. $w^{(01,11)} = 0$ as in Figure 4.3, no mode coupling induced NF for any $w^{(11a,11b)}$ values are found in the undepleted pump regime (the depleted pump regime is discussed below). The reason is that the LP11 pumps were initiated with the same power according to the equal gain condition so therefore no light is effectively transferred between the two modes; however the randomness of the mode coupling induces an increased power variance in the pumps which consequently increases the variance in the signal and hence the NF but this effect is not strong enough to matter in the weak coupling regime. If the pumps are initiated with asymmetric power, a larger NF is indeed induced as verified in simulations not shown here.

Including inter-mode-group mode coupling, the induced NF of the LP01 and LP11a signals are shown in Fig. 4.5(a) and (b) as functions of signal input power and the degree of inter-mode-group mode coupling $w^{(01,11)}$; the data are extracted from the same simulation that produced Figure 4.4; the color bar shows the NF in dB. The NF for LP11b is indistinguishable from that of LP11a so it is omitted here.

In both figures, the NF in $(P_{\mathrm{s,in}}, w^{(01,11)})$-space can be divided in three regions with different characteristics, A, B, and C. Region A is the regime that corresponds to usual single-mode operation; the pump is undepleted and mode coupling is so low that the modes approximate separate single mode channels (intra-mode-group mode coupling is still

$w^{(11a,11b)} = -10$ dB). In this regime, the mode coupling induced NF is predicted to be zero; the mode coupling is simply too small to matter. In region B, the NF increases to more than 10 dB due to higher inter-mode-group mode coupling; the line between regions A and B shows how much input power in the signals that can be tolerated under a certain degree of mode coupling (given the input powers used in our simulation). The line has a positive slope in $(P_{\mathrm{s,in}}, w^{(01,11)})$-space because the NF becomes more sensitive to mode coupling in the depleted pump regime.

Region C, in which inter-mode-group mode coupling is very small and the amplifier is depleted, contains negative NF values. It was already established above that intra-mode-group mode coupling did not induce any NF in the undepleted pump regime but as the pump depletes the NF becomes negative due to a decrease in the signal power variance. This decrease is a simple consequence of the nature of Raman scattering; when the pump is being depleted, the variance of the signal goes asymptotically towards the variance of the pump power at input because energy only flows from one component to the other. This effect is also predicted [72] and measured [90, 91, 93] in fiber optical parametric amplifiers operated in the depleted pump regime. The line between regions B and C denote the point where inter-mode-group mode coupling becomes so significant that the intensity regenerative property of operating the pump in depletion is destroyed. At this point it is recalled that spontaneous emission is not included in the modeling but that it is well-known that amplified spontaneous emission increases the NF when a Raman amplifier is operated in depletion [120].

The importance of the existence of the low NF region A described here should be seen in light of the fact that the model of the pump fluctuations assumed that all pump mode couplings were completely random. Thus, even the low NF regions represent a worst case scenario of addition of excess noise from pump fluctuations in the weak coupling regime.

It should be noted that regions A and C are slightly larger in Figure 4.5(b) for the LP11 mode group than in Figure 4.5(a) for the LP01 mode, which indicates that signals transmitted in LP11a and LP11b modes are more resistant to the effects of pump mode coupling.

4.4 Experimental investigation of mode-dependent gain in a two-mode Raman fiber amplifier

Focus is now turned to the problem of experimentally achieving equal modal gain. As already discussed above, it is an important challenge

of mode-division multiplexing (MDM) systems to realize optical amplifiers that have mode-equalized amplification of all spatial modes to compensate for example for distributed fiber loss and to maximize capacity [46]. As for traditional single-mode systems, discrete Erbium-doped fiber amplifiers have been applied to multi-mode systems as well and low MDG has been achieved for some of the modes in fibers with specially designed Erbium-doping profiles [48, 121, 122]. The approach for counter-balancing fiber losses discussed in this chapter is distributed Raman amplification, which is widely used already in single-mode networks due to its superior noise properties in the backward-pumped configuration [16]. Furthermore, it has been shown theoretically that minimal MDG is possible by coupling pump power into a specific combination of spatial modes [51], or by designing doping concentrations [50], which makes Raman amplifiers a promising candidate for realizing low-loss, multi-mode transmission links over large distances.

Earlier work has demonstrated Raman gain between higher-order modes with the pump in only one mode [52, 123, 124]. Besides the obvious challenges related to exciting the pump in a specific combination of modes, it may often also prove difficult to determine the exact mode combination that leads to the lowest possible MDG because the required fiber data are unavailable from the fiber supplier. In this section, an experimental characterization of the intermodal Raman intensity overlap of the guided modes of a two-moded few-mode fiber (FMF) using mechanically induced long-period gratings (LPGs) to excite the higher-order modes is presented. Using the obtained results, backward pumped Raman amplification of a continuous wave (CW) signal through 10 km of a two-moded fiber with a very low MDG of 0.25 dB per 10 dB gain is demonstrated by pumping in a combination of the LP01 and LP11 modes. The MDG obtained required no prior knowledge about the Raman intensity overlaps of the fiber.

4.4.1 Inter-modal Raman gain

The goal is now to express the Raman gain of a mode μ in terms of the modal combination of power in the pump of a backward pumped distributed Raman amplifier. The set of equations (4.4) derived in the previous section are valid only for the forward propagating pump but in Ref. [97] it is shown that the signal gain in mode μ is

$$G^{(\mu)} = \exp\left(\gamma_R L_{\text{eff}} \left[\eta_{\text{p}} f^{(\mu,11)} + (1-\eta_{\text{p}}) f^{(\mu,01)}\right] P_{\text{p}}\right), \tag{4.18}$$

where γ_R is proportional to the Raman response $\tilde{h}_R$ of Eq. (4.4), L_{eff} is the effective length defined in Eq. (4.10), η_{p} is the mode conversion

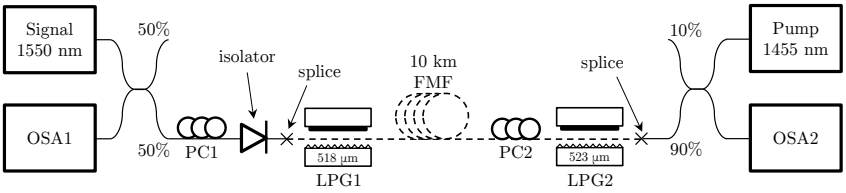

Fig. 4.6: Experimental setup for measuring two-mode Raman gain; full line, single mode fiber; dashed line, two-mode fiber; PC1(2), polarization controller 1(2); LPG1(2), long-period grating 1(2); OSA, optical spectrum analyzer; the number on the LPGs is the gratig pitch.

degree (MCD) of the pump from LP01 to LP11 ($\eta_\mathrm{p} = 0$ when all the pump power is in LP01, and $\eta_\mathrm{p} = 1$ when all the pump power is in LP11) and P_p is the total input pump power in all modes.

4.4.2 Experimental setup

The intermodal Raman gain is measured using the experimental setup shown in Fig. 4.6. The setup is a distributed backwards pumped two-mode Raman amplifier with a CW laser operated at 1550 nm as the signal source and an unpolarized 1455 nm Raman fiber laser the pump source. The fiber characterized here is a 10 km, 2-moded graded-index fiber. The polarization controller 1 (PC1) allows for adjusting the polarization of the input signal before the first long-period grating (LPG1), which is polarization dependent. The isolator protects the OSA and signal source from the strong backward propagating pump. The splice is between a single-mode fiber and the FMF under investigation

The excitation of the LP11 mode is achieved by use of mechanically induced LPG. The LPG is created by pressing the fiber between a periodically grooved aluminum block and a rubber pad. This creates a periodic perturbation in the fiber index, which induces mode coupling if the pitch of the induced gratings matches the difference in propagation constants of the modes [125]. Using a broadband supercontinuum source at the signal input the mode-converted wavelengths are observed in the OSA2 as a drop in the power spectrum due to the FMF-to-single mode fiber splice working as a mode filter. The effective pitch of the LPG is changed by adjusting the angle of the grooves with respect to the fiber, until maximum mode conversion is achieved at the signal wavelength. The use of a supercontinuum source for calibration is not strictly necessary if the difference in propagation constant for the modes of interest is

known, but it facilitates the excitation process. Based on the knowledge of the propagation constants the pitch for the pump wavelength was calculated to be 527 μm, which is in good agreement with the 523 μm pitch experimentally observed at maximum conversion. More details on the setup is given in Ref. [97].

4.4.3 Results: Raman intensity overlaps

Using the setup in Fig. 4.6, 65 measurements of the signal on/off gain were carried out with 5 different pump MCD and 13 different pump power levels varying from 0 to 1200 mW for each MCD. From the expected form of the gain, Eq. (4.18), a function of the following form was fitted to the data

$$G^{(01)} = (c_1 + c_2\eta_\mathrm{p})P_\mathrm{p}, \tag{4.19}$$

where $G^{(01)}$ in this case has the unit of dB, and c_1 and c_2 are fitting parameters. The result is presented in Fig. 4.7(a) where data and fitting lines are shown at the five different values of η_p. The obtained values for the fitting parameters are $c_1 = 8.50$ dB/W and $c_2 = -4.48$ dB/W. The theoretical expression is in excellent agreement with the obtained data with these values of the fitting parameters. From these values the ratio of the Raman intensity overlaps between the LP01-LP01-modes and LP01-LP11-modes is obtained

$$\frac{f^{(01,11)}}{f^{(01,01)}} = 1 + \frac{c_2}{c_1} = 0.47 \tag{4.20}$$

by comparing Eqs. (4.18) and (4.19). This result agrees well with the value of 0.48 obtained from simulated mode-profiles provided by the fiber supplier. Subsequently, the signal was coupled to the LP11-mode with the highest attainable efficiency, ($\eta_\mathrm{s} > 0.99$ where η_s is the signal MCD), and the pump was converted to the LP11-mode with an efficiency of $\eta_\mathrm{p} = 0.925$ and the Raman gain of the LP11-signal was measured vs. the input pump power. A linear function of the type

$$G^{(11)} = c_3 P_\mathrm{p} \tag{4.21}$$

was fitted to the data. From this the ratio $f^{(11,11)}/f^{(01,01)}$ is calculated, taking into account the pump conversion degree: the slope obtained from the fit to the LP11-LP11-data was $c_3 = 4.74$ dB/W. It is assumed that the overlap integrals are wavelength independent (i.e. that the LP01-LP11 and LP11-LP01 overlaps are identical). By comparison of Eqs. (4.21) and (4.19) to (4.18) it is clear that $c_1 = kf^{(01,01)}$ and $c_3 =$

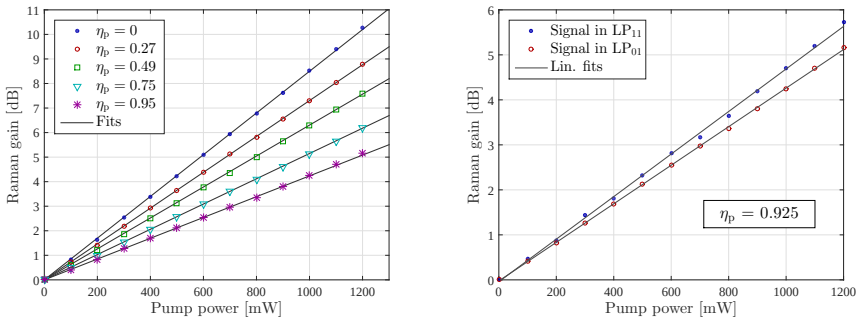

(a) (b)

Fig. 4.7: (a) Measured Raman gain vs. input pump power for five different pump MCD, η_p; the lines result from the two-parameter fit evaluated at each MCD. (b) Measurements of Raman gain for signal and pump in LP11. For comparison is shown the measurement with pump in LP11 and signal in LP01.

$k(f^{(01,11)} + \eta_p(f^{(11,11)} - f^{(01,11)}))$ with $k = 10\log_{10}(e)\gamma_R L_{eff}$. Using Eq. (4.20) for the ratio $f^{(01,11)}/f^{(01,01)}$, these two expressions is rearranged to give [97]

$$\frac{f^{(11,11)}}{f^{(01,01)}} = \frac{c_3}{c_1\eta_p} - \frac{1-\eta_p}{\eta_p}\left(1 + \frac{c_2}{c_1}\right) = 0.56 \tag{4.22}$$

This is compared to the simulated values for LP11a-LP11a and LP11a-LP11b of 0.72 and 0.24, respectively. The measured overlap is, as expected, an intermediate value that depends on the mode coupling within the LP11 mode-group.

4.4.4 Results: equal modal gain

Since the intensity overlaps $f^{(01,11)}$ and $f^{(11,11)}$ often turn out to be very similar in FMFs, relatively low differential gain can be obtained by simply launching the pump completely into LP11. This was experimentally verified by R. Ryf et al. [52] where a differential gain of 0.5 dB per 10 dB of gain was observed. For the fiber used in this work, such a scheme results in a differential gain of 1 dB per 10 dB of gain as obtained from the data shown in Figure 4.8(b) (the differential gain in the figure is slightly lower since the pump is only converted 95 % into LP11). Using our knowledge of the intensity overlap integrals, the condition for equal signal gain across the two signal-modes, $G^{(11)} = G^{(01)}$, can be written as

$$\eta_p f^{(11,11)} + (1-\eta_p) f^{(01,11)} = \eta_p f^{(01,11)} + (1-\eta_p) f^{(01,01)}. \tag{4.23}$$

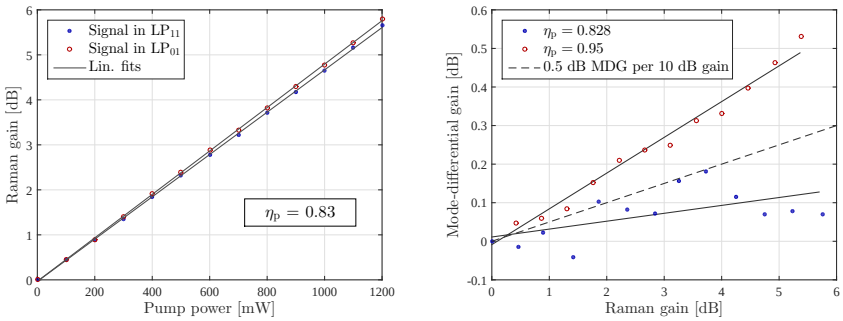

(a) (b)

Fig. 4.8: Raman gain for both a LP01 and LP11-signal with a pump in the mixture of 83 % LP11 and 17 % LP01; (b) mode-differential gain between the two signal modes for pump almost completely converted to LP11 and pump in the mixture of 83 % LP11 and 17 % LP01. A line for 0.5 dB gain difference per 10 dB gain is included for reference.

This equation can be solved, using the experimentally obtained values for the ratios $f^{(11,11)}/f^{(01,01)}$ and $f^{(01,11)}/f^{(01,01)}$, to obtain an equal-gain pump conversion of

$$\eta_{\mathrm{p,eq}} = \frac{1 - f^{(01,11)}/f^{(01,01)}}{1 + f^{(11,11)}/f^{(01,01)} - 2f^{(01,11)}/f^{(01,01)}} = 0.854, \qquad (4.24)$$

where $\eta_{\mathrm{p,eq}}$ is the pump MCD that gives equal modal gain. In Fig. 4.8(a), the results of measuring a signal launched first completely in LP01 and then completely in LP11 with a pump conversion of $\eta_{\mathrm{p}} = 0.83$, i.e. slightly below the optimal value, are shown. From the figure it is clear that very little MDG remains (compare to Fig. 4.7(b)). The MDG as a function of the mean gain is seen in Fig. 4.8(b), showing a residual MDG of only 0.25 dB per 10 dB of Raman gain as obtained from the fitted lines. The reason for the fluctuation in MDG is most likely due to mode coupling between LP11a and LP11b, and the LPG preferentially only couples one of them to the LP01 mode, which is detected in the OSA. This means that any mode coupling between LP11a and LP11b in the amplified signal shows up as a small oscillation on the OSA. In the $\eta_{\mathrm{p}} = 0.83$ measurement (blue dots) the back coupling is slightly more unstable compared to the $\eta_{\mathrm{p}} = 0.95$ measurement (red circle). This is due to the different configuration of the back coupling in LPG2.

4.5 Partial conclusion

In this chapter, two important aspects of few-moded Raman fiber amplifiers were investigated: noise due to random mode coupling in the pump and the challenges of achieving equalized modal gain.

The impact of linear mode coupling in the pump of few-moded distributed Raman fiber amplifiers was analyzed. After deriving basic propagation equations and conditions for equal modal gain and equal input and output signal power, a numerical model of weak random mode coupling was presented. This model was used to analyze the impacts of mode coupling in the pump of a two-mode-group Raman fiber amplifier; in the presence of intra-mode-group mode coupling (LP11a–LP11b coupling) but absence of inter-mode-group mode coupling (LP01–LP11 coupling) a mode-dependent gain < 0.1 dB and no mode coupling induced NF was found. When inter-mode-group mode coupling was included our simulations showed a mode-dependent gain of 0.3 dB when the degree of mode coupling was large (-10 dB); the mode coupling induced noise figure was as large as > 10 dB for increasing degrees of mode coupling; operating in the depleted pump regime tended to increase the mode coupling induced noise figure.

Thereafter, the inter-modal Raman overlaps in a few-mode fiber was characterized experimentally by varying the input pump power and the mode conversion degree of the pump and signal using mechanically induced long-period gratings for mode excitation. The overlap integrals (relative to the LP01-LP01 overlap) for all modal combinations were obtained in this way for a specific two-mode fiber. By use of the obtained overlaps, it was further demonstrated how a mode-dependent gain of only 0.25 dB per 10 dB overall gain is obtained by pumping in a specific combination of the LP01 and LP11 modes.

Chapter 5

Inter-modal four wave-mixing in two-mode fibers

The phase matching requirement of four-wave mixing (FWM) in single-mode waveguides can only be fulfilled by operating all four waves near the zero-dispersion wavelength. The bandwidth of phase matching depends delicately on the dispersion slope and for communication wavelengths near 1550 nm it is only possible to achieve bandwidths much larger than a few nanometers in specially designed highly nonlinear fibers with a very low dispersion slope; separating the signal more than ~ 50 nm from the pump(s) remains difficult due to higher order dispersion terms.

However, if a fiber guides multiple spatial modes each mode is associated with its own propagation constant, which makes phase matching achievable in regimes with large dispersion; the mathematics behind this property is elaborated in Sec. 5.1.3. Further, wave components that are separated hundreds of nanometers may also be phase matched [53, 62, 126]. As explained in the introduction, it remains an critical task in optical communication to avoid excess noise from strong pumps when carrying out signal processing using FWM; especially in the spectral vicinity of any pump is noise a substantial problem, partly due to spontaneous Raman scattering and partly due to pump generation noise (amplified spontaneous emission from e.g. Erbium-doped fiber amplifiers). Inter-modal (IM) FWM enables a pump to be separated from the optical signals while still performing nonlinear processing. The advantage of operating in a regime of large dispersion is that optical signals that are launched in the same mode do not crosstalk through intra-

modal FWM. IM FWM was demonstrated a long time ago by R. Stolen *et al.* [126] at visible wavelengths and has recently been demonstrated by R.-J. Essiambre *et al.* [127, 128] at communication wavelengths but a detailed investigation of the bandwidth of phase matching has not, to the knowledge of the author, been done. In-fiber mode conversion is another application of IM FWM that has been successfully demonstrated recently [129].

In this chapter, two IM-FWM processes are considered (in the scalar approximation throughout the chapter): phase conjugation (PC) and Bragg scattering (BS) as seen in Fig. 3.1(d) and (e). In both cases an LP01 pump (pump 1) and an LP01 signal (s) are launched into the FMF together with a LP11 pump (pump 2), all at different frequencies; an idler is then generated at the frequency determined by the energy conservation of either process in the LP11-mode due to the field overlap conditions discussed in Ch. 2. The aim is to quantify theoretically and experimentally the conversion efficiency (CE) from signal to idler and whether the two schemes agree; also the bandwidth of phase matching is investigated thoroughly. Two fibers with different modal dispersion properties are under investigation, which leads to confirm that IM-FWM is equally effective at different wavelength separations as long as the phase matching conditions are fulfilled. The results of this chapter show that it is indeed feasible to do nonlinear signal processing using IM-FWM.

This chapter is based on and extended from Refs. [94, 130, 131].

5.1 Theory of two-mode four-wave mixing

The two IM-FWM processes under investigation in this chapter, PC and BS, are modeled independently in the first subsection below, while as it turns out that they are not separable under experimental conditions the following section develops a more comprehensive theory that takes six observed processes into account simultaneously. Lastly, the third subsection explains the nature of two-mode phase matching in detail.

5.1.1 Four-field interaction: analytic solutions

The wavelength diagrams of the two FWM processes PC and BS are shown in Fig 3.1(d) and (e) but they are repeated in Fig. 5.1 for clarity with mode designations. The equations that describe PC and BS separately may be derived from the general propagation equation (2.50) derived in Ch. 2 but suitable equations are given directly in Agrawal [56] so they are used here instead. In both cases the two strong pumps are

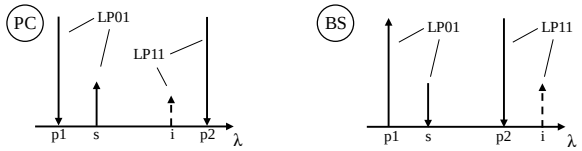

Fig. 5.1: Wavelength configurations of PC and BS with mode designations.

described approximately by the equations

$$\partial_z E_{\mathrm{p1}}^{(01)} = i\frac{n_2\omega_{\mathrm{p1}}}{c}\left(f^{(01,01)}|E_{\mathrm{p1}}^{(01)}|^2 + 2f^{(01,11)}|E_{\mathrm{p2}}^{(11)}|^2\right)E_{\mathrm{p1}}^{(01)} \tag{5.1}$$

$$\partial_z E_{\mathrm{p2}}^{(11)} = i\frac{n_2\omega_{\mathrm{p2}}}{c}\left(f^{(11,11)}|E_{\mathrm{p2}}^{(11)}|^2 + 2f^{(01,11)}|E_{\mathrm{p1}}^{(01)}|^2\right)E_{\mathrm{p2}}^{(11)} \tag{5.2}$$

where it was assumed that the field amplitudes of the signal and generated idler are much smaller than the pump amplitudes, which is a very good approximation in the experiments presented below. For PC, the signal, s, and idler, i, follow the equations

$$\begin{aligned}\partial_z E_{\mathrm{s}}^{(01)} = i\frac{n_2\omega_{\mathrm{s}}}{c}\Big(&2\left[f^{(01,01)}|E_{\mathrm{p1}}^{(01)}|^2 + f^{(01,11)}|E_{\mathrm{p2}}^{(11)}|^2\right]E_{\mathrm{s}}^{(01)}\\ &+2f^{(01,11)}E_{\mathrm{p1}}^{(01)}E_{\mathrm{p2}}^{(11)}E_{\mathrm{i}}^{(11)^*}\mathrm{e}^{-i\Delta\beta z}\Big)\end{aligned} \tag{5.3}$$

$$\begin{aligned}\partial_z E_{\mathrm{i}}^{(11)} = i\frac{n_2\omega_{\mathrm{i}}}{c}\Big(&2\left[f^{(01,11)}|E_{\mathrm{p1}}^{(01)}|^2 + f^{(11,11)}|E_{\mathrm{p2}}^{(11)}|^2\right]E_{\mathrm{i}}^{(11)}\\ &+2f^{(01,11)}E_{\mathrm{p1}}^{(01)}E_{\mathrm{p2}}^{(11)}E_{\mathrm{s}}^{(01)^*}\mathrm{e}^{-i\Delta\beta z}\Big)\end{aligned} \tag{5.4}$$

where $\Delta\beta$ is the phase mismatch calculated below; the signal and idler follow very similar, yet not identical, equations for BS and they become

$$\begin{aligned}\partial_z E_{\mathrm{s}}^{(01)} = i\frac{n_2\omega_{\mathrm{s}}}{c}\Big(&2\left[f^{(01,01)}|E_{\mathrm{p1}}^{(01)}|^2 + f^{(01,11)}|E_{\mathrm{p2}}^{(11)}|^2\right]E_{\mathrm{s}}^{(01)}\\ &+2f^{(01,11)}E_{\mathrm{p2}}^{(11)}E_{\mathrm{i}}^{(11)}E_{\mathrm{p1}}^{(01)^*}\mathrm{e}^{-i\Delta\beta z}\Big)\end{aligned} \tag{5.5}$$

$$\begin{aligned}\partial_z E_{\mathrm{i}}^{(11)} = i\frac{n_2\omega_{\mathrm{i}}}{c}\Big(&2\left[f^{(01,11)}|E_{\mathrm{p1}}^{(01)}|^2 + f^{(11,11)}|E_{\mathrm{p2}}^{(11)}|^2\right]E_{\mathrm{i}}^{(11)}\\ &+2f^{(01,11)}E_{\mathrm{p1}}^{(01)}E_{\mathrm{s}}^{(01)}E_{\mathrm{p2}}^{(11)^*}\mathrm{e}^{i\Delta\beta z}\Big).\end{aligned} \tag{5.6}$$

The field overlaps $f^{(\mu,\nu)}$ are defined in Eq. (2.36). The field profiles are not known in either of the fibers investigated here but the effective areas are. Thus, assuming that the field profiles are approximately Hermite-Gaussian, which decently approximate the Bessel functions discussed in Ch. 2, it is possible to calculate the width of the Hermite-Gaussian

beam from the effective area; the Hermite-Gaussian beam TEM00 is used to approximate LP01 and TEM01 is used for LP11. With the field profiles of both LP01 and LP11 approximated, all field overlaps can be calculated.

Appendix A.2 shows how to solve the equations of a pump degenerate PIA as investigated in Ch. 3; the Eqs. (5.1)–(5.6) are solved very similarly for both PC and BS; since PC is a weak amplification process in this context, the CE rather than the gain is calculated to be

$$\mathrm{CE_{PC}}(z) = \frac{|E_\mathrm{i}(z)|^2}{|E_\mathrm{s}(0)|^2} = \left[\frac{\eta}{g}\sinh(gz)\right]^2, \tag{5.7}$$

where g is the conversion coefficient and η is the IM nonlinearity as defined below. The CE of the BS process from signal to idler is

$$\mathrm{CE_{BS}}(z) = \frac{|E_\mathrm{i}(z)|^2}{|E_\mathrm{s}(0)|^2} = \left[1 - \left(\frac{\kappa}{2g}\right)^2\right]\sin^2(gz), \tag{5.8}$$

where κ is the phase mismatch parameter. The parameters in (5.7) and (5.8) are defined as

$$g^2 = \eta^2 \mp (\kappa/2)^2 \tag{5.9}$$

$$\eta = 2\Gamma f^{(01,11)}\sqrt{P_\mathrm{p1}P_\mathrm{p2}} \tag{5.10}$$

$$\kappa = \Delta\beta \pm \Gamma\left(f^{(01,01)}P_\mathrm{p1} \pm f^{(11,11)}P_\mathrm{p2}\right), \tag{5.11}$$

where '$-$' and '$+$' in g^2 refer to PC and BS, respectively, and vice versa in κ, P_p1 and P_p2 are the constant powers of pump 1 and 2, respectively, $f^{(\mu,\nu)}$ is the intensity overlap between modes μ and ν, and $\Gamma = n_2\omega_0/c$ is the fiber nonlinearity evaluated at frequency ω_0, since the frequency dependence on the fiber nonlinearity was neglected in Eqs. (5.7) and (5.8). These expression may be recognized from standard single-mode cases, only with η and κ different. Note that the highest CE is achieved for $\kappa = 0$ and not $\Delta\beta = 0$. However, for multi-mode fibers $\Delta\beta$ may vary so much with wavelength shift that the nonlinear contribution to κ is a negligible.

Table 5.1 shows the specifications of the two fibers under investigation used for simulations in this and the following section. The relative inverse group velocity (RIGV), i.e. the difference in inverse group velocity between the LP01-mode and the LP11-mode, is found from measurements in Sec. 5.2.1. The dispersion $D^{(\mu)}$ and the the dispersion slopes $S^{(\mu)}$ at 1550 nm of each mode is achieved by simulations from the fiber supplier, and the overlaps $1/f^{(\mu,\nu)}$ are determined as explained

	RIGV $\left[\frac{\text{ps}}{\text{km}}\right]$	$D^{(01)}$ $\left[\frac{\text{ps}}{\text{km nm}}\right]$	$D^{(11)}$ $\left[\frac{\text{ps}}{\text{km nm}}\right]$	$S^{(01)}$ $\left[\frac{\text{ps}}{\text{km nm}^2}\right]$	$S^{(11)}$ $\left[\frac{\text{ps}}{\text{km nm}^2}\right]$
F1	*96*	19.8	21.9	0.068	0.063
F2	*500*	20.2	20.2	0.0663	0.0649

	$1/f^{(01,01)}$ [μm^2]	$1/f^{(11,11)}$ [μm^2]	$1/f^{(01,11)}$ [μm^2]	L [km]
F1	161	170	**258**	1
F2	**96.7**	**187**	**193**	1

Table 5.1: Specifications of Fiber 1 (F1) and 2 (F2) at $\lambda = 1550$ nm; the relative inverse group velocity (RIGV) is the difference in inverse group velocity between LP01 and LP11, $D^{(\mu)}$ and $S^{(\mu)}$ are the dispersion and dispersion slope, respectively, of mode μ, and $1/f^{(\mu,\nu)}$ is the overlap/effective area of modes μ and ν. Regular font numbers are simulated valued from the fiber supplier; bold font numbers are calculated as explained in the text; italic font numbers are measured in Sec. 5.2.1.

above. The two main differences between the two fibers are the much larger RIGV of the LP01-modes and LP11-modes and that the modal dispersions are more equal in Fiber 2, as compared to Fiber 1. As will become clear in Sec. 5.1.3, these two properties leads to larger separation between the interacting waves of the IM-FWM and a different signal bandwidth. For Fiber 2, a more comprehensive set of simulated dispersion data was available and hence Fig. 5.2 shows (a) the inverse group velocities of the two modes and (b) the difference in dispersion between the two modes. The absolute dispersion data are also available but it is the difference between them that determines the bandwidth of phase matching. It is the data shown in Fig. 5.2 that is used to do simulations of Fiber 2.

Figure 5.3 shows contour plots of the analytic results (5.7) (left) and (5.8) (right) for Fiber 1; the parameters used are $n_2 = 2.6 \times 10^{-20}$ $(\text{W m})^{-1}$, $P_{\text{p1}} = P_{\text{p2}} = 26.5$ dBm, a fiber length of $L = 1$ km, and $\lambda_0 = 1550$ nm in $\omega_0 = 2\pi c/\lambda_0$; the phase mismatch $\Delta\beta$ is calculated as shown in Sec. 5.1.3. On the x- and y-axes are the wavelengths of the LP01 input signal and the LP11 pump 2, respectively, and the LP01 pump 1 has $\lambda_{\text{p1}} = 1549$ nm in all cases.

Much understanding can be gained from the expressions (5.7) and (5.8) but here emphasis is put on the signal bandwidth of phase matching. PC and BS have opposite properties in terms of varying the pump 2 and signal wavelength: in PC, phase matching can be obtained in a nm-sized interval of pump 2 wavelength values but the signal is only

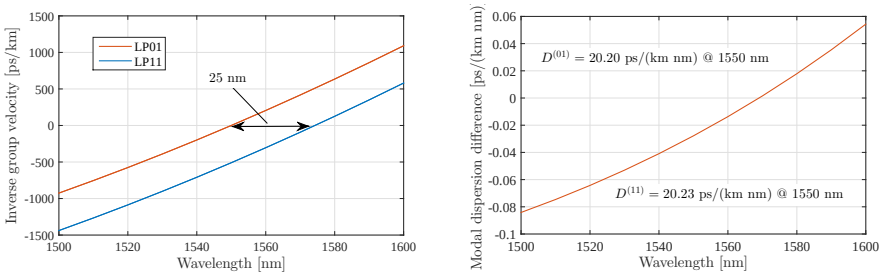

(a) (b)

Fig. 5.2: (a) Inverse group velocity curves of Fiber 2 for LP01 and LP11, where the difference at 1550 nm is 500 ps/km; (b) Modal dispersion difference between LP01 and LP11; the absolute dispersion of each mode is shown at 1550 nm. Data are simulated valued from the fiber supplier.

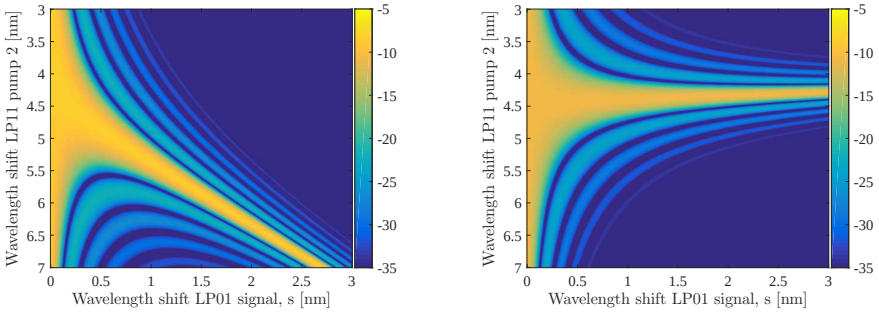

(a) PC; Fiber 1. (b) BS; Fiber 1.

Fig. 5.3: Analytic results of four-field IM-FWM; the color scale show G for PC and CE for BS in linear units; the scaling on the two axes is the same on each of the two PC plots and BS plots, respectively.

phase matched in a very narrow window of width ~ 0.1 nm, and additionally the window center moves with changing pump 2 wavelength. It is notable that PC has one solution to the phase matching condition for pump 2 wavelength shifts below 4.5 nm but above this value it has two; in BS, phase matching is achieved only in one very narrow interval of pump 2 wavelengths, while in this interval the signal bandwidth is much broader. This inverse trend of PC and BE has been predicted before [114] and it is qualitatively elaborated below in Sec. 5.1.3.

As a last remark, it is clear when comparing PC and BS for each of the fibers that the two processes overlap in $(\lambda_s, \lambda_{p2})$ space, which means that they cannot be observed independently in experimental investigations. Therefore, before moving on to the details of the phase matching,

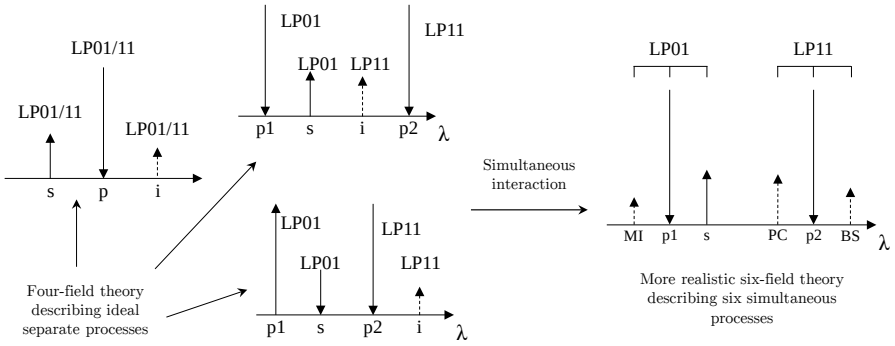

Fig. 5.4: Sketch of how three four-field descriptions, MI (left), PC (top), and BS (bottom), is merged into a six-field description; full lines denote input waves while dashed lines denote generated waves; the different dashed line lengths indicate that the processes occur with different efficiency.

a more comprehensive six-field theory is developed in the next section to gain more accurate theoretical predictions.

5.1.2 Six-field interaction: simulations

So far in this thesis three separate FWM processes have been studied: single-mode MI in chapter 3 and two-mode PC and BS in the previous section. All three are observed simultaneously in the experimental data presented below so a unified description is needed to analyze the data properly. The two approaches that are directly available are using the multi-mode generalized nonlinear Schrödinger equation (MM-GNLSE) [66], which has been done in Ref. [130], or using the general nonlinear propagation equation (2.50) in the CW regime; the latter approach is pursued here.

Figure 5.4 illustrates the idea of the unified theory and also gives the new six-field arrow diagram (right). Many FWM processes take place among six field that can all be in two modes so a few simplifications must be made: firstly, as indicated in the figure, the three lower wavelength components are taken to occupy only LP01 and the three higher wavelength components are taken to occupy only LP11; this is a good approximation partly because the wave components are launched in this configuration and an excellent mode excitation purity has been achieved experimentally (as shown in Fig. 5.13) and partly because IM-FWM processes that involve lower wavelength components in LP11 and higher wavelength components in LP01 are poorly phase matched. Secondly, the two pumps are assumed much stronger than the four side bands so

only FWM processes that involve two pump waves are included.

To use Eq. (2.50) the nonlinear induced polarization must be written down; by studying Fig. 5.4 six remaining processes are identified, two of each of MI, PC, and BS, and they are

$$2\omega_{\mathrm{p1}} = \omega_{\mathrm{s}} + \omega_{\mathrm{MI}} \tag{5.12a}$$
$$2\omega_{\mathrm{p2}} = \omega_{\mathrm{PC}} + \omega_{\mathrm{BS}} \tag{5.12b}$$
$$\omega_{\mathrm{p1}} + \omega_{\mathrm{p2}} = \omega_{\mathrm{s}} + \omega_{\mathrm{PC}} \tag{5.12c}$$
$$\omega_{\mathrm{p1}} + \omega_{\mathrm{p2}} = \omega_{\mathrm{MI}} + \omega_{\mathrm{BS}} \tag{5.12d}$$
$$\omega_{\mathrm{p2}} + \omega_{\mathrm{s}} = \omega_{\mathrm{p1}} + \omega_{\mathrm{BS}} \tag{5.12e}$$
$$\omega_{\mathrm{p1}} + \omega_{\mathrm{PC}} = \omega_{\mathrm{p2}} + \omega_{\mathrm{MI}}, \tag{5.12f}$$

where Eqs. (5.12a)–(5.12b) are intra-modal MI, Eqs. (5.12c)–(5.12d) are IM PC, and Eqs. (5.12e)–(5.12f) are IM BS. The nonlinear induced polarization for ω_{MI}, given as an example here, is found by inserting Eqs. (2.37) and (2.38) into Eq. (2.8) with

$$\mathbf{R}^{(3)}(t_1, t_2, t_3) = \chi^{(3)}_{xxxx}\delta(t_1)\delta(t_2)\delta(t_3), \tag{5.13}$$

where $\chi^{(3)}_{xxxx} \equiv \chi^{(3)}$ is defined as in Sec. 2.4. Assuming that the electric field is polarized in the x direction only, the result becomes

$$\begin{aligned}\mathbf{P}^{(3)}_{\mathrm{MI}}(\mathbf{r}) = \hat{\mathbf{x}}\frac{3}{4}\epsilon_0\chi^{(3)}\Bigg[&2\left(\frac{|F^{(01)}_{\mathrm{p1}}|^2}{{N^{(01)}_{\mathrm{p1}}}^2}|E^{(01)}_{\mathrm{p1}}|^2 + \frac{|F^{(11)}_{\mathrm{p2}}|^2}{{N^{(11)}_{\mathrm{p2}}}^2}|E^{(11)}_{\mathrm{p2}}|^2\right)E^{(01)}_{\mathrm{MI}}\mathrm{e}^{i\beta^{(01)}_{\mathrm{MI}}z}\\
&+\frac{{F^{(01)}_{\mathrm{p1}}}^2F^{(01)*}_{\mathrm{s}}}{{N^{(01)}_{\mathrm{p1}}}^2N^{(01)}_{\mathrm{s}}}{E^{(01)}_{\mathrm{p1}}}^2E^{(01)*}_{\mathrm{s}}\mathrm{e}^{i\left(2\beta^{(01)}_{\mathrm{p1}}-\beta^{(01)}_{\mathrm{s}}\right)z}\\
&+2\,\frac{F^{(01)}_{\mathrm{p1}}F^{(11)}_{\mathrm{p2}}F^{(11)*}_{\mathrm{BS}}}{N^{(01)}_{\mathrm{p1}}N^{(11)}_{\mathrm{p2}}N^{(11)}_{\mathrm{BS}}}E^{(01)}_{\mathrm{p1}}E^{(11)}_{\mathrm{p2}}E^{(11)*}_{\mathrm{BS}}\mathrm{e}^{i\left(\beta^{(01)}_{\mathrm{p1}}+\beta^{(11)}_{\mathrm{p2}}-\beta^{(11)}_{\mathrm{BS}}\right)z}\\
&+2\,\frac{F^{(01)}_{\mathrm{p1}}F^{(11)}_{\mathrm{PC}}F^{(11)*}_{\mathrm{p2}}}{N^{(01)}_{\mathrm{p1}}N^{(11)}_{\mathrm{PC}}N^{(11)}_{\mathrm{p2}}}E^{(01)}_{\mathrm{p1}}E^{(11)}_{\mathrm{PC}}E^{(11)*}_{\mathrm{p2}}\mathrm{e}^{i\left(\beta^{(01)}_{\mathrm{p1}}+\beta^{(11)}_{\mathrm{PC}}-\beta^{(11)}_{\mathrm{p2}}\right)z}\Bigg],\end{aligned} \tag{5.14}$$

where the implicit x, y, z dependencies was left out for clarity. Inserting this expression into (2.50) the equation for ω_{MI} is easily derived; following the same procedure for all components and assuming that the pumps have high enough power to be considered constant in amplitude,

the six-field equations are

$$\begin{aligned}\partial_z E_{\mathrm{MI}}^{(01)} =& \frac{i\omega_{\mathrm{MI}} n_2}{c}\Big[2f^{(01,01)}|E_{\mathrm{p1}}^{(01)}|^2 E_{\mathrm{MI}}^{(01)} + 2f^{(01,11)}|E_{\mathrm{p2}}^{(11)}|^2 E_{\mathrm{MI}}^{(01)} \\ &+ f^{(01,01)} {E_{\mathrm{p1}}^{(01)}}^2 E_{\mathrm{s}}^{(01)*} \mathrm{e}^{-i\Delta\beta_a z} \\ &+ 2f^{(01,11)}\left(E_{\mathrm{p1}}^{(01)} E_{\mathrm{p2}}^{(11)} E_{\mathrm{BS}}^{(11)*} \mathrm{e}^{-i\Delta\beta_d z} + E_{\mathrm{p1}}^{(01)} E_{\mathrm{PC}}^{(11)} E_{\mathrm{p2}}^{(11)*} \mathrm{e}^{-i\Delta\beta_f z}\right)\Big]\end{aligned} \tag{5.15}$$

$$\partial_z E_{\mathrm{p1}}^{(01)} = \frac{i\omega_{\mathrm{p1}} n_2}{c}\left(f^{(01,01)}|E_{\mathrm{p1}}^{(01)}|^2 E_{\mathrm{p1}}^{(01)} + 2f^{(01,11)}|E_{\mathrm{p2}}^{(11)}|^2 E_{\mathrm{p1}}^{(01)}\right) \tag{5.16}$$

$$\begin{aligned}\partial_z E_{\mathrm{s}}^{(01)} =& \frac{i\omega_{\mathrm{s}} n_2}{c}\Big[2f^{(01,01)}|E_{\mathrm{p1}}^{(01)}|^2 E_{\mathrm{s}}^{(01)} + 2f^{(01,11)}|E_{\mathrm{p2}}^{(11)}|^2 E_{\mathrm{s}}^{(01)} \\ &+ f^{(01,01)} {E_{\mathrm{p1}}^{(01)}}^2 E_{\mathrm{MI}}^{(01)*} \mathrm{e}^{-i\Delta\beta_a z} \\ &+ 2f^{(01,11)}\left(E_{\mathrm{p1}}^{(01)} E_{\mathrm{PC}}^{(11)*} E_{\mathrm{p2}}^{(11)} \mathrm{e}^{-i\Delta\beta_c z} + E_{\mathrm{p1}}^{(01)} E_{\mathrm{p2}}^{(11)*} E_{\mathrm{BS}}^{(11)} \mathrm{e}^{-i\Delta\beta_e z}\right)\Big]\end{aligned} \tag{5.17}$$

$$\begin{aligned}\partial_z E_{\mathrm{PC}}^{(11)} =& \frac{i\omega_{\mathrm{PC}} n_2}{c}\Big[2f^{(01,11)}|E_{\mathrm{p1}}^{(01)}|^2 E_{\mathrm{PC}}^{(11)} + 2f^{(11,11)}|E_{\mathrm{p2}}^{(11)}|^2 E_{\mathrm{PC}}^{(11)} \\ &+ f^{(11,11)} {E_{\mathrm{p2}}^{(11)}}^2 E_{\mathrm{BS}}^{(11)*} \mathrm{e}^{-i\Delta\beta_b z} \\ &+ 2f^{(01,11)}\left(E_{\mathrm{p1}}^{(01)} E_{\mathrm{s}}^{(01)*} E_{\mathrm{p2}}^{(11)} \mathrm{e}^{-i\Delta\beta_c z} + E_{\mathrm{MI}}^{(01)} E_{\mathrm{p1}}^{(01)*} E_{\mathrm{p2}}^{(11)} \mathrm{e}^{i\Delta\beta_f z}\right)\Big]\end{aligned} \tag{5.18}$$

$$\partial_z E_{\mathrm{p2}}^{(11)} = \frac{i\omega_{\mathrm{p2}} n_2}{c}\left(f^{(11,11)}|E_{\mathrm{p2}}^{(11)}|^2 E_{\mathrm{p2}}^{(11)} + 2f^{(01,11)}|E_{\mathrm{p1}}^{(01)}|^2 E_{\mathrm{p2}}^{(11)}\right) \tag{5.19}$$

$$\begin{aligned}\partial_z E_{\mathrm{BS}}^{(11)} =& \frac{i\omega_{\mathrm{BS}} n_2}{c}\Big[2f^{(01,11)}|E_{\mathrm{p1}}^{(01)}|^2 E_{\mathrm{BS}}^{(11)} + 2f^{(11,11)}|E_{\mathrm{p2}}^{(11)}|^2 E_{\mathrm{BS}}^{(11)} \\ &+ f^{(11,11)} {E_{\mathrm{p2}}^{(11)}}^2 E_{\mathrm{PC}}^{(11)*} \mathrm{e}^{-i\Delta\beta_b z} \\ &+ 2f^{(01,11)}\left(E_{\mathrm{MI}}^{(01)*} E_{\mathrm{p1}}^{(01)} E_{\mathrm{p2}}^{(11)} \mathrm{e}^{-i\Delta\beta_d z} + E_{\mathrm{p1}}^{(01)*} E_{\mathrm{s}}^{(01)} E_{\mathrm{p2}}^{(11)} \mathrm{e}^{i\Delta\beta_e z}\right)\Big],\end{aligned} \tag{5.20}$$

where the phase mismatch parameters correspond to the frequency conservation equations (5.12a)–(5.12f),

$$\Delta\beta_{\mathrm{i}} = \beta_{\mathrm{MI}}^{(01)} + \beta_{\mathrm{s}}^{(01)} - 2\beta_{\mathrm{p1}}^{(01)} \tag{5.21i}$$

$$\Delta\beta_{\mathrm{ii}} = \beta_{\mathrm{PC}}^{(11)} + \beta_{\mathrm{BS}}^{(11)} - 2\beta_{\mathrm{p2}}^{(11)} \tag{5.21ii}$$

$$\Delta\beta_{\mathrm{iii}} = \beta_{\mathrm{s}}^{(01)} + \beta_{\mathrm{PC}}^{(11)} - \beta_{\mathrm{p1}}^{(01)} - \beta_{\mathrm{p2}}^{(11)} \tag{5.21iii}$$

$$\Delta\beta_{\mathrm{iv}} = \beta_{\mathrm{MI}}^{(01)} + \beta_{\mathrm{BS}}^{(11)} - \beta_{\mathrm{p1}}^{(01)} - \beta_{\mathrm{p2}}^{(11)} \tag{5.21iv}$$

$$\Delta\beta_{\mathrm{v}} = \beta_{\mathrm{s}}^{(01)} + \beta_{\mathrm{p2}}^{(11)} - \beta_{\mathrm{p1}}^{(01)} - \beta_{\mathrm{BS}}^{(11)} \tag{5.21v}$$

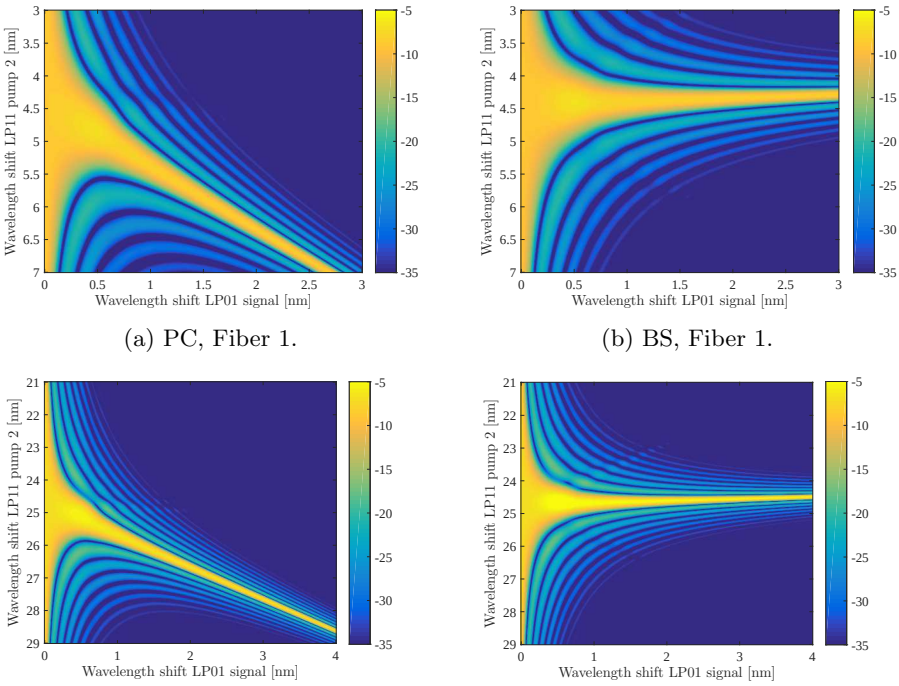

(a) PC, Fiber 1.

(b) BS, Fiber 1.

(c) PC, Fiber 2.

(d) BS, Fiber 2.

Fig. 5.5: Analytic results of six-field IM-FWM; the color scale show the CE of PC and BS in dB and is the same in all plots

$$\Delta\beta_{\mathrm{vi}} = \beta_{\mathrm{MI}}^{(01)} + \beta_{\mathrm{p2}}^{(11)} - \beta_{\mathrm{p1}}^{(01)} - \beta_{\mathrm{PC}}^{(11)}. \tag{5.21vi}$$

Approximate expressions for $\Delta\beta_{\mathrm{i-vi}}$ are calculated in the next section. Like in the previous chapters Eqs. (5.15)–(5.20) are solved using a 4th order Runge-Kutta algorithm with $n_2 = 2.6 \times 10^{-20}$ $(\mathrm{W\,m})^{-1}$, constant pump powers $P_{\mathrm{p1}} = P_{\mathrm{p1}} = 26.5$ dBm, a fiber length of $L = 1$ km in 200 steps, and $\lambda_0 = 1550$ nm in $\omega_0 = 2\pi c/\lambda_0$, where the nonlinear parameter $\Gamma_j = \omega_j n_2/c$ is simplified to be the same for all of $j \in \{\mathrm{MI}, \mathrm{p1}, \mathrm{s}, \mathrm{PC}, \mathrm{p2}, \mathrm{BS}\}$. The fiber parameters are taken from Tab. 5.1 and Fig. 5.2.

Figure 5.5 shows the CE vs. wavelength shift of the signal and pump 2 from pump 1 of PC and BS for both fibers from solving Eqs. (5.15)–(5.20). In the six-field theory, the CE is defined as

$$\mathrm{CE} = \frac{|E_{\mathrm{i}}(L)|^2}{|E_{\mathrm{s}}(L)|^2}, \tag{5.22}$$

i.e. the output idler relative to the output signal because this is how the CE is measured experimentally. The difference from the 4-field theory is

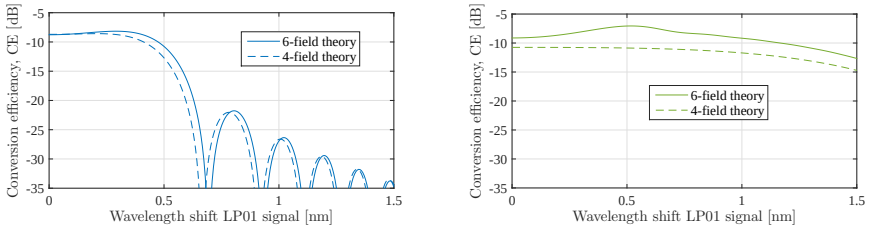

(a) PC (b) BS

Fig. 5.6: Comparison of six-field (solid) and four-field (dashed) theory in Fiber 1; (a) PC and (b) BS CE vs. signal wavelength shift for $\lambda_{p2} = 1553.5$ nm.

that more contours have appeared in the areas where multiple processes are phase matched. The difference between Fiber 1 and Fiber 2 is that Fiber 1 is phase matched at a 4.5 nm separation between pump 1 and pump 2 while Fiber 2 is phase matched at a separation of 25 nm; this is due to a larger RIGV between the modes in Fiber 2. Also, since the effective mode areas are smaller in Fiber 2, the CE is higher (lighter yellow).

To better appreciate the six-field theory, the CE of both the six-field and the four-field theory for PC and BS is plotted in Fig. 5.5(a) and (b), respectively, vs. signal wavelength shift from pump 1 for $\lambda_{p2} = 1553.5$ nm in Fiber 1. The six-field theory has more features than the simple 4-field, and as becomes clear in below these feature are important experimentally. In Fig. 5.5(a) and (b), BS shows the largest difference between the two descriptions but for other values of the pump 2 wavelength it is opposite. Note that in this specific plot, the CE of the six-field process is calculated as $|E_i(L)|^2/|E_s(0)|^2$ to better compare to the four-field theory.

5.1.3 Phase matching in two-mode fibers

The phase matching parameter, $\Delta\beta(\omega_n, \omega_m, \omega_k, \omega_l)$, is in all cases above calculated by expanding the wavenumber of each participating wave in a Taylor series around frequency ω_0,

$$\beta^{(\mu)}(\omega_n) = \beta_0^{(\mu)} + \beta_1^{(\mu)}(\omega_n - \omega_0) + \frac{\beta_2^{(\mu)}}{2!}(\omega_n - \omega_0)^2 + \frac{\beta_3^{(\mu)}}{3!}(\omega_n - \omega_0)^3 + \dots \tag{5.23}$$

where $\beta_i^{(\mu)}(\omega_0)$ as the i'th order expansion coefficient in the Taylor expansion of the wavenumbers for mode μ evaluated at frequency ω_0. The

terms with $i = 0$ cancel from $\Delta\beta$, the terms with $i = 1$ are the inverse group velocity, and the terms with $i = 2$ represent the chromatic dispersion of mode LPμ through $D^{(\mu)} = -(2\pi c/\lambda_0^2)\beta_2^{(\mu)}$. If it is assumed that pump 1 and signal s are in the LP01 mode and pump 2 and idler i are in the LP11 mode, the phase mismatch (as also calculated in Ref. [127]) for the IM FWM processes of PC and BS becomes

$$\Delta\beta = \left[\beta_1^{(01)} + \beta_2^{(01)}\left(\frac{\Delta\omega_\mathrm{s} + \Delta\omega_\mathrm{p1}}{2}\right) - \beta_1^{(11)} - \beta_2^{(11)}\left(\frac{\Delta\omega_\mathrm{p2} + \Delta\omega_\mathrm{i}}{2}\right)\right](\omega_\mathrm{s} - \omega_\mathrm{p}), \tag{5.24}$$

where the wave numbers were expanded to second order and $\Delta\omega_j = \omega_j - \omega_0$ for $j \in \{\mathrm{p1}, \mathrm{p2}, \mathrm{s}, \mathrm{i}\}$. The important point to take from the phase mismatch is that it vanishes when the inverse group velocities of each mode evaluated at the average wavelength of the waves in the same mode are equal. Figure 5.7 illustrated this point for PC: the inverse group velocity at the average wavelength of pump 1 and the signal s in mode LP01, $\lambda_\mathrm{a}^{(01)}$, has to lie on the same horizontal line as the inverse group velocity of the average wavelength of the idler i and pump 2, $\lambda_\mathrm{a}^{(11)}$, to achieve phase matching. Figure 5.8 shows the same for BS where it should be noted that phase matching is conserved perfectly when tuning the signal wavelength if the two RIGV lines are parallel (same dispersion) and without curvature (negligible dispersion slope); this property is due to energy conservation, which makes the idler change wavelength along with the signal such that also the wavelength averages in each mode moves together. In Fig. 5.7 the same property does not apply; the signal and idler moves in opposite directions so only at one signal wavelength is phase matching fulfilled.

Finally, note in Eq. (5.24) that the last factor also makes the phase mismatch become small when the signal and pump p have similar frequencies, which follows trivially from the consideration that when two photons are annihilated, the two new photons are generated in the same modes at the same wavelengths.

The phase mismatch for the intra-modal FWM processes of Eqs. (5.21i) and (5.21ii) are calculated in the same way as is done in the single-mode case of Ref. [17], only in these cases the wave components are not near the zero-dispersion wavelength of the fiber. For the processes considered here, the phase mismatch of mode μ becomes

$$\Delta\beta^{(\mu)} = \beta_2^{(\mu)}(\omega_\mathrm{s} - \omega_j)^2 + \beta_3^{(\mu)}(\omega_\mathrm{s} - \omega_j)^2(\omega_j - \omega_0), \tag{5.25}$$

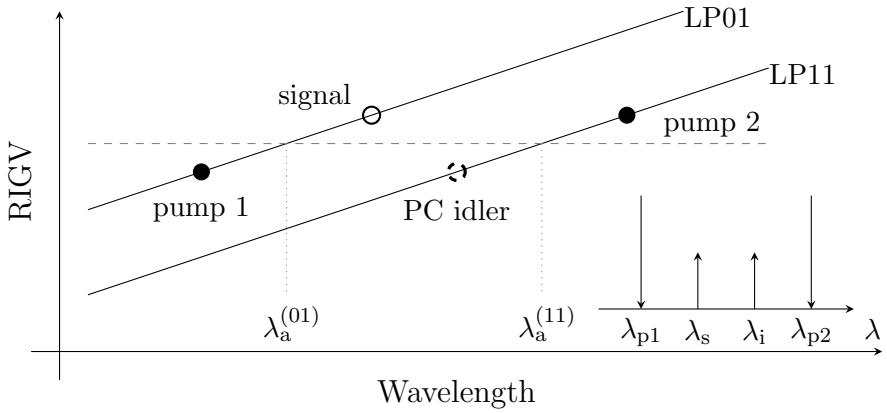

Fig. 5.7: Sketch of the condition for phase matching for PC: the inverse group velocity of the average wavlength in the LP01-mode, $\lambda_a^{(01)}$, has to be equal to the inverse group velocity of the average wavlength in the LP11-mode, $\lambda_a^{(11)}$. The inset shows the wavelength configuration of PC.

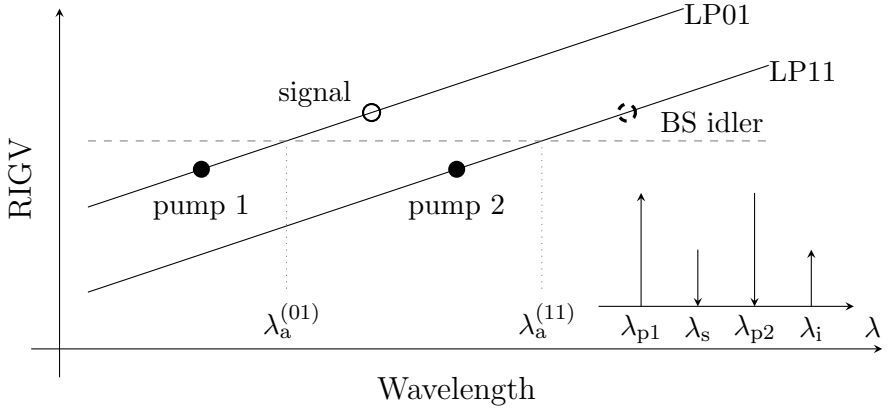

Fig. 5.8: Sketch of the condition for phase matching for BS: the inverse group velocity of the average wavlength in the LP01-mode, $\lambda_a^{(01)}$, has to be equal to the inverse group velocity of the average wavlength in the LP11-mode, $\lambda_a^{(11)}$. The inset shows the wavelength configuration of BS.

where $\omega_j = \omega_{p1}$ for μ being LP01 and $\omega_j = \omega_{p2}$ for μ being LP11, and the wave number expansion coefficients are related to the wavelength domain parameters as show in Ch. 2 in Eqs. (2.32) and (2.33).

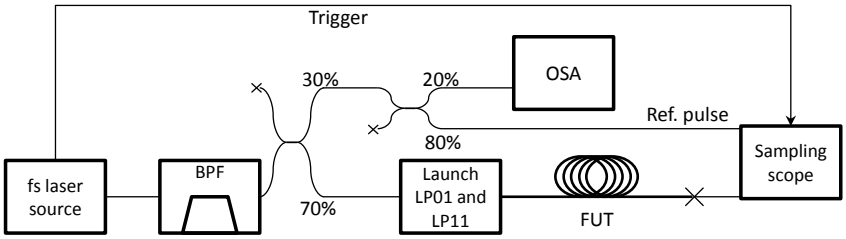

Fig. 5.9: Sketch of the time-of-flight measurement setup. BPF, band-pass filter; OSA, optical spectrum analyzer; FUT, fiber under test.

5.2 Experimental setups

Two setups are used to perform IM-FWM: the first does a time-of-flight (ToF) measurement two find the inverse group velocity vs. wavelength for both modes from which the phase matching properties of interest are extracted; the second does the actual FWM experiment with multiplexing and demultiplexing of the two modes.

5.2.1 Time-of-flight measurement

A sketch of ToF setup is shown in Fig. 5.9: a fs laser is used as source and from it a pulse trigger is sent directly to the sampling scope to the far right; the fs laser source has a broad spectrum, ~ 15 nm, so a tunable band-pass filter (BPF) cut up each fs pulse in smaller spectral fragments of approx 1 nm; the 30/70 fiber coupler divides the output of the BPF into a monitoring arm that goes to both an OSA and the sampling scope as a reference pulse and towards the fiber under test (FUT); the launching of the LP01 and LP11 modes is shown schematically in a box but in the actual experiment the simultaneous launching of both modes was generated by misaligning the incoming single-mode fiber (SMF) a slightly from the FUT; the FUT is one of the fibers mentioned above, Fiber 1 and Fiber 2, in turn; the small cross denotes a rough, slightly misaligned splicing that allows light from both modes of the FUT to propagate into the SMF that is connected to the sampling scope.

The output of the sampling scope of a single setting of the BPF (one wavelength) is seen in Fig. 5.10. The light pulses of the LP01 and LP11 modes of the fiber, which were perfectly overlapping at input, are approximately 100 ps apart at the output. The reference pulse is outside the time interval shown here but it is needed to capture the movement of both pulses in time. The exact position on the time axis of each pulse

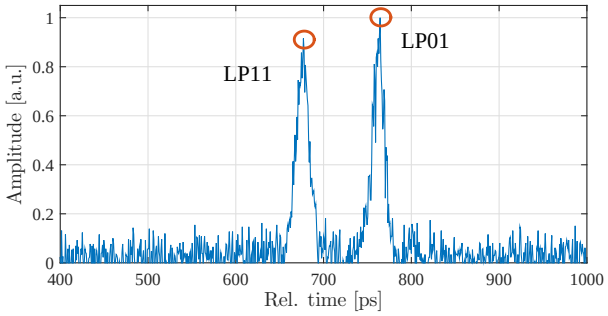

Fig. 5.10: Time trace from the sampling scope in Fig. 5.9. The time lag between the two pulses represent the diffrence in group velocity between the LP01 and LP11 modes.

is calculated by a weighted average over the entire pulse.

This procedure is carried out for a number of wavelengths on both fibers, and the RIGV (time separation between the pulses of the FUT and the reference pulse divided by fiber length) is plotted in Fig. 5.11 for (a) Fiber 1 and (b) Fiber 2. In both plots, the pulses in the LP01 and LP11 modes are shown with red squares and blue dots, respectively. The difference between the to curves is shown with gray stars. Second order polynomial fits are applied to the data from which the slope is identified as the absolute dispersion and the curvature the dispersion slope. The wavelength interval that was accessible using the fs laser source was too small to capture an accurate value of the dispersion slope. As shown in the plots, the measured dispersion values were $D^{(01)} = 18.7$ ps/(nm km) and $D^{(11)} = 21.3$ ps/(nm km) for Fiber 1 and $D^{(01)} = 18.5$ ps/(nm km) and $D^{(11)} = 18.0$ ps/(nm km) Fiber 2; these values are in reasonable agreement with the simulated values provided by the fiber supplier shown in Tab. 5.1 but generally the measured dispersion values are smaller. It turns out that the simulated values of the dispersion of both modes fit better with the experimental data below than the measured values; that is the reason that the simulations in the previous sections were done with the simulated dispersion values.

The vertical separation between the LP01 and LP11 mode curves (the RIGV) is found to be 96 ps/km for Fiber 1 and 500 ps/km for Fiber 2. The corresponding simulated values from the fiber supplier were 60 ps/km and 467 ps/km, respectively, which are significantly different. The experimental data shows great deviance from the simulated RIGV but a much better agreement with the measured RIGV. Therefore, the simulations done in the previous sections were done with the measured RIGV.

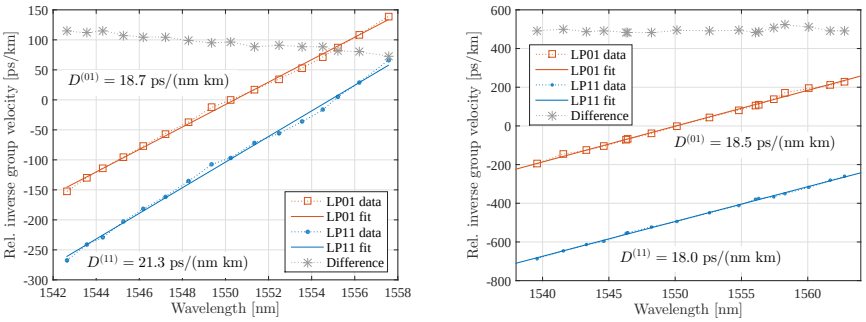

(a) Fiber 1 (b) Fiber 2

Fig. 5.11: RIGV vs. wavelength for (a) Fiber 1 and (b) Fiber 2 of both the LP01 mode (red squares) and the LP11 mode (blue dots); the difference between the two cuves is marked by gray stars.

The horizontal separation of the RIGV curves determines the wavelength separation between the two pumps, cf. Figs. 5.7 and 5.8. The measurements in Fig. 5.11 shows a 4.4 nm separation between the LP01 and LP11 modes at 1550 nm for Fiber 1 and a 25 nm separation for Fiber 2. These values are important for the choice of pump wavelength values in the experimental section below.

5.2.2 Two-mode four-wave mixing

The experimental setup for measuring and characterizing IM FWM is shown in Fig. 5.12; the nonlinear medium is one of the two aforementioned two-mode fibers, Fiber 1 and Fiber 2, in turn. Three tunable laser sources are used to generate the inputs, i.e. pump 1 (TLS 2), pump 2 (TLS 1), and signal s (TLS 3), and a 95/5 coupler is used to achieve a 22 dB power difference between pump 1 and s. All inputs are time gated with a 10% duty cycle and a repetition rate of 10 MHz to avoid stimulated Brillouin scattering and to increase the peak powers (this time gating results in 10 ns pulses separated by 100 ns). Two polarization controllers are used to co-polarize the waves in the LP01 and LP11 optical paths, respectively, which is ensured by the polarization beam-splitter (PBS) after beam combination in the 50/50 non-polarization beam-splitter. Erbium-doped fiber amplifiers (EDFAs) amplify the inputs to achieve pump average powers after the fiber of 20.5 dBm in both pumps; the loss of the fiber was verified to be ∼0.2 dB/km in both modes.

Pump 1 and signal s are launched in the LP01 mode while the second pump 2 is launched into the LP11 mode using a mode-multiplexer

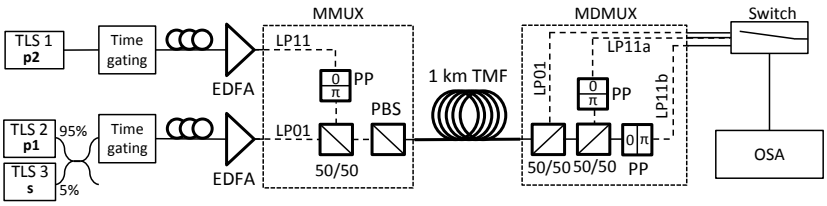

Fig. 5.12: Sketch of the experimental setup; thin solid line, single-mode fiber; thick solid line, TFM; dashed lines, free space; TLS, tunable laser source; MMUX, mode-multiplexer; EDFA, Erbium-doped fiber amplifier; 50/50, 3-dB non-polarization beam-splitter; PBS, polarization beam-splitter; PP, phase plate; TMF, two-mode fiber; MDMUX, mode-demultiplexer; OSA, optical spectrum analyzer.

(MMUX) based on a phase plate (PP), which shifts the phase of half the beam front in the transverse plane by π. The launching purity of the LP11 mode was tested by wrapping the end of the TMF around a cylinder with a diameter of ~ 2 cm, which attenuates the LP11 mode but not the LP01 mode, and a change in power in the LP11 mode of -28 dB was measured directly at the output of the TMF; by only launching the LP01, a change in power of < 0.2 dB was measured by wrapping the TMF. At the output of the fiber, it was also verified that the LP01 and LP11 pulses had optimal temporal overlap.

The modal content of the output of the TMF is analyzed in a mode-demultiplexer (MDMUX) by separating the beam into three using two 3-dB beam splitters as shown in Fig. 5.12. The first beam measures the the power in the LP01 mode of the TMF by coupling directly into a single-mode fiber that does not allow the content of the LP11 mode in the TMF to propagate. The other two beams are used in combination to measure the power in the LP11 mode: one PP is placed in each beam path in order to phase shift the wave of the LP11 mode back to a constant phase front and simultaneously avoid collection of light from the LP01 mode; using one PP only is not sufficient since the orientation of the LP11 mode at the output of the TMF is impractical to control. The two PPs are hence orthogonally orientated, effectively projecting the LP11 mode onto two orthogonal transverse directions, which are collected in the two LP11 ports, respectively. The sum of the powers measured in the two LP11 ports is thus independent on the LP11 mode orientation. Lastly, an optical switch is used for quick sampling of all three ports on the optical spectrum analyzer (OSA).

The mode-separation performance of the MDMUX was investigated and Fig. 5.13 shows the LP01 port (left) and the sum of the two LP11 ports (right) for a typical measurement where the wavelenghts of the

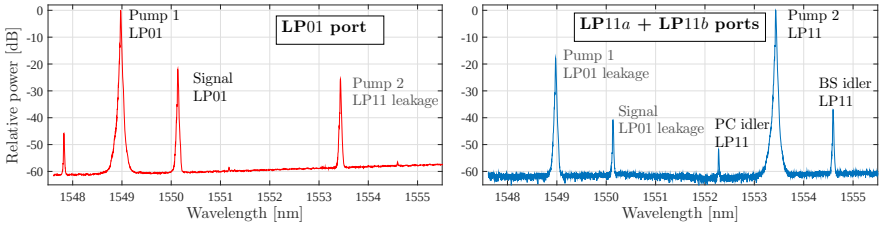

Fig. 5.13: Performance of the MDMUX after Fiber 1; the LP01 port (left) extinguishes the LP11 mode by 25 dB, and the LP11 port (right) extinguishes the LP01 mode by 18 dB.

input LP01 pump 1 and signal s and LP11 pump 2 were $\lambda_{\mathrm{p1}}^{(01)} = 1549$ nm, $\lambda_{\mathrm{s}}^{(01)} = 1550.15$ nm, and $\lambda_{\mathrm{p2}}^{(11)} = 1553.45$ nm, respectively: the data is normalized to the LP01 and LP11 pump powers in each graph, respectively. The LP01 port extinguishes the LP11 mode by 25 dB while the LP11 port extinguishes the LP01 mode by 18 dB.

5.3 Results: conversion efficiency of two two-mode fibers

The final purpose of this chapter is to measure the phase matching bandwidth of PC and BS and compare to the theoretical predictions of the six field theory. To do so, the setup in Fig. 5.12 is used and spectra like the ones in Fig. 5.13 are recorded on the OSA for a range of signal s wavelengths and the processes is repeated for a number of pump 2 wavelengths. These sets of data is then compared to the corresponding simulated values along horizontal lines in Fig. 5.5.

5.3.1 Fiber 1: small differential group delay

In this section, Fiber 1, which has the smallest RIGV of the two fibers that leads to a wavelength separation of 4.4 nm, is discussed. The pump p2 wavelength values are hence chosen in a series of values around a separation of 4.4 nm from the pump 1 wavelength as shown in Tab. 5.2; the pump1 wavelength is $\lambda_{\mathrm{p1}} = 1549$ nm is all cases (a)–(f).

To find the experimental value of the CE of PC for Fiber 1, the power of the LP01 signal is read off of the LP01 port as shown in Fig. 5.13(a) and subtracted (in logarithmic units) from the value of the LP11 PC idler, which is read off of the LP11a+LP11b ports. This procedure work because the pumps have the same output power of the FUT. In Fig. 5.14, the measured CE vs. signal wavelength shift from pump 1 is plotted for

	λ_{p2} [nm]	λ_{p2} - λ_{p1} [nm]		λ_{p2} [nm]	λ_{p2} - λ_{p1} [nm]
(a)	1553.00	4.00	(d)	1553.75	4.75
(b)	1553.40	4.40	(e)	1554.50	5.50
(c)	1553.5	4.50	(f)	1554.70	5.70

Table 5.2: Pump p2 wavelengths used in experiments for Fiber 1; pump p1 is $\lambda_p = 1549$ nm in all cases.

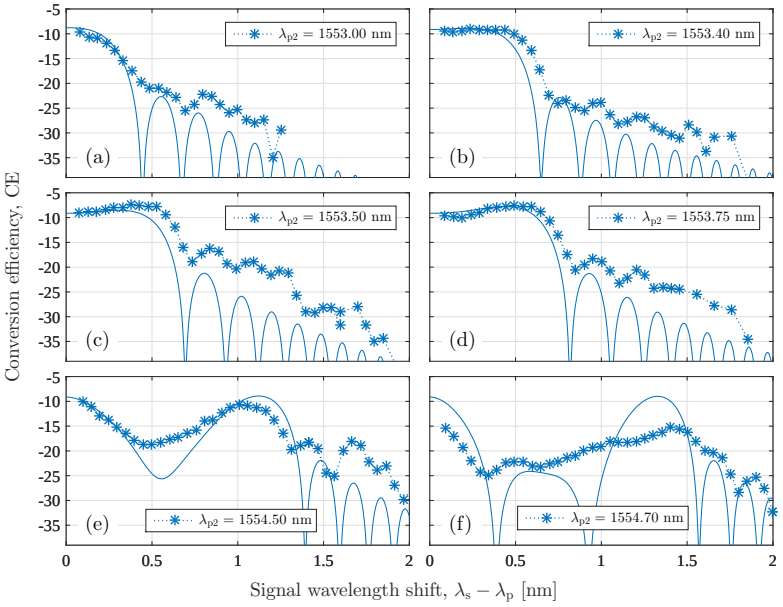

Fig. 5.14: Measured CE for PC vs. signal wavelength for cases (a)–(f) of pump q wavelengths corresponding to the values given in Tab. 5.2.

all choices of pump 2 wavelengths, i.e. cases (a)–(f), together with the corresponding simulated curve from Fig. 5.5 of the six-field theory. As explained above, the CE of PC has different characteristics (vs. signal wavelength) for values below and above $\lambda_q \approx 1553.5$ nm; below, the CE has only one peak and the width of that peak increases with λ_{p2}; above, the CE has two peaks and the peaks separate more in wavelength with increasing λ_{p2}.

The experimental results in Fig. 5.14 replicate these characteristics well. In cases (a)–(d), the width of the CE peak is increasing from 0.25 nm to 0.75 nm in accordance theory. In case (d), it is observed that the single peak of phase matching is starting to split up in two peaks. In the two remaining cases of (e) and (f), two clearly separated peaks are

observed; the peak close to $\lambda_s - \lambda_p = 0$ is present due to PC being phase matched because the $(\omega_s - \omega_p)$-term in Eq. (5.24) is small; the other peak is present due to the first term in square brackets in Eq. (5.24) is small. It should be noted when comparing the experimental data to the theoretical curves that the pump powers in the simulations were adjusted to 26.5 dBm even though the output pump average power was measured to be 20.5 dBm in both modes; with a 10% duty cycle, the peak power of the pump pulses is expected to be 30.5 dBm. There are two reasons that this adjustment is justifiable: 1) the theory assumes that all propagating fields are co-polarized through the whole fiber, but any drift in polarization reduces the strength of the IM FWM in the experimental data; 2) the pump output peak power of 30.5 dBm is only valid of the pulses are perfectly square, but in reality the pulses are not shaped perfectly square by the amplitude modulators so the peak power is likely to be smaller than 30.5 dBm. Hence, a good agreement between experimental and simulated CE is obtained if pump powers of 26.5 dBm are used.

The highest CE is found experimentally in case (c) where -7.4 dB is achieved at $\lambda_s - \lambda_p \approx 0.4$ nm. However, the CE is evaluated as the output idler power relative to the output signal power and not the input signal power, which is not possible to evaluate in the experimental setup at this time. A problem arises because the signal is amplified through the fiber through intra-modal degenerate FWM by pump 1; hence the generated component below $\lambda = 1548$ nm in Fig. 5.13. Therefore, we compare the output idler to a too large value when evaluating the CE, and it is thus concluded that the measured CE is > -7.4 dB.

The CE of BS is evaluated in the same way as for PC in the same set of measurements, only reading off the power of the LP11 BS idler of Fig. 5.13 instead of the LP11 PC idler; the results are shown in Fig. 5.15 in the same manner as the PC results in Fig. 5.14. As already explained, the phase matching characteristics of BS is different from PC: only in a narrow interval of pump p2 wavelengths close to $\lambda_q \approx 1553.5$ nm is any phase matching bandwidth in terms of signal wavelengths expected. On the other hand, this bandwidth is predicted to be significantly larger than any bandwidth observable in PC.

Indeed, the measured CE for cases (a)–(f) confirm these predictions in decent agreement with theory. Case (a), pump 2 wavelength being below ~ 1553.5 nm, has a narrow bandwidth compared to cases (b) and (c), which have pump 2 wavelengths inside the region of a wide bandwidth of phase matching, as seen in Fig. 5.5(b). The maxima around $\lambda_s - \lambda_p = 0.5$ nm in (b) and (c) are predicted by the six-field theory (but not the four-field theory) and is a result of a combination

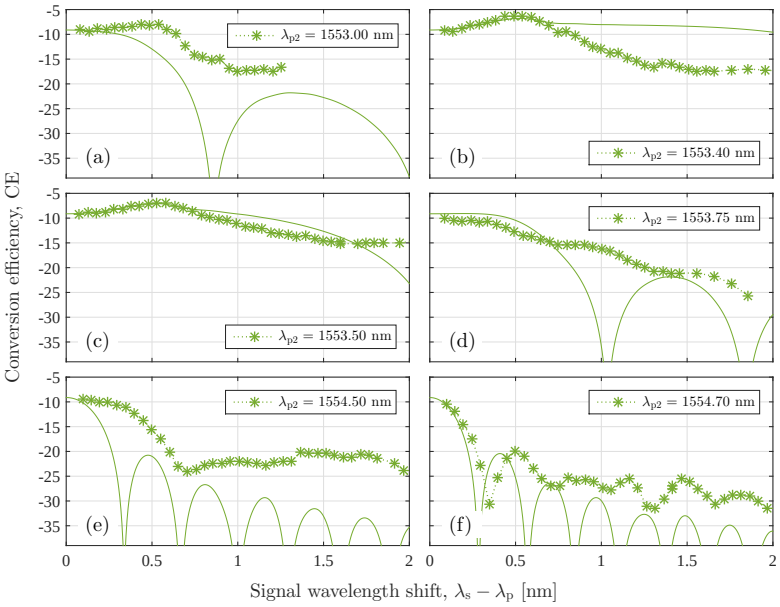

Fig. 5.15: Measured CE for BS vs. signal wavelength for cases (a)–(f) of pump q wavelengths corresponding to the values given in Tab. 5.2.

of phase matched PC, BS, and MI. The CE bandwidths of (b) and (c) are the widest observed in Fiber 1 in good qualitative agreement with theory, and clearly wider than any bandwidth observed for PC. The pump 2 wavelengths of case (d) lies on the upper edge of the region of a wide bandwidth of phase matching, and indeed the bandwidth of the CE diminishes. Cases (e) and (f) are above the region of phase matching so the bandwidth of the CE becomes gradually smaller.

The largest CE of > -6.3 dB is found in case (b) where evidently the same problem with evaluating the CE based on the input signal power, as explained for PC above, is the reasons for the $>$-sign.

5.3.2 Fiber 2: large differential group delay

Attention is now turned to Fiber 2, which has a larger RIGV that leads to a wavelength separation of 25 nm; the purpose of this section is to investigate if the performance of the IM-FWM processes PC and BS are qualitatively the same as for Fiber 1 when the wavelengths separation is larger. Since one of the potential applications of higher order modes in fibers is enabling FWM among a broad spectrum of wavelengths, it is important that the efficiency of IM-FWM is not degraded at large wavelengths separations due to for example dispersion fluctuations. The

	λ_{p2} [nm]	λ_{p2} - λ_{p1} [nm]		λ_{p2} [nm]	λ_{p2} - λ_{p1} [nm]
(a)	1559.3	22.9	(d)	1563.0	25.6
(b)	1562.2	24.8	(e)	1564.3	26.9
(c)	1562.4	25.0	(f)	1565.3	27.9

Table 5.3: Pump p2 wavelengths used in experiments for Fiber 2; pump p1 is $\lambda_p = 1537.4$ nm in all cases.

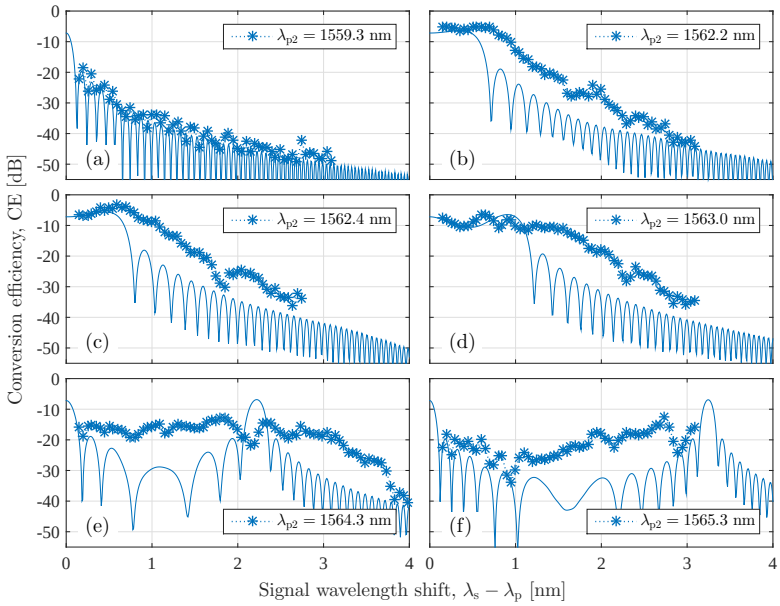

Fig. 5.16: Measured CE for PC vs. signal wavelength for cases (a)–(f) of pump q wavelengths corresponding to the values given in Tab. 5.3.

pump 1 wavelength was changed to 1537.4 nm (since both pumps should preferably lie inside the amplification spectrum of an EDFA), and the pump 2 wavelengths chosen of measurements are shown in Tab. 5.3.

Figure 5.16 shows the measured CE vs. signal wavelength shift in the same fashion as Fig. 5.14. For all cases (a)–(f), the measurements follow the general trends predicted by the theory but quantitatively the agreement it not as good as for Fiber 1. In (b)–(d), the measured peak is wider than expected, which are likely not explained by simultaneous IM FWM since the six strongest (phase matched and non-cascaded) processes are included in the theory. The explanation is most likely that neither the ToF measurements nor the simulated dispersion data from the fiber supplier has given a sufficient insight into the dispersion prop-

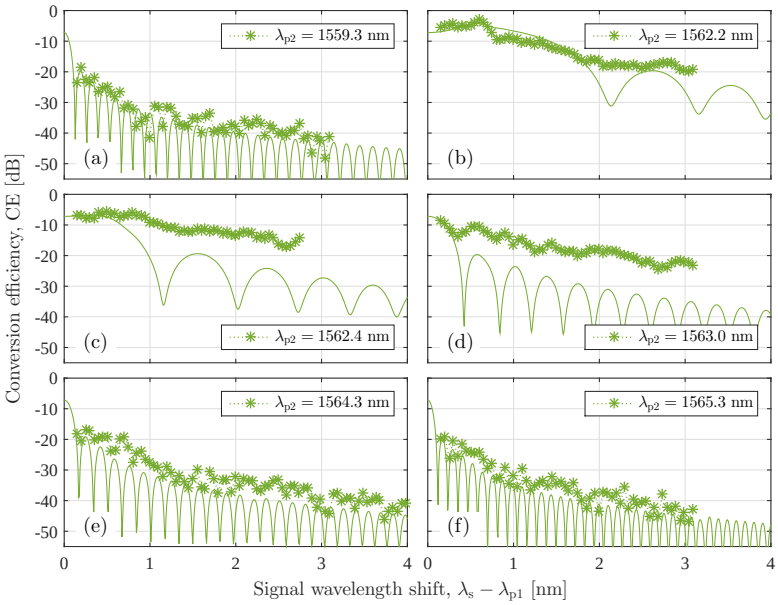

Fig. 5.17: Measured CE for BS vs. signal wavelength for cases (a)–(f) of pump q wavelengths corresponding to the values given in Tab. 5.3.

erties of the fiber, so the theory is not calculating the phase matching spectra accurately .

The experimental data of cases (e) and (f) also show some deviance from theory which are most likely due to dispersion fluctuations. Clearly, any fluctuations due to fabrication imperfections in the dispersion parameters such as inverse group velocity, dispersion coefficient, or dispersion slope through the fiber leads to critical changes in the phase matching condition of IM FWM. Thus, one must expect that any experimental investigation that tries to map out the CE in Fig. 5.5 will find a more blurred picture with broader and lower amplitude features.

The results for the CE of BS as shown in Fig. 5.17 confirm the trends observed for PC. Firstly, a good quantitative agreement between experiments and theory is found; a wide conversion bandwidth is measured in (b) and (c) as theory predicts, and in the rest of the cases he conversion bandwidth is much smaller. However, (c) and (d) show the same wider bandwidth experimentally than theoretically, which confirms the hypothesis that the theoretical curves are inaccurate.

The largest CE measured in Fiber 2 is CE > -3.25 dB for PC in case (c) and CE > -2.70 dB for BS in case (b), where the $>$-signs are there for the same reason as explained for Fiber 1. These CE values are higher than those reported for Fiber 1 due to the smaller effective modal

areas of Fiber 2 as seen in Tab. 5.1. Also, stimulated Raman scattering was not included in the theory, and pump 2 and the idler are situated at a 25 nm higher wavelength than pump 1 so a small amount of Raman amplification is expected; this might explain why the results of Fiber 2 are generally above the theoretical curves.

5.4 Partial conclusion

In this chapter, inter-modal four-wave mixing was discussed theoretically and experimentally. Two models of inter-modal four-wave mixing, a simple four-field model and a more comprehensive six-field model, were derived and the their differences were highlighted. The phase matching properties of two-mode fibers fiber were analyzed in detail and both mathematical and conceptual conditions for efficient phase matching were discussed. The models were used to predict the conversion efficiency from signal to idler in two separate four-wave mixing processes, phase conjugation and Bragg scattering, in two fibers with different phase matching properties. The dispersion properties of the two fibers were such that the signal is converted to the idler over 4.4 nm in Fiber 1 over 25 nm in Fiber 2.

Secondly, inter-modal four wave mixing experiments were carried out in the two fibers 1 and 2. The conversion efficiency of both phase conjugation and Bragg scattering was measured in both fibers and compared to the theoretical predictions of the six-field theory; it was found by comparing the two models that the four-field theory did not describe important features observed experimentally. A good qualitative accordance between experiments and theory was observed for both processes in both fibers though a detailed quantitative agreement was only observed for some cases of pump 2 wavelength values in Fiber 1. The most important reason for the deviance of the results in Fiber 2 is believed to be dispersion fluctuations along the fiber and Raman amplification from the pump with the smallest wavelength.

Chapter 6

Conclusion and outlook

This final chapter concludes all the former chapters of the thesis and suggests in an outlook ideas on how to continue the work that was carried out.

6.1 Conclusion

Starting at Maxwell's equations, this thesis provided a thorough introduction to electromagnetic theory in the context of fiber waveguides. Transverse equations were derived for both full-vectorial and linearly polarized modes, and a general propagation equation was determined from which all other propagation equations in the thesis were derived.

In Ch. 3, a semi-classical model of quantum noise in fiber parametric processes that accounts for the impacts of Raman scattering, fiber loss, dispersion, and the depleted pump regime was presented. No existing quantum models account, to the knowledge of the author, for all these effects simultaneously. The semi-classical model was validated against simple results of quantum models and excellent agreement was found. A phase-insensitive parametric amplifier in shape of modulation interaction was modeled and it was demonstrated that loss plays only a minor role for the noise properties phase insensitive parametric amplifiers. An asymmetric Raman-induced noise figure spectrum was found and it was explained why the spectrum is reverse asymmetric compared to what might be expected from the asymmetry of spontaneous Raman scattering. One of the most interesting results of this chapter was that spontaneous Raman scattering induced an increased noise figure close to the degenerate pump, a results not predicted by quantum models; an argument was given in favor of the existence of such an increase. In the depleted pump regime, the semi-classical model predicts amplitude

regeneration of the amplified signal even in the presence of Raman scattering; it was noted that such amplitude regeneration has already been measured.

For parametric frequency conversion in form of Bragg scattering, it was shown that loss induces a noise figure floor that can only be avoided by converting in a shorter piece of fiber such that the accumulated loss is smaller. Raman scattering was found to induce a noise figure comparable with the 3 dB noise figure of parametric amplification, thus destroying the favorable noise less frequency conversion property of Bragg scattering. It was also shown that on the anti-stokes side of the pumps, the noise figure depends more on the pumps-to-side bands wavelength separation and the temperature than on the Stokes side.

Ch. 4 discussed two challenges associated with few-mode Raman fiber amplifiers: weak random linear mode coupling and mode-dependent gain. Equations for multi-mode Raman fiber amplification were derived, conditions for equal modal gain were calculated, and a model for weak random linear mode coupling was defined. These models were used to simulate the excess noise induced by random mode coupling in the pump of two-mode distributed Raman fiber amplifiers. It was shown that in the weak coupling regime intra-mode-group mode coupling has no observable effect on the mode-dependent gain and that inter-mode-group mode coupling has only a minor effect of < 0.3 dB in a case where distributed Raman amplification compensated for 20 dB of loss. The noise figure was simulated under variation of the signal input power and the degree of inter-mode-group mode coupling and for both signal modes three separate regimes were found in the space of these two parameters; the three regimes represent no induced noise figure, amplitude regeneration as for the parametric amplifier, and a large mode coupling induced noise figure, respectively.

Mode-dependent gain was also investigated experimentally in a two-mode Raman fiber amplifier. A scheme for measuring the Raman intensity overlaps in the fiber and using these for calculating the pump power distribution among the guided modes to achieve equal modal gain in the signal was presented. Using this scheme a mode-dependent gain of only 0.25 dB per 10 dB gain was demonstrated by launching the backward propagating pump into a specific combination of modes (17% in the LP01-mode and 83% in the LP11-mode).

In Ch. 5, inter-modal four-wave mixing was modeled and experimentally investigated. The goal was to find the conversion efficiency from signal to idler and the phase matching properties of two four-wave mixing processes, phase conjugation and Bragg scattering, including the bandwidth of phase matching for the signal. Two two-mode fibers with

different dispersion properties were investigated; the most significant difference between the fibers was the relative inverse group velocity of the two guided modes, which lead to the idler being generated in the LP11-mode with a wavelength separation of 4.4 nm from the signal in the LP01-mode in Fiber 1, and the idler being generated with a wavelength separation of 25 nm from the signal in Fiber 2 in the same mode configuration. For both fibers, the conversion efficiency of phase conjugation and Bragg scattering was measured for a range of signal wavelengths and pump-to-pump wavelength separations, and the highest conversion efficiencies found were > -7.4 dB for phase conjugation and > -6.3 dB for Bragg scattering in Fiber 1 and > -3.25 dB for phase conjugation and > -2.70 dB for Bragg scattering in Fiber 2. The simulated bandwidths of phase matching for the signal showed a good qualitative agreement with the experimental data; good quantitative agreement is believed to be limited by insufficient dispersion data, dispersion fluctuations through the fibers and Raman amplification from the pump with the smallest wavelength.

6.2 Outlook

The work carried out in this thesis is far from complete and there are more than a few ways to proceed at this point. In this final section, some comments on further work is given.

For the semi-classical modeling presented in Ch. 3, one obvious step forward is developing quantum models that describe all the regimes that the were presented in this thesis. However, until such models are developed, experimental verification of the semi-classical model is needed to confirm its validity; especially the noise properties of Bragg scattering have not been studied much so noise figure measurements for that particular process has value. Concerning modeling, the semi-classical model would find more use if it was defined for pulses instead of only CW. It remains, however, unclear how to define field ensembles for a continuum of frequencies. The most interesting angle, in the view of the author, is investigating the increasing Raman induced noise figure close to the degenerate pump in the phase-insensitive amplifier. Existing quantum models do not predict an increase in the noise figure around the pump so an interesting question is: is the semi-classical model not able to predict the noise figure of the combined effects of four-wave mixing and Raman scattering correctly, even though it predicts them correctly separately, or are the existing quantum models incomplete?

In Ch. 4, the model of weak random linear mode describes effects

that have not been given much attention in the literature so far. Therefore, the most important thing to do in a next step is to validate the model against other models or preferably experimental data. While it is difficult to prove that random linear mode coupling has a small impact on the mode-dependent gain as predicted in Ch. 4, it would be more feasible to experimentally verify the existence of the three regimes of the noise figure in the space of signal input power and degree of inter-mode-group mode coupling. However, since the degree of mode coupling is not a variable this investigation may be cumbersome. In terms of modeling, the model would be improved much if it was to be defined for a backward propagating pump. This, however, is problematic because one would have to guess the output photon number distribution of the pump (at signal input) to ensure both that the pump has a Poisson distributed number of photons at input (signal output) and that the signal has the measured distribution at the output.

The experimental investigation of equal modal gain in a two-mode Raman fiber amplifier of Ch. 4 has a more exciting potential. As a first thing, a better measurement of the output modal content is needed. This may be done by properly de-multiplexing the signal modes at the fiber output with phase plates as it is done in Ch 5. This improvement would remove the oscillations observed in the mode-dependent gain, and a better value for Raman intensity overlaps will most likely be achieved. Thus, an even lower mode-dependent gain should be achievable. The next step is to send actual data through a long two-mode fiber instead of a continuous wave signal, and then demonstrate that a better transmission can be achieved with a backward propagating pump in the correct combination of two modes to give equal modal gain.

In Ch. 5, the performance of the inter-modal four-wave mixing can be improved significantly by performing the same experiments in a shorter fiber with higher power (such that the same accumulated nonlinearity is achieved). A shorter fiber has multiple advantages: lower linear mode coupling, less polarization drift, and (presumably) a smaller degree of dispersion fluctuations. All of these effects, though to a small degree the mode coupling, are limiting the results presented in Ch. 5 at the moment. The next exciting step is do inter-modal four-wave mixing in fibers that have even larger separations in wavelength between the inverse group velocity curves; one goal that is worth pursuing is realizing four-wave mixing where the side bands are separated more than 20 THz from the pump(s) such that all Raman noise is avoided. Such a configuration could unlock the noise-less frequency conversion property of Bragg scattering in silica fibers.

Appendix A

Supplementary material for chapters

A.1 Statistical derivation of the noise figure of a Raman amplifier

Given an ensemble of electromagnetic fields defined as Eq. (3.17), we may apply a constant Raman gain G in power to one signal provided by one pump, which leaves the SNR unchanged (signal and noise are amplified equally), but spontaneous emission from the pump is also present and that changes the SNR. In this semi-classical model, we add fluctuation variables after having applied the gain and then calculate the corresponding change in the SNR. The output field ensemble of a Raman amplifier in the linear gain regime is

$$A_{\text{out}} = G^{1/2}\left[x_0 + \delta x + i(p_0 + \delta p)\right] + \delta a_1 + i\delta a_2, \tag{A.1}$$

where δa_j is the fluctuation in quadrature j of the spontaneous emission associated with the physical process that provided the gain. Defining the SNR as Eq. (3.20) and the Raman NF as the ratio $\text{SNR}_{\text{in}}/\text{SNR}_{\text{out}}$, we get

$$\text{NF} = \frac{\text{SNR}_{\text{in}}}{\text{SNR}_{\text{out}}} \approx 1 + \frac{4\langle \delta a^2 \rangle}{G\,\hbar\omega B_0}, \tag{A.2}$$

where a large photon number was assumed and it was furthermore assumed that the statistics of the fluctuations in both quadratures are equal, so $\langle \delta a_1^2 \rangle = \langle \delta a_2^2 \rangle = \langle \delta a^2 \rangle$. To evaluate the NF the variance of δa, which is equal to the second order moment $\langle \delta a^2 \rangle$ because δa has zero mean value, must be determined.

Classical photon number equations describing the Raman interaction among two waves at different wavelengths are shown in textbooks on nonlinear optics [57] and it is custom to approximate the lower wavelength component (the anti-Stokes component or pump in the context of Raman amplifiers) by a constant but here we also need to consider the opposite case of the higher wavelength component (the Stokes component) being much stronger than the lower wavelength component and hence approximate that by a constant. Likewise, the mean output power of (A.1) is

$$\langle |A_{\mathrm{S,out}}|^2 \rangle = G(x_0^2 + p_0^2) + \hbar\omega_{\mathrm{S}} B_0 G/2 + 2\langle \delta a_{\mathrm{S}}^2 \rangle \tag{A.3}$$

$$\langle |A_{\mathrm{AS,out}}|^2 \rangle = L(x_0^2 + p_0^2) + \hbar\omega_{\mathrm{AS}} B_0 L/2 + 2\langle \delta a_{\mathrm{AS}}^2 \rangle, \tag{A.4}$$

where (A.3) describes the weak Stokes component that receives Raman gain G from the strong anti-Stokes component, and (A.4) describes the weak anti-Stokes component that depletes a factor L by giving energy to the strong Stokes component. The second term of each equation is the amplification/depletion of the vacuum fluctuations explicitly included in (A.1) and they are artifacts of the semi-classical modeling; $\langle \delta a_{\mathrm{S}}^2 \rangle$ and $\langle \delta a_{\mathrm{AS}}^2 \rangle$ should be chosen to counter-balance these terms as well as including spontaneous emission. If $\langle \delta a_{\mathrm{S}}^2 \rangle$ and $\langle \delta a_{\mathrm{AS}}^2 \rangle$ are chosen to be

$$\langle \delta a_{\mathrm{S}}^2 \rangle = ([G(z) - 1](n_{\mathrm{T}} + 1)/2 - [G(z) - 1]/4)\, \hbar\omega_{\mathrm{S}} B_0 \tag{A.5}$$

$$\langle \delta a_{\mathrm{AS}}^2 \rangle = ([1 - L(z)]n_{\mathrm{T}}/2 + [1 - L(z)]/4)\, \hbar\omega_{\mathrm{AS}} B_0, \tag{A.6}$$

and they are inserted into (A.3) and (A.4), then one gets the equivalent of what may be derived from the classical equations. The Raman NF of a signal on either side of a strong pump is now easily calculated using (A.2) to be

$$\mathrm{NF_S} = \frac{1}{G(z)} + \frac{2[G(z) - 1](n_{\mathrm{T}} + 1)}{G(z)} \to 2(n_{\mathrm{T}} + 1) \tag{A.7}$$

$$\mathrm{NF_{AS}} = \frac{1}{L(z)} + \frac{2[1 - L(z)]n_{\mathrm{T}}}{L(z)} \to (1 + 2n_{\mathrm{T}})/L(z). \tag{A.8}$$

The arrows indicate the tendencies in case of large Raman interaction, i.e. $G \gg 1$ and $L \ll 1$. In the limit of low temperature, $n_{\mathrm{T}} \approx 0$, these formulas give the expected results of a 3-dB NF on the S side and a NF equal to the depletion on the AS side.

Considering case (i) and case (i) of Fig. 3.10, in which there are two pumps and two small signals, the results (A.7) and (A.8) do not immediately apply. However, if one regards the two pumps as one wave component with power $P = P_{\mathrm{p}} + P_{\mathrm{q}}$ and the signal and idler as one

small signal, one has an artificial two-component system that may be described by the results of this appendix. The frequency separation between the two components is $\Omega_{\mathrm{pi}} = \omega_{\mathrm{p}} - \omega_{\mathrm{i}}$ in case (a) and Ω_{ip} in case (b).

A.2 Analytical solutions to single-mode four-wave mixing equations

This appendix shows how to solve the four-wave mixing (FWM) equations in the case of degenerate amplification MI. The equations are derived in Ch. 2, and they read

$$\begin{aligned}\partial_z E_{\mathrm{s}} = i\gamma_{\mathrm{s}} \Big[&|E_{\mathrm{s}}|^2 E_{\mathrm{s}} + (2 - f_R)\left(|E_{\mathrm{p}}|^2 + |E_{\mathrm{i}}|^2\right) E_{\mathrm{s}} + (1 - f_R) E_{\mathrm{p}}^2 E_{\mathrm{i}}^* \mathrm{e}^{-i\Delta\beta z} \\ &+ f_R \left(|E_{\mathrm{p}}|^2 \tilde{h}_R(\Omega_{\mathrm{ps}}) + |E_{\mathrm{i}}|^2 \tilde{h}_R(\Omega_{\mathrm{is}}) \right) E_{\mathrm{s}} \Big] - \frac{\alpha_{\mathrm{s}}}{2} E_{\mathrm{s}},\end{aligned} \tag{A.9}$$

$$\begin{aligned}\partial_z E_{\mathrm{p}} = i\gamma_{\mathrm{p}} \Big[&|E_{\mathrm{p}}|^2 E_{\mathrm{p}} + (2 - f_R)\left(|E_{\mathrm{s}}|^2 + |E_{\mathrm{i}}|^2\right) E_{\mathrm{p}} + 2(1 - f_R) E_{\mathrm{s}} E_{\mathrm{i}} E_{\mathrm{p}}^* \mathrm{e}^{i\Delta\beta z} \\ &+ f_R \left(|E_{\mathrm{s}}|^2 \tilde{h}_R(\Omega_{\mathrm{sp}}) + |E_{\mathrm{i}}|^2 \tilde{h}_R(\Omega_{\mathrm{ip}}) \right) E_{\mathrm{p}} \Big] - \frac{\alpha_{\mathrm{p}}}{2} E_{\mathrm{p}},\end{aligned} \tag{A.10}$$

$$\begin{aligned}\partial_z E_{\mathrm{i}} = i\gamma_{\mathrm{i}} \Big[&|E_{\mathrm{i}}|^2 E_{\mathrm{i}} + (2 - f_R)\left(|E_{\mathrm{p}}|^2 + |E_{\mathrm{s}}|^2\right) E_{\mathrm{i}} + (1 - f_R) E_{\mathrm{p}}^2 E_{\mathrm{s}}^* \mathrm{e}^{-i\Delta\beta z} \\ &+ f_R \left(|E_{\mathrm{p}}|^2 \tilde{h}_R(\Omega_{\mathrm{pi}}) + |E_{\mathrm{s}}|^2 \tilde{h}_R(\Omega_{\mathrm{si}}) \right) E_{\mathrm{i}} \Big] - \frac{\alpha_{\mathrm{i}}}{2} E_{\mathrm{i}},\end{aligned} \tag{A.11}$$

where $\gamma_j = \omega_j n_2/(cA_{\mathrm{eff}})$ [1/(W m)] and $n_2 = 3\chi^{(3)}\epsilon_0/(4n_{\mathrm{eff}}^2 c)$ [m^2/W] is the nonlinear refractive index. Ignoring the Raman scattering and loss terms, then in the undepleted pump regime where the pump is always of much larger amplitude than the two side bands the pump equation reduces to

$$\partial_z E_{\mathrm{p}} = i\gamma_{\mathrm{p}} |E_{\mathrm{p}}|^2 E_{\mathrm{p}}, \tag{A.12}$$

which has the simple solution

$$E_{\mathrm{p}}(z) = \sqrt{P_{\mathrm{p}}} \mathrm{e}^{i\gamma_{\mathrm{p}} P_{\mathrm{p}} z}, \tag{A.13}$$

where P_{p} is the constant pump power. Inserting this result into the signal and idler equations and neglecting terms that do not hold the pump amplitude squared, then

$$\partial_z E_{\mathrm{s}} = i\gamma_{\mathrm{s}}(2 - f_R) P_{\mathrm{p}} E_{\mathrm{s}} + i\gamma_{\mathrm{s}}(1 - f_R) P_{\mathrm{p}} E_{\mathrm{i}}^* \mathrm{e}^{-i\Delta\beta z + 2i\gamma_{\mathrm{p}} P_{\mathrm{p}} z}, \tag{A.14}$$

$$\partial_z E_\mathrm{i} = i\gamma_\mathrm{i}(2-f_R)P_\mathrm{p}E_\mathrm{i} + i\gamma_\mathrm{i}(1-f_R)P_\mathrm{p}E_\mathrm{s}^* \mathrm{e}^{-i\Delta\beta z + 2i\gamma_\mathrm{p}P_\mathrm{p}z}. \quad \text{(A.15)}$$

Making the following transformations

$$E_j = A_j \mathrm{e}^{i\gamma_j(2-f_R)P_\mathrm{p}z} \quad \text{(A.16)}$$

for both $j \in \{\mathrm{s},\mathrm{i}\}$, Eqs. (A.14) and (A.15) become

$$\partial_z A_\mathrm{s} = i\xi_\mathrm{s} A_\mathrm{i}^* \mathrm{e}^{-i\kappa z}, \quad \text{(A.17)}$$

$$\partial_z A_\mathrm{i} = i\xi_\mathrm{i} A_\mathrm{s}^* \mathrm{e}^{-i\kappa z}, \quad \text{(A.18)}$$

where $\xi_j = \gamma_j(1-f_R)P_j$ for both $j \in \{\mathrm{s},\mathrm{i}\}$ and $\kappa = \Delta\beta + 2\gamma_\mathrm{p}(1-f_R)P_\mathrm{p}$. Differentiating Eq. (A.17) and using both Eqs. (A.17) and (A.18), one finds

$$\partial_{zz} A_\mathrm{s} + i\kappa\partial_z A_\mathrm{s} - \xi_\mathrm{s}\xi_\mathrm{i} A_\mathrm{s} = 0, \quad \text{(A.19)}$$

where ∂_{zz} denotes double differentiation with respect to z. Solving this simple second order differential equation with the initial conditions appropriate for the degenerate PIA, $A_\mathrm{s}(0) = A_0$ and $A_\mathrm{i}(0) = 0$, the solution is

$$A_\mathrm{s}(z) = A_0 \left(\cosh(gz) + \frac{i\kappa}{2g} \sinh(gz) \right) \mathrm{e}^{-i\frac{\kappa}{2}z}, \quad \text{(A.20)}$$

where $g^2 = \xi_\mathrm{s}\xi_\mathrm{i} - (\kappa/2)^2$. The difference between A_j and E_j is just a phase factor so the gain can be found directly by

$$G(z) = \frac{|A_\mathrm{s}(z)|^2}{|A_\mathrm{s}(0)|^2} = 1 + \frac{\xi_\mathrm{s}\xi_\mathrm{i}}{g^2} \sinh^2(gz). \quad \text{(A.21)}$$

The other FWM processes can be solved in a similar way.

Appendix B

Submitted paper: Experimental characterization of Raman overlaps between mode-groups

Experimental characterization of Raman overlaps between mode-groups

Erik N. Christensen[1,+,*], Jacob G. Koefoed[1,+], Søren M. M. Friis[1], Mario A. Usuga Castaneda[1], and Karsten Rottwitt[1]

[1]Department of Photonics Engineering, Technical University of Denmark, 2800 Kongens Lyngby, Denmark
[*]ench@fotonik.dtu.dk
[+]These authors contributed equally to this work

ABSTRACT

Mode-division multiplexing has the potential to further increase data transmission capacity through optical fibers. In addition, distributed Raman amplification is a promising candidate for multi-mode signal amplification due to its desirable noise properties and the possibility of mode-equalized gain. In this paper, we present an experimental characterization of the intermodal Raman intensity overlaps of a few-mode fiber using backward-pumped Raman amplification. By varying the input pump power and the degree of higher order mode-excitation for the pump and the signal in a 10 km long two-mode fiber, we are able to characterize all intermodal Raman intensity overlaps. Using these results, we perform a Raman amplification measurement and demonstrate a mode-differential gain of only 0.25 dB per 10 dB overall gain. This is, to the best of our knowledge, the lowest mode differential gain achieved for amplification of mode division multiplexed signals in a single fiber.

Introduction

During the past decade, the increase in data capacity per fiber has slowed relative to the rapid progress in the 1990's while, at the same time, the demand for capacity continues to grow exponentially.[1] Current methods for signal multiplexing, i.e. wavelength-, polarization-, time-, and quadrature-division multiplexing, are approaching their fundamental limits so new means of multiplexing are needed. Space-division multiplexing[2] in the form of multi-core fibers has already been used to achieve new heights in data capacity from a single laser source;[3,4] in single-core fibers supporting multiple spatial modes, long-distance propagation of optical signals has been demonstrated;[5,6] and recently, data transmission in a few-mode multi-core fiber was presented.[7] One important challenge of mode-division multiplexing (MDM) systems is building multi-mode optical amplifiers, that have mode-equalized amplification of all spatial modes, to compensate for example for distributed fiber loss; it is desirable for a multi-mode amplifier to avoid mode-dependent gain (MDG) in order to maximize capacity.[8] As for traditional single-mode systems, discrete Erbium-doped fiber amplifiers have been applied to multi-mode systems as well and low MDG has been achieved for some of the modes in fibers with specially designed Erbium-doping profiles.[9–11]

Another approach to counter-balance fiber losses is distributed Raman amplification, which is also widely used already in single-mode networks due to its superior noise properties in the backward-pumped configuration.[12] Furthermore, it has been shown theoretically that minimal MDG is possible by coupling pump power into a specific combination of spatial modes,[13] or by optimizing fiber design,[14] which makes Raman amplifiers a promising candidate for realizing low-loss, multi-mode transmission links over large distances.

Earlier work has demonstrated Raman gain between higher-order modes with the pump in only one mode.[5,15,16] Besides the obvious challenges related to exciting the pump in a specific combination of modes, it may often also prove difficult to determine the exact mode combination that leads to the lowest possible MDG because the required fiber data are unavailable from the fiber supplier. In this paper, we present an experimental characterization of the intermodal Raman intensity overlap of the guided modes of a two-moded (6 modes counting polarisation and LP_{11a} and LP_{11b}) few-mode fiber (FMF) using mechanically induced long-period gratings (LPGs) to excite the higher-order modes. Using the obtained results, we demonstrate backward pumped Raman amplification of a continuous wave (CW) signal through 10 km of a two-moded fiber with a very low MDG of 0.25 dB per 10 dB gain by pumping in a combination of the LP_{01} and LP_{11} modes. The mode-differential gain obtained required no prior knowledge about the Raman intensity overlaps of the fiber.

Results

The purpose of the present work is to characterize the intermodal Raman overlaps and use them to achieve a minimal MDG in a backward-pumped Raman fiber amplifier. This is done by coupling the pump light into the fiber in the correct combination of the LP_{01}- and LP_{11}-modes. As will be discussed in the Methods section below, due to strong mode-coupling, the two-fold quasi-degenerate LP_{01}-modes and four-fold quasi-degenerate LP_{11}-modes are simply considered as two distinct groups of modes. We carry out two measurements: Firstly, the Raman gain of a continuous wave signal in the LP_{01}-mode is measured vs. total pump input power for five different modal compositions of the pump, i.e. different combinations of the LP_{01}- and the LP_{11}-modes. Secondly, both pump and signal are converted to LP_{11}. This data is used to calculate the Raman intensity overlaps relative to the LP_{01}-LP_{01}-overlap, which is all that is needed to find the correct combination of pump modes.

Raman intensity modal overlaps

Assuming both pump, and signal to be CW sources, the signal power P_i^s, in spatial mode i, and the counter propagating $P_j^{p,-}$ and copropagating pump power $P_j^{p,+}$, in spatial mode j, is governed by[17]

$$\frac{dP_i^s}{dz} = -\alpha_s P_i^s + \gamma_R \left(\sum_j F_{i,j} (P_j^{p,+} + P_j^{p,-}) \right) P_i^s, \tag{1}$$

$$\frac{dP_j^{p,\pm}}{dz} = \mp \alpha_p P_j^{p,\pm} \mp \frac{\lambda_s}{\lambda_p} \gamma_R \left(\sum_j F_{i,j} P_i^s \right) P_j^{p,\pm} \tag{2}$$

where α_s and α_p are loss coefficients for signal and pump wavelengths λ_s and λ_p, and γ_R is related to the spontaneous Raman scattering cross section. Note that γ_R and $\alpha_{p,s}$ are assumed mode-independent. The intensity overlap integrals are defined as

$$F_{i,j} = \frac{\int I_i I_j \, dA}{\int I_i \, dA \int I_j \, dA}, \tag{3}$$

with I_i being the intensity of mode i integrated over the entire fiber cross section. Solving (1) and (2) using the undepleted pump approximation, we arrive at an expression for the on/off gain

$$G_i = \frac{P_i^s(L) \text{ (pump on)}}{P_i^s(L) \text{ (pump off)}} = \exp\left(\gamma_R L_{\text{eff}} \left(\sum_j F_{i,j} P_j^{p,+}(0) + \sum_j F_{i,j} P_j^{p,-}(L) \right) \right), \tag{4}$$

where $L_{\text{eff}} = (1 - \exp[-\alpha_p L])/\alpha_p$ is the effective fiber length and L is the physical fiber length. The setup used is a backwards pumped configuration, where the pump has only two different spatial profiles (corresponding to LP_{01} and LP_{11}), so Eq. (4) can be reduced to

$$G_i = \exp\left(\gamma_R L_{\text{eff}} [\eta_p F_{i,11} + (1 - \eta_p) F_{i,01}] P_p \right), \tag{5}$$

for the signal in mode i, where η_p is the degree of conversion of the pump from LP_{01} to LP_{11} ($\eta_p = 0$ when all the pump power is in LP_{01}, and $\eta_p = 1$ when all the pump power is in LP_{11}) and P_p is the total input pump power (in all modes). Using the setup which is described in the methods section below, 65 measurements were carried out with 5 different conversion degrees and 13 different pump power levels varying from 0 to 1200 mW for each conversion degree. From the expected form of the gain, Eq. (5), we fitted a function of the form

$$G_{01}^{(\text{dB})} = (c_1 + c_2 \eta_p) P_p \tag{6}$$

to the data, where c_1 and c_2 are fitting parameters. The result is presented in Figure 1a where data and fitting lines are shown at the five different values of η_p. The obtained values for the fitting parameters are $c_1 = 8.50$ dB/W and $c_2 = -4.48$ dB/W. The theoretical expression is in excellent agreement with the obtained data with these values of the fitting parameters. From these values the ratio of the Raman intensity overlaps between the LP_{01}-LP_{01}-modes and LP_{01}-LP_{11}-modes is obtained

$$\frac{F_{01,11}}{F_{01,01}} = 1 + \frac{c_2}{c_1} = 0.47, \tag{7}$$

by comparing (5) and (6). This result agrees well with the value of 0.48 obtained from simulated mode-profiles provided by the fiber supplier.

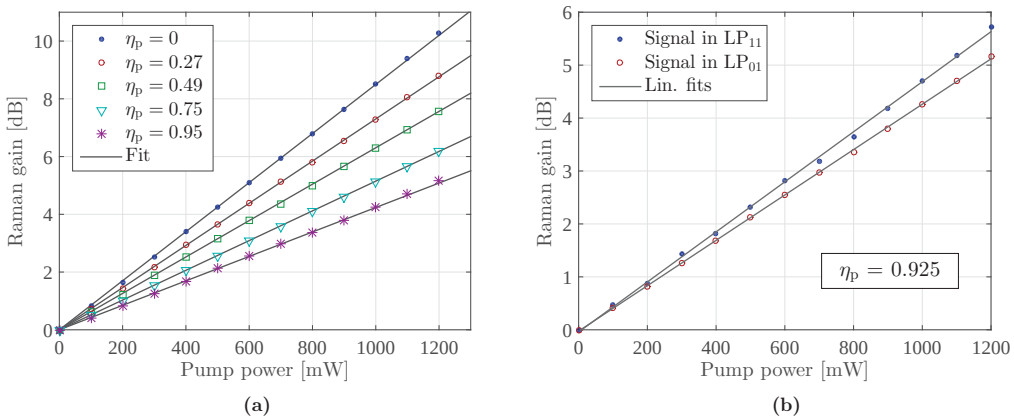

Figure 1. (**a**) Measured Raman gain vs. input pump power for five different pump conversion degrees, η_p; the lines result from the two-parameter fit evaluated at each conversion degree. (**b**) Measurements of Raman gain for signal and pump in LP_{11}. For comparison is shown the measurement with pump in LP_{11} and signal in LP_{01}.

Table 1. Measured values for overlap integrals relative to the LP_{01}-LP_{01} overlap.

	LP_{01}-LP_{01}	LP_{11}-LP_{01}	LP_{11}-LP_{11}
Measurement	1	0.47	0.56

Subsequently, the signal was coupled to the LP_{11}-mode with the highest attainable efficiency, ($\eta_p > 0.99$), and the pump was converted to the LP_{11}-mode with an efficiency of $\eta_p = 0.925$, see the Methods section for details, and the Raman gain of the LP_{11}-signal was measured vs. the input pump power. A linear function of the type

$$G_{11}^{\mathrm{dB}} = c_3 P_p, \tag{8}$$

was fitted to the data. From this the ratio $\frac{F_{11,11}}{F_{01,01}}$ is calculated, taking into account the pump conversion degree. The slope obtained from the fit to the LP_{11}-LP_{11} -data was $c_3 = 4.74$ dB/W. We assume wavelength independence of the overlap integrals (i.e. that the LP_{01}-LP_{11} and LP_{11}-LP_{01} overlaps are nearly identical). By comparison of Eqs. (8) and (6) to (5) we note that $c_1 = kF_{01,01}$ and $c_3 = k(F_{01,11} + \eta_p(F_{11,11} - F_{01,11}))$ with $k = 10\log_{10}(e)\gamma_R L_{\mathrm{eff}}$. Using Eq. (7) for the ratio $F_{01,11}/F_{01,01}$, these two expressions can be rearranged to give

$$\frac{F_{11,11}}{F_{01,01}} = \frac{c_3}{c_1\eta_p} - \frac{1-\eta_p}{\eta_p}\left(1 + \frac{c_2}{c_1}\right) = 0.56. \tag{9}$$

This is compared to the simulated values for LP_{11a}-LP_{11a} and LP_{11a}-LP_{11b} of 0.72 and 0.24, respectively. The measured overlap is, as expected, an intermediate value that depends on the mode-coupling within the LP_{11} mode-group. In table 1 the measured overlaps are summarized, and in table 2 the simulated overlaps are shown. Notice that the overlaps are normalized so that the LP_{01}-LP_{01}-overlap equals one.

Mode-equalized Gain Based on Measured Overlaps

Since the LP_{11}-LP_{11} and LP_{11}-LP_{01} intensity overlaps often turn out to be very similar in FMFs, relatively low differential gain can be obtained by simply launching the pump completely into LP_{11}. This was experimentally verified by R. Ryf *et al.*[6] where a differential gain of 0.5 dB per 10 dB of gain was observed. For the fiber used in this work, such a scheme results in a differential gain of 1 dB per 10 dB of gain as obtained from the data shown in Figure 2b (the differential gain in the figure is slightly lower since the pump is only converted 95 % into LP_{11}). Using our knowledge of the intensity overlap integrals, the

Table 2. Simulated overlap integrals for all modes.

	LP_{01}	LP_{11a}	LP_{11b}
LP_{01}	1	0.48	0.48
LP_{11a}	0.48	0.72	0.24
LP_{11b}	0.48	0.24	0.72

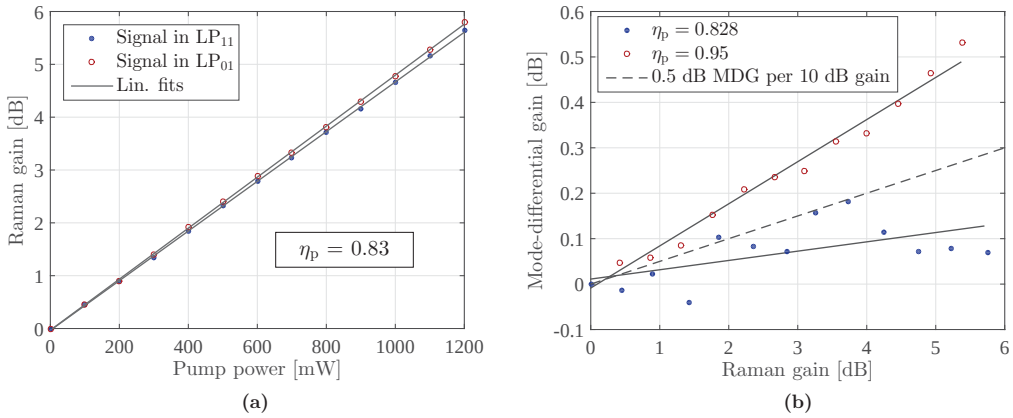

Figure 2. (**a**) Raman gain for both a LP_{01} and LP_{11}-signal with a pump in the mixture of 83 % LP_{11} and 17 % LP_{01} demonstrating near-equal gain for the two signals. (**b**) MDG between the two signal modes for pump almost completely converted to LP_{11} and pump in the mixture of 83 % LP_{11} and 17 % LP_{01}. A line for 0.5 dB gain difference per 10 dB gain is included for reference.

condition for equal signal gain across the two signal-modes, $G_{11} = G_{01}$, can be written as

$$\eta_p F_{11,11} + (1-\eta_p)F_{01,11} = \eta_p F_{01,11} + (1-\eta_p)F_{01,01}. \tag{10}$$

This equation can be solved, using the experimentally obtained values for the ratios $F_{11,11}/F_{01,01}$ and $F_{01,11}/F_{01,01}$, to obtain an equal-gain pump conversion of

$$\eta_{p,eq} = \frac{1 - F_{01,11}/F_{01,01}}{1 + F_{11,11}/F_{01,01} - 2F_{01,11}/F_{01,01}} = 0.854\ (= 8.35\ \text{dB conversion}). \tag{11}$$

In Figure 2a the results of measuring a signal launched first completely in LP_{01} and then completely in LP_{11} with a pump conversion of $\eta_p = 0.83$, i.e. slightly below the optimal value, are shown. From the figure it is clear that very little mode-dependent gain remains (compare with Figure 1b). The mode-differential gain as a function of the mean gain is seen in Figure 2b, showing a residual MDG of only 0.25 dB per 10 dB of Raman gain as obtained from the fitted lines. This differential mode gain is, to the best of our knowledge, the lowest that has so far been experimentally demonstrated. The reason for the fluctuation in MDG is most likely due to mode coupling between LP_{11a} and LP_{11b}. The LPG preferentially couples to the LP_{01} mode that we detect in the optical spectrum analyzer (OSA), as explained in the Methods section. This means that any mode coupling between LP_{11a} and LP_{11b} shows up as a small variation in the measured amplified signal. In the $\eta_p = 0.83$ (blue dot) measurement the back coupling is slightly more unstable compared to the $\eta_p = 0.95$ (red circle). This is due to the different configuration of the back coupling LPG.

Methods

The intermodal Raman gain is measured using the experimental setup shown in Figure 3. The setup is a distributed backwards pumped multi-mode Raman amplifier with a CW laser operated at 1550 nm as the signal source, and an unpolarized 1455 nm Raman fiber laser used for optical pumping. The characterized fiber is a 10 km, 2-moded graded-index fiber.

Higher-Order Mode excitation

The excitation of higher-order modes is achieved by use of mechanically induced LPGs, which are created by pressing the fiber between a periodically grooved aluminum block and a rubber pad. This creates a periodic perturbation in the fiber index, which induces mode coupling if the pitch of the induced gratings matches the difference in propagation constants of the modes.[18]

Using a broadband supercontinuum source at the signal input the mode-converted wavelengths are observed in the OSA_2 as a drop in the power spectrum due to the FMF to single mode fiber splice working as a mode filter. The effective pitch of the LPG is changed by adjusting the angle of the grooves with respect to the fiber, until maximum mode-conversion is achieved at the signal wavelength. The use of a supercontinuum source for calibration is not strictly necessary if the difference in propagation constant for the modes of interest is known, but it facilitates the excitation process. Based on the knowledge of the propagation constants the pitch for the pump wavelength was calculated to be 527 μm, which is in excellent agreement with the 523 μm pitch experimentally observed at maximum conversion. The LPGs are polarization dependent,[18] so a polarization controller (PC) is used to optimize conversion of the polarized signal source. After propagation through the fiber the signal is converted back to the fundamental mode using a second LPG.

From standard mode-coupling theory the coupling strength between the modes in a step-index fiber is given by[19]

$$K(z) = \frac{\pi}{\lambda n_{\text{core}}} \frac{\int \Delta\varepsilon(r,\phi,z)\psi_1(r,\phi)\psi_2(r,\phi)\,\mathrm{d}A}{\int \psi_1^2(r,\phi)\,\mathrm{d}A}, \tag{12}$$

where $\psi_{1,2}$ are the scalar mode profiles of the fiber. Since the grooves of the mechanical block are only applied to the fiber from one direction, the perturbation $\Delta\varepsilon(r,\phi,z)$ is asymmetric with respect to this direction. Since the LP_{01} mode is a circularly symmetric mode, we expect that mainly the LP_{11} mode which is spatially asymmetric with respect to the pertubation direction is excited in the induced grating. However, since we use an unpolarized pump, both polarizations of this spatial mode are excited resulting in an almost equal excitation of the four full-vectorial modes (TE_{01}, TM_{01}, HE_{21a} and HE_{21b}) that constitute the pseudo-LP_{11} modes. The strong coupling between these modes is expected to quickly smooth out any difference in the excitation.[17] Thus, following a similar approach as Antonelli *et al.*,[20] we only consider the excitation of the quasi-degenerate groups of modes, LP_{01} and LP_{11}, consisting of two and four nearly degenerate modes, respectively. In this regard, the measured overlaps are essentially an average over these groups.

Characterization of fiber under test

For all measurements the signal power launched is 0.4 mW, and the launched pump power is varied from 0 to 1200 mW. For each pump power the on/off gain is measured by OSA_2. The ratio of the LP_{01}-LP_{01} and LP_{01}-LP_{11} overlaps is found with the signal in LP_{01} and the pump in varying mixtures of both LP_{11} and LP_{01} by adjusting LPG_2 to the desired pump mode conversion.

For the LP_{11}-LP_{11} gain measurement LPG_1 and PC_1 were adjusted to obtain more than 99% signal conversion, and LPG_2 was adjusted to obtain a maximum of $\eta_p = 0.92$ pump conversion; The lower pump conversion is due to the pump being unpolarized. The LPG_2 conversion bandwidth is large enough such that, by optimizing PC_2, 12 dB of the signal is converted back to LP_{01}. The back conversion is necessary due to the mode-filtering effect of the single-mode to multi-mode fiber splice. The gain of the back converted signal is the LP_{11}-LP_{11} gain.

Equal modal gain measurement

To equalize the modal gain, we first adjust LPG_2 so that we are pumping in a combination of the LP_{11} and LP_{01} modes very close to the optimal value 85% conversion as obtained from the previous measurements, see Eq. (11). We then first adjust LPG_1 and PC_1 to maximize signal conversion ($\eta_p > 0.99$) and measure the gain of this mode. Then LPG_1 is lifted so that the signal is a pure LP_{01}-mode and the gain for this mode is measured. The difference in the gain for these two signal-modes then gives the mode-differential gain.

Conclusion

We have experimentally characterized the intermodal Raman overlaps in a few-mode fiber by varying the launched pump power and the conversion efficiencies of the pump and signal using mechanically induced long-period gratings for mode excitation. The overlap integrals (relative to the LP_{01}-LP_{01} overlap) for all modal combinations were obtained in this way for a specific few-mode fiber. By use of the obtained overlaps, it was further demonstrated how a mode-differential gain of

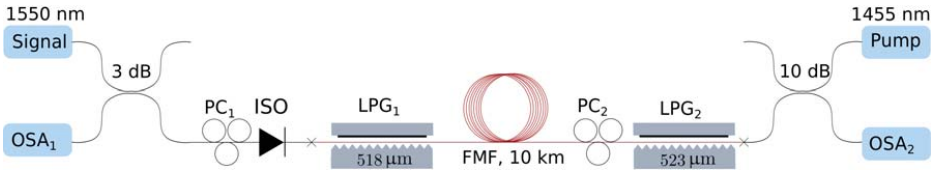

Figure 3. The experimental setup used for all measurements. ISO: Isolator, OSA:optical spectrum analyser, PC: polarization controller, LPG: long period grating, FMF: few-mode fiber. Red lines signify FMF and black lines single mode fiber with crosses indicating splices. The number on the gratings indicate pitch.

only 0.25 dB per 10 dB overall gain is obtained by pumping in a specific combination of the LP_{11} and LP_{01} modes. In the specific few-mode fiber under test, the differential gain was shown to be significantly lower when pumping in the determined combination of modes compared to when pumping only in LP_{11}.

References

1. Essiambre, R. J. & Tkach, R. W. Capacity trends and limits of optical communication networks. *Proceedings of the IEEE* **100**, 1035–1055 (2012).
2. Richardson, D. J., Fini, J. M. & Nelson, L. E. Space-division multiplexing in optical fibres. *Nature Photonics* **7**, 354–362 (2013).
3. Zhu, B. *et al.* Seven-core multicore fiber transmissions for passive optical network. *Optics Express* **18**, 11117–11122 (2010).
4. Hu, H. *et al.* Single Source 5-dimensional (Space-, Wavelength-, Time-, Polarization-, Quadrature-) 43 Tbit/s Data Transmission of 6 SDM × 6 WDM × 1.2 Tbit/s Nyquist-OTDM-PDM-QPSK. In *CLEO Postdeadline Pap.*, JTh5B.10 (2014).
5. Ryf, R. *et al.* Mode-division multiplexing over 96 km of few-mode fiber using coherent 6×6 MIMO processing. *Journal of Lightwave Technology* **30**, 521–531 (2012).
6. Ryf, R. *et al.* Mode-multiplexed transmission over a 209-km DGD-compensated hybrid few-mode fiber span. *IEEE Photonics Technology Letters* **24**, 1965–1968 (2012).
7. van Uden, R. G. H. *et al.* Ultra-high-density spatial division multiplexing with a few-mode multicore fibre. *Nature Photonics* **8**, 865–870 (2014).
8. Winzer, P. J. & Foschini, G. J. MIMO capacities and outage probabilities in spatially multiplexed optical transport systems. *Optics Express* **19**, 16680 (2011).
9. Le Cocq, G. *et al.* Modeling and characterization of a few-mode EDFA supporting four mode groups for mode division multiplexing. *Optics Express* **20**, 27051–61 (2012).
10. Ip, E. *et al.* 146λ x 6 x 19-Gbaud wavelength-and mode-division multiplexed transmission over 10 x 50-km spans of few-mode fiber with a gain-equalized few-mode EDFA. *Journal of Lightwave Technology* **32**, 790–797 (2014).
11. Jung, Y. *et al.* First demonstration of cladding pumped few-moded EDFA for mode division multiplexed transmission. *Conference on Optical Fiber Communication, Technical Digest Series* **22**, 29008–29013 (2014).
12. Islam, M. N. Raman amplifiers for telecommunications. *IEEE Journal on Selected Topics in Quantum Electronics* **8**, 548–559 (2002).
13. Zhou, J. An analytical approach for gain optimization in multimode fiber Raman amplifiers. *Optics Express* **22**, 21393 (2014).
14. Weng, Y., Wang, T. & Pan, Z. Optimization of mode-dependent gain efficiency based on intermodal Raman scattering for few-mode distributed Raman amplifier. In *Conference on Lasers and Electro-Optics*, SW1P.5 (Optical Society of America, 2016).
15. Trabold, B. M., Abdolvand, a., Euser, T. G., Walser, a. M. & Russell, P. S. J. Amplification of higher-order modes by stimulated Raman scattering in H2-filled hollow-core photonic crystal fiber. *Optics Letters* **38**, 600–2 (2013).

16. Rottwitt, K. & Povlsen, J. H. Analyzing the fundamental properties of Raman amplification in optical fibers. *Journal of Lightwave Technology* **23**, 3597–3605 (2005).

17. Ryf, R., Essiambre, R.-J., von Hoyningen-Huene, J. & Winzer, P. J. Analysis of Mode-Dependent Gain in Raman Amplified Few-Mode Fiber. In *OFC/NFOEC Tech. Dig.* (2012).

18. Savin, S., Digonnet, M. J., Kino, G. S. & Shaw, H. J. Tunable mechanically induced long-period fiber gratings. *Optics Letters* **25**, 710–712 (2000).

19. Okamoto, K. *Fundamentals of Opticals Waveguides* (Elsevier, 2006), second edn.

20. Antonelli, C., Mecozzi, A. & Shtaif, M. Raman amplification in multimode fibers with random mode coupling. *Optics letters* **38**, 1188–90 (2013).

Acknowledgements

The authors acknowledge financial supported for the research by The Danish Council for Independent Research, research grant: DFF – 4184-00433, and InnovationsFonden for funding the e-space project (#0603-00514B) and also the center of excellence: Silicon Photonics for Optical Communications granted by the Danish National Research Foundation (DNRF123)

Author contributions statement

E.N.C and J.G.K performed experiments and wrote the manuscript. S.M.M.F, M.A.U.C and K.R contributed to theory and conceiving experiments. All authors reviewed and revised the manuscript.

Additional information

Competing financial interests
The authors have no competing financial interests to disclose.

Appendix C

Submitted paper: Noise Contributions of Linear Pump Mode Coupling in Few-Mode Raman Fiber Amplifiers

Noise Contributions of Linear Pump Mode Coupling in Few-Mode Raman Fiber Amplifiers

Søren M. M. Friis and Karsten Rottwitt

***Abstract*—We review recent work on few-mode Raman fiber amplifiers and address some of the connected challenges: mode dependent gain and linear mode coupling. Deterministic linear mode coupling in a transmitted signal can be mitigated by multiple-input multiple-output processing techniques in linear transmission systems but if distributed Raman amplification is employed, mode coupling introduce a new source of amplification noise. We employ a model of few-mode Raman amplification and a numerical implementation of random linear mode coupling in the pump to study fundamental limiting effects of few-moded Raman fiber amplifiers. Conditions for equal modal gain and balance between Raman gain and fiber attenuation are derived.**

By quantifying the degree of both intra- and inter-mode group linear mode coupling, we show how the signal-to-noise ratio of a transmitted signal is affected by the presence of linear mode coupling in the pump in the depleted as well as in the undepleted pump regime.

***Index Terms*—IEEE, IEEEtran, journal, LATEX, paper, template.**

I. Introduction

INDIVIDUAL spatial modes in few-mode fibers (FMF) have been shown to hold great promise as a means to enhance the capacity in an optical communication system since they form a basis in a space division multiplexed (SDM) communication system. Each individual mode is ideally orthogonal to all other modes and capable of carrying information. However, one challenge in such systems is optical amplification. An amplifier in an SDM system needs to be able to amplify individual modes with the same gain and with the same noise performance and at multiple wavelengths at the same time.

Recent SDM transmission system experiments have included discrete few-moded Erbium-doped fiber amplifiers and distributed Raman fiber amplifiers. In 2012, N. Bai *et al.* investigated in [1] a few-moded Erbium-doped fiber amplifier that supported three spatial modes, LP01, LP11a and LP11b. Here and in the following, the notion of LP modes refer to scalar linearly polarized modes as they exist in weakly guiding stepindex optical fibers [2]. The amplifier was used to boost the signal just before the input of the receiver. The impact of using different spatial pump modes was considered and the mode dependent gain, i.e. the difference in gain between the LP01 and the LP11a and LP11b modes across the entire C-band, was shown to be 1 dB when the pump power was in the LP21 mode for an average modal gain of $\sim$ 7 dB. V.A.J.M Sleiffer *et al.* demonstrated in [3] the use of an inline few-moded Erbium-doped fiber amplifier, providing gain for the spatial modes: LP01, LP11a and LP11b. The amplifier provided a modal gain of around 17 dB across the full C-band with a mode dependent gain close to 2 dB.

R. Ryf and co-workers demonstrated in 2011 [4] the use of distributed Raman amplification to counteract the loss in a 137 km long FMF. The signals were situated in the LP01, and the LP11 mode while the pump was launched into the LP11 mode. The Raman fiber amplifier used in their experiment provided a maximum gain of about 8 dB in the wavelength range from 1550 nm to 1570 nm with a variation in gain between modes of less than 0.5 dB. It is noted that in their experiment the signals experienced an effective noise figure, as defined in [5], of -1.5 dB in the same wavelength range. In 2012, R. Ryf and *et al.* [6] showed a transmission through a 209 km long FMF using distributed Raman gain to counterbalance intrinsic fiber loss. The signal consisted of polarization multiplexing of the three spatial modes LP01, LP11a and LP11b. The backward pumped distributed Raman fiber amplifier provided around 10 dB of gain at 1550 nm, obtained by using 800 mW of pump power coupled into the LP11 mode.

As already pointed out, one challenge in using optical FMF amplifiers is the mode dependent gain. In discrete Erbium-doped fiber amplifiers, Q. Kang *et al.* [7] have proposed a fiber design that has enabled a 6 mode group amplifier providing a gain around 25 dB for all 6 modes with a maximum gain difference among the 6 modes of only 0.6 dB. R. Ryf *et al.* analyzed mode dependent gain theoretically in a distributed Raman fiber amplifier in [8]. Among four mode groups a mode dependent gain of 0.13 dB, for a Raman gain of 10 dB on each signal mode group, was predicted. To achieve this result, the pump power was distributed among two different mode groups.

The task of minimizing the difference in gain among different signal modes at different signal wavelengths is a challenging problem. The solution is either to optimize the fiber design for minimum mode dependent gain or to adjust the configuration of the pump at the amplifier input; for example distributing the pump power among different wavelengths or spatial modes. For the latter solution, a numerical approach to optimizing the pump power distribution in different spatial modes has been addressed by J. Zhou in [9].

In analogy to the mode dependent gain, the noise performance of few-mode amplifiers is also mode dependent. However, evaluating the gain and noise performance is further complicated since the power distribution within individual modes, be it signal or pump modes, may shift during propagation. This linear and distributed mode coupling is not caused

S. M. M. Friis and K. Rottwitt are with the Department of Photonics Engineering, Technical University of Denmark, 2800 Kongens Lyngby, Denmark e-mail: karo@fotonik.dtu.dk.

Manuscript received April 19, 2005; revised August 26, 2015.

by the amplifying mechanism but for example due to small perturbations in the fiber, splices between fiber segments, or due to the fact that scalar LP modes, as we consider in the following, are composed of several spatial and polarization degenerate modes that couple strongly to each other during propagation. Thus, mode coupling exist in space division multiplexed systems even without amplification. This type of coupling is deterministic in nature and may be mitigated by using MIMO techniques [10]. However, the complexity of using MIMO scales quadratically with the number of modes and even though the impact of mode coupling may be mitigated, mode coupling still results in a transmission penalty [11]. Consequently low linear mode coupling is desirable [11]–[13].

Another class of mode coupling is random linear mode coupling (RLMC) that happens because of stochastic perturbations along the fiber, as for example stochastic mechanical perturbations or temperature perturbations; the impact of RLMC in a single amplifier is a new noise source introduced in multi-mode systems. RLMC cannot be mitigated by MIMO and its impact is enhanced in amplifiers as for example a Raman fiber amplifier [14]. The reason for this is that in a system relying on distributed Raman amplification, the random mode coupling not only impacts the statistics of the output power of the signal due to mode dependent loss but even more dramatically, the signal is impacted by a random distributed mode coupling of the pump power as it couples between different modes each having a different Raman gain coefficient to individual modes.

As a means to minimize linear mode coupling, deterministic as well as random mode coupling, a fiber may be designed with a large separation between the effective refractive index of each mode. This has been investigated by L. Grüner-Nielsen *et al*. [11] and K. Jespersen *et al*. [15] and likewise its impact on the Raman gain [16] by C. Antonelli *et al.*. It has been demonstrated that the linear mode coupling decreases with increasing mode index difference, and it has been demonstrated that an index difference of $\Delta n = 1.3 \cdot 10^{-3}$ result in a linear mode coupling of -18.2 dB, measured in a 500 m fiber, whereas an index difference of $\Delta n = 2.8 \cdot 10^{-3}$ reduces the linear mode coupling to -25 dB, measured in a 30 km long fiber.

In this paper, we estimate the induced excess noise of distributed few-mode Raman fiber amplifiers due to linear mode coupling in the pump. We present a scheme with parameters that may be derived from experimental data, and we quantify the results in terms of mode differential gain and an induced noise figure (NF). Since deterministic mode coupling in the signal can be well mitigated by MIMO processing [17], we include only mode coupling among the pump modes; and because little is usually known about where in the fiber mode coupling takes place, we regard as a first approximation the pump mode couplings to be of random nature. Amplified spontaneous emission is omitted from the investigation for simplicity and should thus be considered an additional source of noise. The model of linear mode coupling is defined to represent the weak coupling regime where only a small amount of electromagnetic energy is expected to couple from one pump mode to another while propagating through the fiber; this is in contrast to earlier works that focus on the strong coupling regime [18]–[20].

II. Theory

In this section, basic propagation equations of stimulated Raman scattering are derived in the same fashion as Ref. [16] and equal modal gain conditions are derived; secondly, a numerical model of random linear mode coupling is presented.

A. Deterministic Propagation Equations

A nonlinear propagation equation suitable for describing multi-mode stimulated Raman scattering is derived and presented in Refs. [21], [22] and in the continuous wave regime it reads

$$\frac{\partial E_n^{(\mu)}}{\partial z} = \frac{i\omega_n \mathrm{e}^{-i\beta_n^{(\mu)} z}}{4N_n^{(\mu)}} \int \mathbf{F}_n^{(\mu)^*} \cdot \mathbf{P}_n^{(3)} dxdy, \tag{1}$$

where ω_n is the angular frequency at wave component n, $\beta_n^{(\mu)}$ is the propagation constant at frequency ω_n in mode μ, z is the longitudinal coordinate through the fiber, $\mathbf{F}_n^{(\mu)}(x,y)$ is a vector containing the field distribution functions of each of the three components of the electric field, and $N_n^{(\mu)}$ is a normalization term that ensure that the unit of the electric field amplitude, $E_n^{(\mu)}$, is the square root of watts, and it defined as [22]

$$\frac{1}{4}\iint \left[\mathbf{F}_n^{(\nu)^*} \times \mathbf{H}_n^{(\mu)} + \mathbf{F}_n^{(\mu)} \times \mathbf{H}_n^{(\nu)^*}\right] \cdot \hat{\mathbf{z}}\, dxdy = \delta_{\mu,\nu} {N_n^{(\mu)}}^2 \tag{2}$$

where $\mathbf{H}_n^{(\mu)}$ is the same for the magnetic field as $\mathbf{F}_n^{(\mu)}(x,y)$ is for the electric field. In the derivation of Eq. (1), the electric field was expanded in a set of continuous wave fields

$$\mathbf{E}(\mathbf{r},t) = \frac{1}{2}\sum_m \mathbf{A}_m(\mathbf{r})\mathrm{e}^{-i\omega_m t} + \text{c.c.} \tag{3}$$

and the time independent coefficient $\mathbf{A}_m$ is a sum over all modes at frequency ω_m,

$$\mathbf{A}_m = \sum_\nu \frac{\mathbf{F}_m^{(\nu)}(x,y)}{N_n^{(\nu)}} E_m^{(\nu)} \mathrm{e}^{i\beta_m^{(\nu)} z}. \tag{4}$$

The third order nonlinear induced polarization in Eq. (1) is the time independent coefficient of

$$\mathbf{P}^{(3)}(\mathbf{r},t) = \frac{1}{2}\sum_n \mathbf{P}_n^{(3)}(\mathbf{r})\mathrm{e}^{-i\omega_m t} + \text{c.c.} \tag{5}$$

To derive propagation equations for N continuous wave fields each with an arbitrary number of modes, we evaluate the nonlinear induced polarization as [22]

$$\mathbf{P}^{(3)}(\mathbf{r},t) = \epsilon_0 \chi^{(3)} \mathbf{E}(\mathbf{r},t) \int R(t-\tau)|\mathbf{E}(\mathbf{r},t)|^2 d\tau \tag{6}$$

where only one component of the susceptibility tensor $\chi_{ijkl}^{(3)}$ is included, i.e. the $\chi_{iiii}^{(3)} \equiv \chi^{(3)}$ where $i = x$ or y and $\chi^{(3)}$ is the total susceptibility (sum of Kerr and Raman susceptibilities). The response function is $R(t) = \frac{3}{2} f_R h_R(t)$ where $f_R = 0.18$ is the Raman fraction of the total susceptibility and $h_R(t)$ is the normalized time domain Raman response, which can be

parameterized as shown in Ref. [23]. The analysis is simplified if it assumed that all electric fields are linearly polarized such that $\mathbf{F}_n^{(\mu)} = F_n^{(\mu)}\hat{\mathbf{x}}$ where $\hat{\mathbf{x}}$ is a unit vector in the x direction; this simplification is convenient for communication fibers, which are often weakly guiding. Inserting Eq. (3) into Eq. (6) and only collecting terms that oscillate at ω_n; then inserting Eq. (6) and (4) into Eq. (1) and using that terms that require phase matching fall out, the final propagation equation becomes (see Ref. [24] for a similar process)

$$\frac{\partial E_n^{(\mu)}}{\partial z} = \frac{i\omega_n n_2 f_R}{c} E_n^{(\mu)} \sum_m \sum_\nu f^{(\mu,\nu)} |E_m^{(\nu)}|^2 \tilde{h}_R(\Omega_{mn}) \quad (7)$$

where $n_2 = 3\chi^{(3)}/(4\epsilon_0 c n_{\text{eff}}^2)$ where n_{eff} is the effective index of mode μ at frequency ω_n, $f^{(\mu,nu)}$ is the nonlinear mode overlap integral defined as

$$f^{(\mu,\nu)} = \frac{\int |F^{(\mu)}|^2 |F^{(\nu)}|^2 dxdy}{\int |F^{(\mu)}|^2 dxdy \int |F^{(\nu)}|^2 dxdy}, \quad (8)$$

where the subscript on $F_{(\mu)}$ was removed, thus assuming that the field distribution functions are equal at all wavelengths; since no wave components in this work (and for Raman amplifiers in silica in general) are separated by more than ca. 100 nm, this is a decent approximation. The function $\tilde{h}_R(\Omega_{mn})$ [23] is the frequency domain Raman response function; $\Omega_{mn} = \omega_m - \omega_n$ is the frequency shift from ω_n to ω_m. The set of equations (7) are readily converted to power by multiplying with the complex conjugate modal field amplitude $E_n^{(\mu)^*}$ and adding the complex conjugate of the resulting equation to itself, i.e.

$$\frac{\partial P_n^{(\mu)}}{\partial z} = -\alpha_n^{(\mu)} P_n^{(\mu)} + \frac{2i\omega_n n_2 f_R}{c} P_n^{(\mu)} \times \sum_m \sum_\nu f^{(\mu,\nu)} P_m^{(\nu)} \text{Im}\{\tilde{h}_R(\Omega_{mn})\}, \quad (9)$$

where $|E_n^{(\mu)}|^2 = P_n^{(\mu)}$ was used. The usual linear loss term with attenuation coefficient $\alpha_n^{(\mu)}$ was added by hand to account for distributed fiber losses. The two degenerate modes LP11a and LP11b form a mode group, which makes them more strongly coupled to each other than to modes outside the mode group. To take this unavoidable mode coupling into account one may average the Raman terms of the LP11a and LP11b in Eq. (9) by assuming that through a small piece of fiber, the propagating light has spent approximately equal time in both modes [16]. Such an averaging is not necessary in our modeling since an ensemble that approximately represents the whole LP11 mode space (i.e. all combinations of LP11a and LP11b) is propagated through the fiber; thus, the average of the ensemble represents the same value that comes out of the averaged Raman propagation equations of Ref. [16].

B. Two Mode-Group System

Several experiments of transmitting data through few-mode fibers have been conducted [6], [17], [25] and distributed Raman amplification has been used to mitigate fiber attenuation [4]. Based on Eq. (9) we derive conditions for achieving equal modal gain in a system of two mode groups, LP01 and LP11; the latter mode group consists of two modes, LP11a and LP11b. As stated above, only one state of polarization is considered. If a signal s at a single wavelength is amplified by a pump p at a single wavelength both occupying the three spatial mode in a loss-less fiber, then in the undepleted pump regime, the solutions for the signal modes are all on the form

$$P_{\text{s}}^{(\mu)}(z) = P_{\text{s}}^{(\mu)}(0) \text{e}^{G^{(\mu)} z}, \quad (10)$$

where

$$G^{(\mu)} = \frac{2\omega_s n_2 f_R}{c} \text{Im}\{\tilde{h}_R(\Omega_{\text{ps}}\} \sum_\nu f^{(\mu,\nu)} P_{\text{p}}^{(\nu)} \quad (11)$$

and $P_{\text{p}}^{(\mu)}$ is the constant power of pump mode μ. Equating the gain of the LP11a and LP11b modes and using that $f^{(11a,11a)} = f^{(11b,11b)} \equiv f^{(11,11)}$ one gets

$$\left(f^{(11,11)} - f^{(11a,11b)}\right)\left(P_{\text{p}}^{(11a)} - P_{\text{p}}^{(11a)}\right) = 0, \quad (12)$$

from which it is immediately concluded that $P_{\text{p}}^{(11a)} = P_{\text{p}}^{(11b)}$ since $f^{(11,11)}$ and $f^{(11a,11b)}$ are rarely similar. Then equating the gains of the LP01 and LP11a modes, the condition for equal gain in all three modes becomes

$$P_{\text{p}}^{(11a)} = \frac{f^{(01,01)} - f^{(01,11)}}{f^{(11,11)} + f^{(11a,11b)} - 2f^{(01,11)}} P_{\text{p}}^{(01)} \quad (13)$$

where $f^{(01,11a)} = f^{(01,11b)} \equiv f^{(01,11)}$ was used. It follows from this results that $f^{(11,11)} + f^{(11a,11b)} > 2f^{(01,11)}$ is a requirement for equal gain to be possible, since $f^{(01,01)} > f^{(01,11)}$ always applies in circular symmetric fibers; if this condition is not met in a given fiber, equal gain among LP11a and LP11b is still achievable for $P_{\text{p}}^{(11a)} = P_{\text{p}}^{(11a)}$.

In a situation where the equal gain condition is not met by the fiber but equal gain among LP01 and LP11a(b) is desired, the power of LP11b(a) must be zero, and the power of LP11a(b) becomes

$$P_{\text{p}}^{(11a)} = \frac{f^{(01,01)} - f^{(01,11)}}{f^{(11,11)} - f^{(01,11)}} P_{\text{p}}^{(01)}. \quad (14)$$

A transparent transmission line, i.e. each of the output signal modal powers equal each of the input signal modal powers, is achieved by using Eq. (13), equating the LP01 signal gain and the total loss, and assuming that all pump and signal modes have the same attenuation coefficient, α_{p} and α_{s}, respectively. The LP01 pump input power is then found to be

$$P_{\text{p}}^{(01)} = \frac{\alpha_{\text{s}} L}{\bar{\gamma} L_{\text{eff}}}, \quad (15)$$

where L is the fiber length, $L_{\text{eff}} = [1 - \exp(-\alpha_{\text{p}} L)]/\alpha_{\text{p}}$ is the effective fiber length, and

$$\bar{\gamma} = \frac{2n_2\omega_{\text{s}}}{c}\left[f^{(01,01)} + \frac{2\left(f^{(01,01)} - f^{(01,11)}\right) f^{(01,11)}}{f^{(11,11)} + f^{(11a,11b)} + 2f^{(01,11)}}\right] \times f_R \text{Im}\{\tilde{h}_R(\Omega_{\text{ps}}\}. \quad (16)$$

The two mode-group system described here is investigated numerically by solving the set of equations (9) using a 4th order Runge-Kutta algorithm through an $L = 100$ km fiber

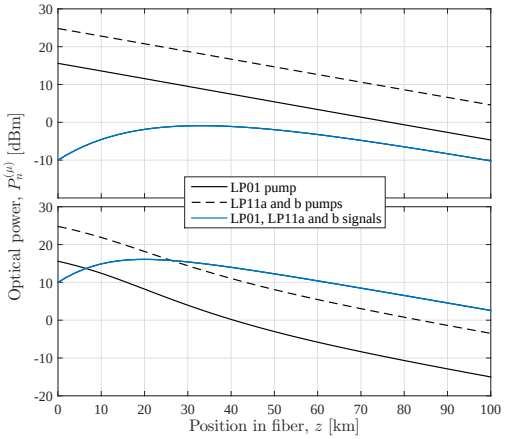

Fig. 1. Power evolution through fiber operated in the linear gain regime (top) and in the depleted pump regime (bottom); the curves for the LP11a and b pumps, and the curves for the LP01, LP11a and b signals, repsectively, are indistinguishable in the plot.

in 50 steps (including more steps only changed the outcome by a negligible margin) with a nonlinear index $n_2 = 2.6 \times 10^{-20}$ m^2/W, an LP01 effective area $A_{\text{eff}}^{(01)} = 80$ μm^2, realistic nonlinear mode overlaps $f^{(01,11)} = 0.5f^{(01,01)}$, $f^{(11,11)} = 0.76f^{(01,01)}$, $f^{(11a,11b)} = 0.3f^{(01,01)}$ [26], common attenuation coefficients $\alpha_{\text{p}} = \alpha_{\text{p}} = 0.2$ dB/km, pump and signal wavelengths $\lambda_{\text{p}} = 1450$ nm and $\lambda_{\text{s}} = 1550$ nm, and LP01 and LP11a and b pump powers from Eq. (15) and (14), respectively.

The result is shown in Fig.1: the top plot shows the power evolution of all six fields in the undepleted pump regime; all the signal modes are indistinguishable in the plot as a consequence of the equal gain condition calculated above, and the LP11a and LP11b pumps are indistinguishable because they follow identical equations when their attenuation coefficients and all signal powers are equal. In the top plot, a signal input power of $P_{\text{s}}^{(01)} = P_{\text{s}}^{(11a)} = P_{\text{s}}^{(11b)} = P_{\text{s,in}} = -10$ dBm was used and since the pumps remain essentially undepleted by the signals, the transmission line is transparent as dictated by Eq. (15). In the bottom plot, the signals were initiated with a power of $P_{\text{s,in}} = 10$ dBm and the pumps are immediately affected and start to deplete; consequently, not enough energy remain in the pumps to compensate for the attenuation in the rest of the fiber, and hence the signals arrive with almost 10 dB lower power than at input.

C. Random Linear Mode Coupling

Mode coupling has been modeled in different ways [19], [27], [28] but the mechanisms behind mode coupling are presently not well understood [29]. Therefore, it is difficult to define meaningful properties of couplings taking place at specific positions in the fiber. In practice one needs to measure the output modal contents—e.g. by S^2 measurements [30]—with little knowledge about where in the fiber the coupling has

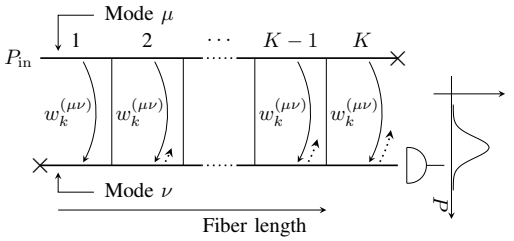

Fig. 2. Illustration of the random linear mode coupling model: the two horizontal lines represent two fiber modes in which the fields couple with mean rate $w_k^{(\mu\nu)}$ in each section. The plot is a sketch of the power probability density in mode ν given the overall coupling degree $w^{(\mu\nu)}$ and standard deviation $\sigma^{(\mu\nu)}$. The dashed arrows indicate possible backcoupling, which is neglected in the model.

taken place. Hence, a numerical investigation of the statistical properties of the mode coupling must treat the fiber as a series of identical sections. Since the pump must be assumed to take many different modal combinations through the fiber—due to both deterministic and random mode coupling—and an amplified signal experiences many of these, we assume that all mode coupling in the pump can be viewed as random. Thus, we model mode coupling in the pump as a transfer of a random proportion of the total mode power to other modes; we consider the weak coupling regime so it is implied that only a fraction of the light in a given mode has changed to another mode through the whole fiber. The fiber sections are assumed uncorrelated, which implies that the correlation length of the perturbations that are responsible for mode coupling is much shorter than the length of one section. By choosing a suitable coupling probability distribution, the parameters of the individual, identical sections are calculated directly from the measurable output power statistics of the modes that were coupled to. Hence, the degree of mode coupling between two modes is a stochastic variable but it is calculated through a well-defined mean and variance. Fig.2

The model of RLMC is illustrated in Fig. 1: light is initiated only in mode μ and in each step a random proportion with mean value $w_k^{(\mu\nu)}$ of the power in mode μ couples to mode ν. The random proportion of power that couples must be chosen from a probability distribution that has support on the continuous interval $[0, 1]$; the Beta distribution is often used to model random proportions [31],

$$\text{Beta}(x|a,b) = \frac{x^{a-1}(1-x)^{b-1}}{B(a,b)}, \tag{17}$$

where $B(a, b)$ is a normalization constant. The stochastic variable x is the random proportion of power that changes mode, and it has the properties

$$\langle x \rangle = \frac{a}{a+b} \equiv w_k^{(\mu\nu)} \tag{18}$$

$$\langle (x - \langle x \rangle)^2 \rangle = \frac{ab}{(a+b)^2(a+b+1)} \equiv {\sigma_k^{(\mu\nu)}}^2, \tag{19}$$

where $w_k^{(\mu\nu)}$ and $\sigma_k^{(\mu\nu)}$ are the mean value and the standard deviation of the random coupling in the identical sections, and

a and b are positive shape parameters. At the output of the fiber, the power mean value and standard variation in mode ν can be measured, and relative to the mean input power we call these the overall coupling degree $w^{(\mu\nu)}$ and overall standard deviation $\sigma^{(\mu\nu)}$, where superscript $(\mu\nu)$ denotes that the parameter belongs to coupling between mode μ and ν. This procedure may be repeated for any number of modes. The connection between $w^{(\mu\nu)}$, $\sigma^{(\mu\nu)}$, $w_k^{(\mu\nu)}$, and $\sigma_k^{(\mu\nu)}$ is simple because the output in mode ν is a sum of a large number of independent, identically distributed random numbers so due to the Central Limit Theorem, the output is normally distributed and the mean value and variance are the sums of the mean values and variances of each section, so

$$w_k^{(\mu\nu)} = w^{(\mu\nu)}/K \tag{20}$$

$$\sigma_k^{(\mu\nu)} = \sigma^{(\mu\nu)}/\sqrt{K}, \tag{21}$$

where K is the number of sections, which is a numerical parameter that must be assumed to be large, e.g equal to the number of steps in the numerical algorithm for solving the set of equations (9). In the connections (20) and (21), it was assumed that no significant amount of light couples back to the initial mode as shown by the dashed arrows in Fig. 1 that points from mode ν to mode ν. From simulations not shown here, we find that this approximation is fair as long as $w^{(\mu\nu)} < 0.1$, which underlines that the simple interpretation of $w^{(\mu\nu)}$ and $\sigma^{(\mu\nu)}$ is valid only in the weak coupling regime. The linearity of the random mode couplings implies that the model is valid in the depleted pump regime as well as in the undepleted pump regime.

III. Impacts of Pump Mode Coupling and Pump Depletion

To quantify the amount of noise that mode coupling in the pump adds during amplification, the input signal must be initiated with a well defined signal-to-noise ratio. Lasers can produce good approximations to coherent states so a straightforward approach to generating an input ensemble is defining a mean input number of photons, $\bar{n}_n^{(\mu)} = P_n^{(\mu)}/(\hbar\omega_n B_0)$, in every mode where $\hbar$ is Planck's constant and $B_0 = 12$ GHz (0.1 nm) is the frequency bandwidth. The number of photons in a coherent state follows a Poisson distribution [32], so an input ensemble of fields in every mode of both pump and signal is generated by calculating the mean number of photons, pull out 20×10^3 numbers from a Poisson distribution with $\bar{n}_n^{(\mu)}$ as the mean number, and then convert every element back to optical power units.

The signal-to-noise ratio, SNR, is defined at every point in the fiber as

$$\mathrm{SNR}_n^{(\mu)} = \frac{\langle P_n^{(\mu)} \rangle^2}{\mathrm{Var}\left(P_n^{(\mu)}\right)} \tag{22}$$

and the pump mode coupling-induced noise figure (NF) is defined as the relative change in SNR, $\mathrm{NF} = \mathrm{SNR}_{\mathrm{input}}/\mathrm{SNR}_{\mathrm{output}}$. In the two mode-group case already considered about, six ensembles are propagated in parallel through Eqs. (9) and mode coupling as of the previous section is applied to every element in each ensemble.

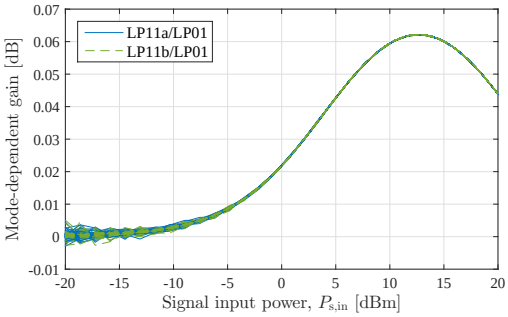

Fig. 3. lP11a (blue solid) and LP11b (green dashed) relative to LP01 mode-dependent signal gain vs. signal input power, $P_{\mathrm{s,in}}$; the many curves in each mode represents a range of different $w^{(11a,11b)}$ values from -40 dB to -10 dB.

A. Mode-Dependent Gain

Recent works have focused on the possibilities of achieving mode equalized gain [4], [9], [33] using theory similar to what we presented above. However, it remains unclear what the impacts of pump depletion and pump mode couplings are on the NF and the prospects of achieving mode-equalized gain in Raman fiber amplifiers, which is what we investigate in these two sections: we conduct simulations both with and without inter-mode-group mode coupling such that firstly only the LP11a and LP11b in the pump couples (intra-mode-group mode coupling); secondly, also the LP01 mode couple to the LP11 mode-group (inter-mode-group mode coupling).

In the model of weak random mode coupling, all modes need not couple to the same overall degree, and indeed intra-mode-group mode couplings in the LP11 mode-group are expected to be stronger than inter-mode-group mode couplings between LP01 and LP11 mode-groups. We start by assuming that inter-mode-group mode coupling is negligible and do simulations in the same fashion as in Fig.1; both the signal input power and the degree of intra-mode-group mode coupling, $w^{(11a,11b)}$, are varied; the pump mode powers are again chosen to satisfy equal modal gain in all signal modes and to make the transmission line transparent.

Fig.3 shows the the mode-dependent gain (MDG), i.e. the signal gain of LP11a (blue solid) and LP11b (green dashed) relative to the gain of LP01, respectively. The many curves of each mode represent a range of different $w^{(11a,11b)}$ values from -40 dB to -10 dB; no significant difference can be observed in this interval. In the undepleted gain regime, the mode dependent gain is fluctuation around zero as expected from the equal modal gain conditions; in the depleted pump regime ($P_{\mathrm{s,in}} > 5$ dBm), an increasing mode-dependent gain is observed but it is still somewhat smaller than the lowest MDG of few-mode Raman amplifiers measured in the undepleted pump regime toady of 0.25 dB per 10 dB gain [34]. Our analysis shows that intra-mode-group mode coupling in the pump plays a minor role for mode dependent gain even in the depleted pump regime.

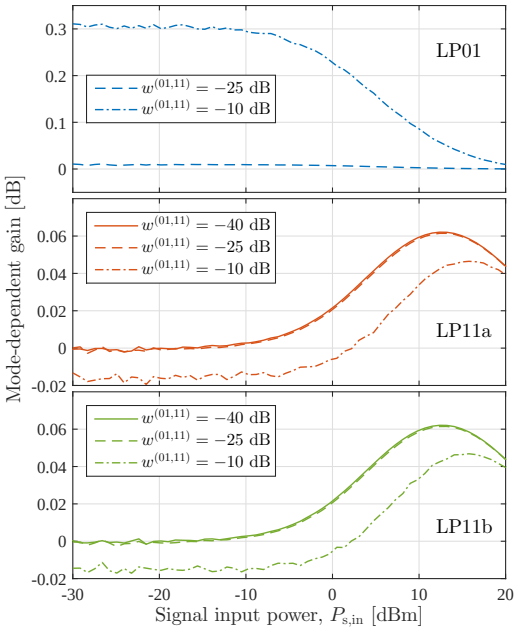

Fig. 4. Mode-dependent gain vs. signal input power $P_{\mathrm{s,in}}$ in modes LP01 (top), LP11a (middle), and LP11b (bottom) for different degrees of inter-mode-group mode coupling $w^{(01,11)}$ relative to the LP01 gain at $w^{(01,11)} = -40$ dB.

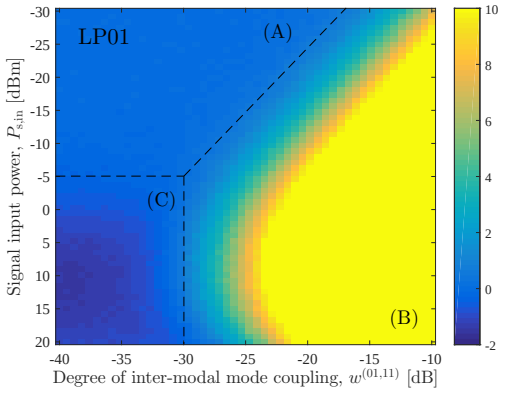

Fig. 5. Signal LP01 NF vs. overall degree of inter-modal mode coupling w_2 and input signal power $P_{\mathrm{s,in}}$ (undepleted pump regime top, and depleted pump regime bottom). Three separate regions (A)–(C) with different characteristics are identified; see the text.

Next, inter-mode-group mode coupling is included by setting the degree of inter-mode-group mode coupling, $w^{(01,11)}$, non-zero. The degree of intra-mode-group mode coupling $w^{(11a,11b)}$ is kept at the maximum value of -10 dB since in all cases the intra-mode-group couplings must be stronger than the inter-mode-group couplings. Fig.4 shows the MDG of all three signal modes at $w^{(01,11)} = -40$ dB, $w^{(01,11)} = -25$ dB, and $w^{(01,11)} = -10$ dB relative to the LP01 signal gain at $w^{(01,11)} = -40$ dB, which is so low that all behavior is expected to be the same as if it was not present.

Indeed, the MDG curves of LP11a and LP11b (middle and bottom plots) at $w^{(01,11)} = -40$ dB are very similar to those in Fig.3; the same are those at $w^{(01,11)} = -25$, which means that an inter-mode-group mode coupling degree of -25 dB in the pump is not detectable in the LP11 mode-group in our analysis even in pump depletion. For the LP01 mode (top plot), however, a slight increase in gain relative to the $w^{(01,11)} = -40$ case is observed; at $w^{(01,11)} = -10$, the increase in MDG is 0.3 dB, which cf. [34] might be detectable experimentally. The reason for this increase in gain for larger values of $w^{(01,11)}$ is that light is transferred between the to mode groups; indeed, light couples between the LP01 mode and the LP11 mode group to the same degree in our model but the LP11 pumps are initiated much stronger than the LP01 pump, as is evident in Fig.1, to obey the equal modal gain condition. Hence, effectively light is coupled from the LP11 mode group to the LP01 mode and that causes the gain in the LP01 signal to increase. That is also the reason that the LP11a and LP11b MDG have decreased in Fig.4 for increased values of $w^{(01,11)}$. As the pump depletes, however, these tendencies disappear because the pumps are saturated before the mode coupling effectively takes place.

The effects described in Figs. 3 and 4 are clearly visible in the plots but are of very modest magnitude. Hence our analysis has shown that weak linear mode coupling in the pump (coupling degrees between modes up to -10 dB) has only a minor impact on the conditions for equal modal gain in distributed Raman amplifiers even in the depleted pump regime.

B. Pump Mode Coupling Induced Noise Figure

The noise properties of few-mode Raman fiber amplifiers (FM-RFA) are important for their potential in future optical communication systems; one of the great advantages of backward-pumped single-mode RFA is their superior noise properties to EDFAs [35]. If FM-RFA are to be used in communication systems, the presence of mode coupling should not introduce too much excess noise. In this paper, we only model forward pumped FM-RFA due to the difficulties of applying statistical models in the backward pumped configuration.

The NFs of all three signal modes are evaluated using Eq. (22); if inter-mode-group mode coupling is neglected, i.e. $w^{(01,11)} = 0$ as in Fig.3, no mode coupling induced NF for any $(w^{(11a,11b)}$ values are found in the undepleted pump regime (the depleted pump regime is discussed below). The reason is that the LP11 pumps were initiated with the same power according to the equal gain condition so therefore no light is effectively transferred between the two modes; however the randomness of the mode coupling induces an increased power variance in the pumps which consequently increases the variance in the signal and hence the NF but this effect is not strong enough to matter in the weak coupling regime. If

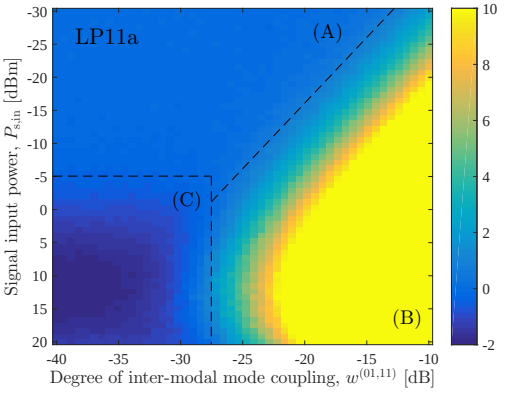

Fig. 6. Signal LP11a NF vs. overall degree of inter-modal mode coupling w_2 and input signal power $P_{s,in}$ (undepleted pump regime top, and depleted pump regime bottom). Three separate regions (A)–(C) with different characteristics are identified; regions (A) and (C) are larger than those for LP01 in Fig.4.

the pumps are initiated with asymmetric power, a larger NF is indeed induced as verified in simulations not shown here.

Including inter-mode-group mode coupling, the induced NF of the LP01 and LP11a signals are shown in Figs. 5 and 6 as functions of signal input power and the degree of inter-mode-group mode coupling $w^{(01,11)}$; the data are extracted from the same simulation that produced Fig.4; the color bar shows the NF in dB. The NF for LP11b is indistinguishable from that of LP11a so it is omitted here.

In both figures, the NF in $(P_{s,in}), w^{(01,11)})$ space can be divided in three regions with different characteristics, A, B, and C. Region A is the regime that corresponds to usual single-mode operation; the pump is undepleted and mode coupling is so low that the modes approximate separate single mode channels (intra-mode-group mode coupling is still $w^{11a,11b} = -10$ dB). In this regime, the mode coupling induced NF is predicted to be zero; the mode coupling is simply too small to matter. In region B, the NF increases to more than 10 dB due to higher inter-mode-group mode coupling; the line between regions A and B shows how much input power in the signals that can be tolerated under a certain degree of mode coupling (given the input powers used in our simulation). The line has a positive slope in $(P_{s,in}), w^{(01,11)})$ space because the NF becomes more sensitive to mode coupling in the depleted pump regime.

Region C, in which inter-mode-group mode coupling is very small and the amplifier is depleted, contains negative NF values. We already established above that intra-mode-group mode couplings did not induce any NF in the undepleted pump regime but as the pump depletes the NF becomes negative due to a decrease in the signal power variance. This decrease is a simple consequence of the nature of Raman scattering; when the pump is being depleted, the variance of the signal goes asymptotically towards the variance of the pump power at input because energy only flows from one component to the other. This effect is also predicted [36] and measured [37]–[39] in fiber optical parametric amplifiers operated in the depleted pump regime. The line between regions B and C denote the point where inter-mode-group mode coupling becomes so significant that the intensity regenerative property of operating the pump in depletion is destroyed.

The importance of the existence of low the NF region A described here should be seen in light of the fact that the model of the pump fluctuations assumed that all pump mode couplings were completely random. Thus, even the low NF regions represent a worst case scenario of addition of excess noise from pump fluctuations in the weak coupling regime.

It should be noted that we observe that regions A and C are slightly larger in Fig.6 for the LP11 mode group than in Fig.5 for the LP01 mode, which indicates that signals transmitted in LP11a and LP11b modes are more resistant to the effects of pump mode coupling.

IV. Conclusion

In this paper, we analyzed the impacts of linear mode coupling in the pump of few-moded distributed Raman fiber amplifiers. After deriving basic propagation equations and conditions for equal modal gain and equal input and output signal power, a numerical model of weak random mode coupling was presented. This model was used to analysis the impacts of mode coupling in the pump of a two-mode-group Raman fiber amplifier...

References

[1] N. Bai, E. Ip, Y.-k. Huang, E. Mateo, F. Yaman, M.-j. Li, S. Bickham, S. Ten, J. Liñares, C. Montero, V. Moreno, X. Prieto, V. Tse, K. M. Chung, A. Pak, T. Lau, H.-y. Tam, C. Lu, Y. Luo, G.-d. Peng, G. Li, T. Wang, N. E. C. L. America, and I. Way, "Mode-division multiplexed transmission with inline few-mode fiber amplifier," *Opt. Express*, vol. 20, no. 3, pp. 2668–2680, 2012.

[2] K. Okamoto, *Fundamentals of Opticals Waveguides*, 2nd ed. Elsevier, 2006.

[3] V. A. J. M. Sleiffer, Y. Jung, V. Veljanovski, R. G. H. V. Uden, M. Kuschnerov, B. Inan, L. G. Nielsen, Y. Sun, D. J. Richardson, S. U. Alam, F. Poletti, J. K. Sahu, A. Dhar, A. M. J. Koonen, B. Corbett, R. Winfield, and A. D. Ellis, "Multiplexed DP-16QAM transmission with inline MM-EDFA," *Opt. Express*, vol. 20, no. 26, pp. B428–B438, 2012.

[4] R. Ryf, A. Sierra, R.-J. Essiambre, S. Randel, A. Gnauck, C. A. Bolle, M. Esmaeelpour, P. J. Winzer, R. Delbue, P. Pupalaikis, A. Sureka, D. Peckham, A. McCurdy, and R. Lingle, "Mode-Equalized Distributed Raman Amplification in 137-km Few-Mode Fiber," in *37th Eur. Conf. Expo. Opt. Commun.* OSA, 2011, p. Th.13.K.5.

[5] K. Rottwitt and A. J. Stentz, "Raman Amplification in Lightwave Communication Systems," in *Opt. Fiber Telecommun. IV A Components*, I. Kaminow and T. Li, Eds. Academic, 2002, ch. 5, pp. 213–257.

[6] R. Ryf, M. A. Mestre, S. Randel, S. Member, C. Schmidt, A. H. Gnauck, R.-J. Essiambre, P. J. Winzer, R. Delbue, P. Pupalaikis, A. Sureka, Y. Sun, X. Jiang, D. W. Peckham, A. Mccurdy, and R. Lingle, "Mode-Multiplexed Transmission Over a 209-km DGD-Compensated Hybrid Few-Mode Fiber Span," *IEEE Photonics Technol. Lett.*, vol. 24, no. 21, pp. 1965–1968, 2012.

[7] Q. Kang, E. Lim, Y. Jun, X. Jin, F. P. Payne, S. Alam, and D. J. Richardson, "Gain Equalization of a Six-Mode-Group Ring Core Multimode EDFA," in *Eur. Conf. Exhib. Opt. Commun.*, 2014.

[8] R. Ryf, R.-J. Essiambre, J. von Hoyningen-Huene, and P. J. Winzer, "Analysis of Mode-Dependent Gain in Raman Amplified Few-Mode Fiber," *OFC Tech. Dig.*, 2012.

[9] J. Zhou, "An analytical approach for gain optimization in multimode fiber Raman amplifiers," *Opt. Express*, vol. 22, no. 18, p. 21393, 2014.

[10] R. Ryf, S. Randel, A. H. Gnauck, C. Bolle, A. Sierra, S. Mumtaz, M. Esmaeelpour, E. C. Burrows, R.-J. Essiambre, P. J. Winzer, D. W. Peckham, A. H. McCurdy, and R. Lingle, "Mode-division multiplexing over 96 km of few-mode fiber using coherent 66 MIMO processing," *J. Light. Technol.*, vol. 30, no. 4, pp. 521–531, 2012.

[11] L. Grüner-nielsen, Y. Sun, J. W. Nicholson, D. Jakobsen, K. G. Jespersen, R. Lingle, and B. Pálsdóttir, "Few Mode Transmission Fiber With Low DGD, Low Mode Coupling, and Low Loss," *J. Light. Technol.*, vol. 30, no. 23, pp. 3693–3698, 2012.
[12] P. J. Winzer, A. H. Gnauck, A. Konczykowska, F. Jorge, and J.-Y. Dupuy, "Penalties from in-band crosstalk for advanced optical modulation formats," in *37th European Conference and Exposition on Optical Communications*. Optical Society of America, 2011, p. Tu.5.B.7.
[13] B. Ung, P. Vaity, L. Wang, Y. Messaddeq, L. a. Rusch, and S. LaRochelle, "Few-mode fiber with inverse-parabolic graded-index profile for transmission of OAM-carrying modes," *Opt. Express*, vol. 22, no. 15, p. 18044, 2014.
[14] K.-P. Ho and J. M. Kahn, "Mode Coupling and its Impact on Spatially Multiplexed Systems," in *Opt. Fiber Telecommun. Vol. VIB, Sixth Ed. Syst. Networks*, 6th ed. Academic, 2013, ch. 11.
[15] K. Jespersen, Z. Li, B. Pálsdóttir, F. Poletti, and J. W. Nicholson, "Measuring Distributed Mode Scattering in Long , Few- Moded Fibers," in *OFC Tech. Dig.*, 2012, p. OTh31.4.
[16] C. Antonelli, A. Mecozzi, and M. Shtaif, "Raman amplification in multimode fibers with random mode coupling." *Opt. Lett.*, vol. 38, no. 8, pp. 1188–90, 2013.
[17] R. Ryf, S. Randel, A. H. Gnauck, C. Bolle, A. Sierra, S. Mumtaz, M. Esmaeelpour, E. C. Burrows, R.-J. Essiambre, P. J. Winzer, D. W. Peckham, A. H. McCurdy, and R. Lingle, "Mode-Division Multiplexing Over 96 km of Few-Mode Fiber Using Coherent 6×6 MIMO Processing," *J. Light. Technol.*, vol. 30, no. 4, pp. 521–531, 2012.
[18] K. P. Ho and J. M. Kahn, "Mode-dependent loss and gain : statistics and effect on mode-division multiplexing," *Opt. Express*, vol. 19, no. 17, pp. 16 612–16 635, 2011.
[19] ——, "Statistics of group delays in multimode fiber with strong mode coupling," *J. Light. Technol.*, vol. 29, no. 21, pp. 3119–3128, 2011.
[20] ——, "Linear Propagation Effects in Mode-Division Multiplexing Systems," *J. Light. Technol.*, vol. 32, no. 4, pp. 614–628, Feb. 2014.
[21] M. Kolesik and J. Moloney, "Nonlinear optical pulse propagation simulation: From Maxwells to unidirectional equations," *Phys. Rev. E*, vol. 70, no. 3, p. 036604, Sep. 2004.
[22] F. Poletti and P. Horak, "Description of ultrashort pulse propagation in multimode optical fibers," *J. Opt. Soc. Am. B*, vol. 25, no. 10, p. 1645, 2008.
[23] D. Hollenbeck and C. D. Cantrell, "Multiple-vibrational-mode model for fiber-optic Raman gain spectrum and response function," *J. Opt. Soc. Am. B*, vol. 19, no. 12, p. 2886, Dec. 2002.
[24] C. Headley and G. P. Agrawal, "Unified description of ultrafast stimulated Raman scattering in optical fibers," *J. Opt. Soc. Am. B*, vol. 13, no. 10, p. 2170, 1996.
[25] N. K. Fontaine, R. Ryf, M. a. Mestre, B. Guan, X. Palou, S. Randel, Y. Sun, L. Gruner-Nielsen, R. V. Jensen, and R. Lingle, "Characterization of Space-Division Multiplexing Systems using a Swept-Wavelength Interferometer," in *Opt. Fiber Commun. Conf. Fiber Opt. Eng. Conf. 2013*, no. c. OSA, 2013, p. OW1K.2.
[26] Y. Xiao, R.-J. Essiambre, M. Desgroseilliers, A. M. Tulino, R. Ryf, S. Mumtaz, and G. P. Agrawal, "Theory of intermodal four-wave mixing with random linear mode coupling in few-mode fibers," *Opt. Express*, vol. 22, no. 26, pp. 32 039–32 059, 2014.
[27] A. Mecozzi, C. Antonelli, and M. Shtaif, "Nonlinear propagation in multi-mode fibers in the strong coupling regime," *Opt. Express*, vol. 20, no. 11, p. 11673, 2012.
[28] C. Antonelli, A. Mecozzi, M. Shtaif, and P. J. Winzer, "Random coupling between groups of degenerate fiber modes in mode multiplexed transmission," *Opt. Express*, vol. 21, no. 8, p. 9484, 2013.
[29] L. Palmieri, "Coupling mechanism in multimode fibers," in *Proc. SPIE*, vol. 9009, Dec. 2013, p. 90090G.
[30] J. W. Nicholson, A. D. Yablon, S. Ramachandran, and S. Ghalmi, "Spatially and spectrally resolved imaging of modal content in large-mode-area fibers," *Opt. Express*, vol. 16, no. 10, pp. 7233–7243, 2008.
[31] L. Blanco Castañeda, V. Arunachalam, and S. Dharmaraja, "Some Continuous Distributions," in *Introd. to Probab. Stoch. Process. with Appl.* Wiley, 2012, ch. 4, pp. 145–189.
[32] C. C. Gerry and P. L. Knight, *Introductory Quantum Optics*. Cambridge, 2005.
[33] Y. Weng, T. Wang, and Z. Pan, "Optimization of Mode-Dependent Gain Efficiency based on Intermodal Raman Scattering for Few-Mode Distributed Raman Amplifier," in *Conf. Lasers Electro-Optics*. OSA, 2016, p. SW1P.5.
[34] E. N. Christensen, J. G. Koefoed, S. M. M. Friis, M. A. Usuga, and K. Rottwitt, "Experimental characterization of Raman overlaps between mode-groups," *Submitted to Scientific Reports*, June 2016.
[35] M. N. Islam, "Raman Amplifiers for Telecommunications," *IEEE J. Sel. Top. Quantum Electron.*, vol. 8, no. 3, pp. 548–559, 2002.
[36] S. M. M. Friis, K. Rottwitt, and C. J. McKinstrie, "Raman and loss induced quantum noise in depleted fiber optical parametric amplifiers," *Opt. Express*, vol. 21, no. 24, p. 29320, Nov. 2013.
[37] K. Croussore and G. Li, "Phase and Amplitude Regeneration of Differential Phase-Shift Keyed Signals Using Phase-Sensitive Amplification," *IEEE J. Sel. Top. Quantum Electron.*, vol. 14, no. 3, pp. 648–658, 2008.
[38] M. Matsumoto, "Fiber-Based All-Optical Signal Regeneration," *IEEE J. Sel. Top. Quantum Electron.*, vol. 18, no. 2, pp. 738–752, 2012.
[39] M. Sköld, J. Yang, H. Sunnerud, M. Karlsson, S. Oda, and P. A. Andrekson, "Constellation diagram analysis of DPSK signal regeneration in a saturated parametric amplifier," *Opt. Express*, vol. 16, no. 9, p. 5974, 2008.

Søren Michael Mørk Friis received the B.Sc. and M.Sc. in engineering from Technical University of Denmark in 2010 and 2013, respectively. He is now employed as a PhD student at the Department of Photonics Engineering at Technical University of Denmark where he studies nonlinear amplifiers and frequency converters in single- and few-moded fibers.

Karsten Rottwitt was born in Odense, Denmark in 1965. He received his M.Sc. and Ph.D. degree in soliton propagation through optical fiber amplifiers from the Technical University of Denmark (DTU) in 1990 and 1993, respectively. After two years as a Post Doc. at DTU, he continued his career at AT&T and Lucent Technologies/Bell Labs Innovations from 1995 to 2000. In 2000, he got a position at the Physics department of the University of Copenhagen, Denmark. Since 2002, he has been at the department of Photonics Engineering at the Technical University of Denmark (DTU Fotonik) where he is now a full professor. Karsten Rottwitt has authored or co-authored more than 150 scientific publications within the field of fiber optics. He holds 11 patents. Prof. Karsten Rottwitt is a member of OSA. He has served as reviewer for several journals and international conferences and is currently member of the board of editors of Optica.

Bibliography

[1] M. Castells, "The Impact of the Internet on Society: A Global Perspective," *BBVAOpenMind*, sep 2014.

[2] D. J. Richardson, "Filling the Light Pipe," *Science*, vol. 330, no. 6002, pp. 327–328, 2010.

[3] A. D. Ellis, J. Zhao, and D. Cotter, "Approaching the Non-Linear Shannon Limit," *J. Light. Technol.*, vol. 28, pp. 423–433, feb 2010.

[4] A. Chraplyvy, "Plenary paper: The coming capacity crunch," in *2009 35th Eur. Conf. Opt. Commun.*, p. 8007, 2009.

[5] A. D. Ellis, N. M. Suibhne, D. Saad, and D. N. Payne, "Communication networks beyond the capacity crunch," *Philos. Trans. R. Soc. A Math. Phys. Eng. Sci.*, vol. 374, no. 2062, p. 20150191, 2016.

[6] S. Smirnov, J. Ania-Castanon, T. Ellingham, S. Kobtsev, S. Kukarin, and S. Turitsyn, "Optical spectral broadening and supercontinuum generation in telecom applications," *Opt. Fiber Technol.*, vol. 12, no. 2, pp. 122–147, 2006.

[7] J. Pfeifle, V. Brasch, M. Lauermann, Y. Yu, D. Wegner, T. Herr, K. Hartinger, P. Schindler, J. Li, D. Hillerkuss, R. Schmogrow, C. Weimann, R. Holzwarth, W. Freude, J. Leuthold, T. J. Kippenberg, and C. Koos, "Coherent terabit communications with microresonator Kerr frequency combs," *Nat. Photonics*, vol. 8, no. 5, pp. 375–380, 2014.

[8] P. Delfyett, S. Gee, Myoung-Taek Choi, H. Izadpanah, Wangkuen Lee, S. Ozharar, F. Quinlan, and T. Yilmaz, "Optical frequency combs from semiconductor lasers and applications in ultrawideband signal processing and communications," *J. Light. Technol.*, vol. 24, no. 7, pp. 2701–2719, 2006.

[9] P. J. Winzer and R.-J. Essiambre, "Advanced Optical Modulation Formats," *Proc. IEEE*, vol. 94, no. 5, pp. 952–985, 2006.

[10] P. J. Winzer, "High-Spectral-Efficiency Optical Modulation Formats," *J. Light. Technol.*, vol. 30, no. 24, pp. 3824–3835, 2012.

[11] G. P. Agrawal, *Fiber-Optic Communication Systems*. Wiley Series in Microwave and Optical Engineering, New York, USA: John Wiley & Sons, Inc., 2002.

[12] B. Ramamurthy and B. Mukherjee, "Wavelength conversion in WDM networking," *IEEE J. Sel. Areas Commun.*, vol. 16, no. 7, pp. 1061–1073, 1998.

[13] J. Elmirghani and H. Mouftah, "All-optical wavelength conversion: technologies and applications in DWDM networks," *IEEE Commun. Mag.*, vol. 38, no. 3, pp. 86–92, 2000.

[14] Z. Pan, C. Yu, and A. E. Willner, "Optical performance monitoring for the next generation optical communication networks," *Opt. Fiber Technol.*, vol. 16, no. 1, pp. 20–45, 2010.

[15] C. Giles and E. Desurvire, "Modeling erbium-doped fiber amplifiers," *J. Light. Technol.*, vol. 9, no. 2, pp. 271–283, 1991.

[16] M. Islam, "Raman amplifiers for telecommunications," *IEEE J. Sel. Top. Quantum Electron.*, vol. 8, pp. 548–559, may 2002.

[17] J. Hansryd, P. Andrekson, M. Westlund, Jie Li, and P.-O. Hedekvist, "Fiber-based optical parametric amplifiers and their applications," *IEEE J. Sel. Top. Quantum Electron.*, vol. 8, pp. 506–520, may 2002.

[18] S. Radic, "Parametric amplification and processing in optical fibers," *Laser Photonics Rev.*, vol. 2, pp. 498–513, dec 2008.

[19] M. E. Marhic, P. A. Andrekson, P. Petropoulos, S. Radic, C. Peucheret, and M. Jazayerifar, "Fiber optical parametric amplifiers in optical communication systems," *Laser Photon. Rev.*, vol. 9, pp. 50–74, jan 2015.

[20] M. E. Marhic, F. S. Yang, L. G. Kazovsky, and Y. Park, "Broadband fiber-optical parametric amplifiers and wavelength converters with low-ripple Chebyshev gain spectra," *Opt. Lett.*, vol. 21, p. 1354, sep 1996.

[21] S. Radic, C. J. McKinstrie, A. R. Chraplyvy, G. Raybon, J. C. Centanni, C. G. Jorgensen, K. Brar, and C. Headley, "New class of continuous wave parametric amplifiers," in *Optical Fiber Communication Conference and Exhibit, 2002. OFC 2002*, pp. FB5–1–FB5–3, Mar 2002.

[22] F. S. Yang, M. C. Ho, M. E. Marhic, and L. G. Kazovsky, "Demonstration of two-pump fiber optical parametric amplification," in *Lasers and Electro-Optics Society Annual Meeting, 1997. LEOS '97 10th Annual Meeting. Conference Proceedings., IEEE*, vol. 1, pp. 122–123 vol.1, Nov 1997.

[23] C. McKinstrie, S. Radic, and A. Chraplyvy, "Parametric amplifiers driven by two pump waves," *IEEE J. Sel. Top. Quantum Electron.*, vol. 8, pp. 538–547, may 2002.

[24] C. J. McKinstrie and S. Radic, "Phase-sensitive amplification in a fiber," *Opt. Express*, vol. 12, no. 20, p. 4973, 2004.

[25] P. L. Voss, R. Tang, and P. Kumar, "Measurement of the photon statistics and the noise figure of a fiber-optic parametric amplifier," *Opt. Lett.*, vol. 28, p. 549, apr 2003.

[26] K. K. Y. Wong, K. Shimizu, M. E. Marhic, K. Uesaka, G. Kalogerakis, and L. G. Kazovsky, "Continuous-wave fiber optical parametric wavelength converter with +40-dB conversion efficiency and a 3.8-dB noise figure.," *Opt. Lett.*, vol. 28, no. 9, pp. 692–694, 2003.

[27] H. A. Haus and J. A. Mullen, "Quantum Noise in Linear Amplifiers," *Phys. Rev.*, vol. 128, pp. 2407–2413, dec 1962.

[28] Z. Tong, A. Bogris, M. Karlsson, and P. A. Andrekson, "Full characterization of the signal and idler noise figure spectra in single-pumped fiber optical parametric amplifiers.," *Opt. Express*, vol. 18, pp. 2884–93, feb 2010.

[29] C. J. McKinstrie, S. Radic, and M. G. Raymer, "Quantum noise properties of parametric amplifiers driven by two pump waves.," *Opt. Express*, vol. 12, pp. 5037–66, oct 2004.

[30] C. J. McKinstrie, M. Yu, M. G. Raymer, and S. Radic, "Quantum noise properties of parametric processes.," *Opt. Express*, vol. 13, pp. 4986–5012, jun 2005.

[31] P. L. Voss and P. Kumar, "Raman-effect induced noise limits on $\chi^{(3)}$ parametric amplifiers and wavelength converters," *J. Opt. B Quantum Semiclassical Opt.*, vol. 6, pp. S762–S770, aug 2004.

[32] C. J. McKinstrie, S. Radic, R. M. Jopson, and A. Chraplyvy, "Quantum noise limits on optical monitoring with parametric devices," *Opt. Commun.*, vol. 259, no. 1, pp. 309–320, 2006.

[33] Z. Tong, A. Bogris, C. Lundström, C. J. McKinstrie, M. Vasilyev, M. Karlsson, and P. A. Andrekson, "Modeling and measurement of the noise figure of a cascaded non-degenerate phase-sensitive parametric amplifier.," *Opt. Express*, vol. 18, pp. 14820–35, jul 2010.

[34] H. J. McGuinness, M. G. Raymer, C. J. McKinstrie, and S. Radic, "Quantum Frequency Translation of Single-Photon States in a Photonic Crystal Fiber," *Phys. Rev. Lett.*, vol. 105, p. 093604, aug 2010.

[35] M. G. Raymer and K. Srinivasan, "Manipulating the color and shape of single photons," *Phys. Today*, vol. 65, no. 11, p. 32, 2012.

[36] K. Inoue and H. Toba, "Wavelength conversion experiment using fiber four-wave mixing," *IEEE Photonics Technol. Lett.*, vol. 4, pp. 69–72, jan 1992.

[37] D. Méchin, R. Provo, J. D. Harvey, and C. J. McKinstrie, "180-nm wavelength conversion based on Bragg scattering in an optical fiber.," *Opt. Express*, vol. 14, pp. 8995–9, oct 2006.

[38] A. H. Gnauck, R. M. Jopson, C. J. McKinstrie, J. C. Centanni, and S. Radic, "Demonstration of low-noise frequency conversion by bragg scattering in a fiber.," *Opt. Express*, vol. 14, pp. 8989–94, oct 2006.

[39] A. S. Clark, M. J. Collins, A. C. Judge, E. C. Mägi, C. Xiong, and B. J. Eggleton, "Raman scattering effects on correlated photon-pair generation in chalcogenide," *Opt. Express*, vol. 20, p. 16807, jul 2012.

[40] M. J. Collins, A. S. Clark, J. He, D.-Y. Choi, R. J. Williams, A. C. Judge, S. J. Madden, M. J. Withford, M. J. Steel, B. Luther-Davies, C. Xiong, and B. J. Eggleton, "Low Raman-noise correlated photon-pair generation in a dispersion-engineered chalcogenide As_2S_3 planar waveguide.," *Opt. Lett.*, vol. 37, pp. 3393–5, aug 2012.

[41] K. Krupa, A. Tonello, V. V. Kozlov, V. Couderc, P. Di Bin, S. Wabnitz, A. Barthélémy, L. Labonté, and S. Tanzilli, "Bragg-scattering conversion at telecom wavelengths towards the photon counting regime.," *Opt. Express*, vol. 20, pp. 27220–5, nov 2012.

[42] G. Li, N. Bai, N. Zhao, and C. Xia, "Space-division multiplexing: the next frontier in optical communication," *Adv. Opt. Photonics*, vol. 6, p. 413, dec 2014.

[43] R.-J. Essiambre, R. Ryf, N. K. Fontaine, and S. Randel, "Breakthroughs in Photonics 2012: Space-Division Multiplexing in Multimode and Multicore Fibers for High-Capacity Optical Communication," *IEEE Photonics J.*, vol. 5, pp. 0701307–0701307, apr 2013.

[44] D. J. Richardson, J. M. Fini, and L. E. Nelson, "Space-division multiplexing in optical fibres," *Nat. Photonics*, vol. 7, pp. 354–362, apr 2013.

[45] P. M. Krummrich, "Optical amplification and optical filter based signal processing for cost and energy efficient spatial multiplexing," *Opt. Express*, vol. 19, p. 16636, aug 2011.

[46] P. J. Winzer and G. J. Foschini, "MIMO capacities and outage probabilities in spatially multiplexed optical transport systems," *Opt. Express*, vol. 19, p. 16680, aug 2011.

[47] Y. Jung, S.-u. Alam, Z. Li, A. Dhar, D. Giles, I. P. Giles, J. K. Sahu, F. Poletti, L. Grüner-Nielsen, and D. J. Richardson, "First demonstration and detailed characterization of a multimode amplifier for space division multiplexed transmission systems," *Opt. Express*, vol. 19, p. B952, dec 2011.

[48] G. Le Cocq, L. Bigot, A. Le Rouge, M. Bigot-Astruc, P. Sillard, C. Koebele, M. Salsi, and Y. Quiquempois, "Modeling and characterization of a few-mode EDFA supporting four mode groups for mode division multiplexing," *Opt. Express*, vol. 20, p. 27051, nov 2012.

[49] R. Ryf, A. Sierra, R.-J. Essiambre, S. Randel, A. Gnauck, C. A. Bolle, M. Esmaeelpour, P. J. Winzer, R. Delbue, P. Pupalaikis, A. Sureka, D. Peckham, A. McCurdy, and R. Lingle, "Mode-Equalized Distributed Raman Amplification in 137-km Few-Mode Fiber," in *37th Eur. Conf. Expo. Opt. Commun.*, (Washington, D.C.), p. Th.13.K.5, OSA, 2011.

[50] Y. Weng, T. Wang, and Z. Pan, "Optimization of Mode-Dependent Gain Efficiency based on Intermodal Raman Scattering for Few-Mode Distributed Raman Amplifier," in *Conf. Lasers Electro-Optics*, (Washington, D.C.), p. SW1P.5, OSA, 2016.

[51] J. Zhou, "An analytical approach for gain optimization in multimode fiber Raman amplifiers," *Opt. Express*, vol. 22, no. 18, p. 21393, 2014.

[52] R. Ryf, M. a. Mestre, S. Randel, C. Schmidt, A. H. Gnauck, R.-J. Essiambre, P. J. Winzer, R. Delbue, P. Pupalaikis, A. Sureka, Y. Sun, X. Jiang, D. W. Peckham, A. McCurdy, and R. Lingle, "Mode-Multiplexed Transmission Over a 209-km DGD-Compensated Hybrid Few-Mode Fiber Span," *IEEE Photonics Technol. Lett.*, vol. 24, no. 21, pp. 1965–1968, 2012.

[53] P. Steinvurzel, J. Demas, B. Tai, Y. Chen, L. Yan, and S. Ramachandran, "Broadband parametric wavelength conversion at 1 μm with large mode area fibers," *Opt. Lett.*, vol. 39, no. 4, p. 743, 2014.

[54] A. Farsi, S. Clemmen, S. Ramelow, and A. L. Gaeta, "Low-Noise Quantum Frequency Translation of Single Photons," in *CLEO Tech. Dig.*, p. FM3A.4, 2015.

[55] D. J. Griffiths, *Introduction to Electrodynamics*. Pearson, 3 ed., 2008.

[56] G. P. Agrawal, *Nonlinear Fiber Optics*. Elsevier, 4 ed., 2006.

[57] K. Rottwitt and P. Tidemand-Lichtenberg, *Nonlinear Optics - Principles and Applications*. CRC Press, first ed., 2015.

[58] S. Afshar V and T. M. Monro, "A full vectorial model for pulse propagation in emerging waveguides with subwavelength structures part I: Kerr nonlinearity.," *Opt. Express*, vol. 17, pp. 2298–318, feb 2009.

[59] R. Song, J. Zhu, and X. Zhang, "Full-vectorial modal analysis for circular optical waveguides based on the multidomain Chebyshev pseudospectral method," *J. Opt. Soc. Am. B*, vol. 27, no. 9, p. 1722, 2010.

[60] G. B. Arfken and H. J. Weber, *Mathematical Methods for Physicists*. Elsevier, sixth ed., 2005.

[61] K. Okamoto, *Fundamentals of Opticals Waveguides*. Elsevier, second ed., 2006.

[62] J. Demas, P. Steinvurzel, B. Tai, L. Rishøj, Y. Chen, and S. Ramachandran, "Intermodal nonlinear mixing with Bessel beams in optical fiber," *Optica*, vol. 2, no. 1, p. 14, 2015.

[63] A. W. Snyder and J. D. Love, *Optical Waveguide Theory*. Boston, MA: Springer US, 1984.

[64] M. D. Turner, T. M. Monro, and S. Afshar V, "A full vectorial model for pulse propagation in emerging waveguides with subwavelength structures part II : Stimulated Raman Scattering," *Opt. Express*, vol. 17, no. 14, pp. 11565–11581, 2009.

[65] M. Kolesik and J. V. Moloney, "Nonlinear optical pulse propagation simulation: From Maxwell's to unidirectional equations," *Phys. Rev. E*, vol. 70, p. 036604, sep 2004.

[66] F. Poletti and P. Horak, "Description of ultrashort pulse propagation in multimode optical fibers," *J. Opt. Soc. Am. B*, vol. 25, p. 1645, oct 2008.

[67] F. Poletti and P. Horak, "Dynamics of femtosecond supercontinuum generation in multimode fibers," *Opt. Express*, vol. 17, p. 6134, apr 2009.

[68] C. Antonelli, M. Shtaif, and A. Mecozzi, "Modeling of Nonlinear Propagation in Space-Division Multiplexed Fiber-Optic Transmission," *J. Light. Technol.*, vol. 34, no. 1, pp. 36–54, 2016.

[69] C. Antonelli, A. Mecozzi, and M. Shtaif, "Raman amplification in multimode fibers with random mode coupling," *Opt. Lett.*, vol. 38, no. 8, p. 1188, 2013.

[70] D. Hollenbeck and C. D. Cantrell, "Multiple-vibrational-mode model for fiber-optic Raman gain spectrum and response function," *J. Opt. Soc. Am. B*, vol. 19, no. 12, p. 2886, 2002.

[71] R. H. Stolen and E. P. Ippen, "Raman gain in glass optical waveguides," *Appl. Phys. Lett.*, vol. 22, no. 6, p. 276, 1973.

[72] S. M. M. Friis, K. Rottwitt, and C. J. McKinstrie, "Raman and loss induced quantum noise in depleted fiber optical parametric amplifiers," *Opt. Express*, vol. 21, p. 29320, Nov. 2013.

[73] S. M. M. Friis, L. Mejling, and K. Rottwitt, "Effects of Raman scattering and attenuation in silica fiber-based parametric frequency conversion," *in preparation for Opt. Express*, 2016.

[74] S. M. M. Friis, K. Rottwitt, and C. J. McKinstrie, "Quantum and Raman Noise in a Depleted Fiber Optical Parametric Amplifier," in *Nonlinear Opt.*, (Washington, D.C.), p. NW4A.06, OSA, 2013.

[75] S. M. M. Friis, L. Mejling, M. A. Usuga, A. T. Pedersen, C. J. McKinstrie, and K. Rottwitt, "Effects of Raman scattering in quantum state-preserving frequency conversion," in *CLEO 2014*, (Washington, D.C.), p. STu2I.2, OSA, 2014.

[76] S. M. M. Friis, L. Mejling, and K. K. Rottwitt, "Reducing Raman Noise in Parametric Frequency Conversion by Varying the Input Pump Power," in *Adv. Photonics*, (Washington, D.C.), p. NW4A.6, OSA, 2014.

[77] C. M. Caves, "Quantum limits on noise in linear amplifiers," *Phys. Rev. D*, vol. 26, pp. 1817–1839, oct 1982.

[78] C. J. McKinstrie and J. P. Gordon, "Field Fluctuations Produced by Parametric Processes in Fibers," *IEEE J. Sel. Top. Quantum Electron.*, vol. 18, pp. 958–969, mar 2012.

[79] C. J. McKinstrie, J. D. Harvey, S. Radic, and M. G. Raymer, "Translation of quantum states by four-wave mixing in fibers.," *Opt. Express*, vol. 13, pp. 9131–42, oct 2005.

[80] C. J. McKinstrie, M. G. Raymer, S. Radic, and M. Vasilyev, "Quantum mechanics of phase-sensitive amplification in a fiber," *Opt. Commun.*, vol. 257, pp. 146–163, jan 2006.

[81] P. L. Voss, K. G. Köprülü, and P. Kumar, "Raman-noise-induced quantum limits for $\chi^{(3)}$ nondegenerate phase-sensitive amplification and quadrature squeezing," *J. Opt. B Quantum Semiclassical Opt.*, vol. 23, no. 4, pp. 598–610, 2006.

[82] Zhi Tong, C. Lundström, P. A. Andrekson, M. Karlsson, and A. Bogris, "Ultralow Noise, Broadband Phase-Sensitive Optical Amplifiers, and Their Applications," *IEEE J. Sel. Top. Quantum Electron.*, vol. 18, no. 2, pp. 1016–1032, 2012.

[83] J. A. Levenson, P. Grangier, I. Abram, and T. Rivera, "Reduction of quantum noise in optical parametric amplification," *J. Opt. Soc. Am. B*, vol. 10, p. 2233, nov 1993.

[84] R. Tang, P. L. Voss, J. Lasri, P. Devgan, and P. Kumar, "Noise-figure limit of fiber-optical parametric amplifiers and wavelength converters: experimental investigation," *Opt. Lett.*, vol. 29, p. 2372, oct 2004.

[85] Z. Tong, C. Lundström, P. A. Andrekson, C. J. McKinstrie, M. Karlsson, D. J. Blessing, E. Tipsuwannakul, B. J. Puttnam, H. Toda, and L. Gru, "Towards ultrasensitive optical links enabled by low-noise phase-sensitive amplifiers," *Nat. Photonics*, vol. 5, no. July, pp. 430–436, 2011.

[86] C. C. Gerry and P. L. Knight, *Introductory Quantum Optics*. Cambridge, 2005.

[87] K. Rottwitt, J. Bromage, A. Stentz, Lufeng Leng, M. Lines, and H. Smith, "Scaling of the raman gain coefficient: applications to germanosilicate fibers," *J. Light. Technol.*, vol. 21, no. 7, pp. 1652–1662, 2003.

[88] H. Kidorf, K. Rottwitt, M. Nissov, M. Ma, and E. Rabarijaona, "Pump interactions in a 100-nm bandwidth Raman amplifier," *IEEE Photonics Technol. Lett.*, vol. 11, no. 5, pp. 530–532, 1999.

[89] Z. Tong, A. Bogris, M. Karlsson, and P. A. Andrekson, "Raman-Induced Asymmetric Pump Noise Transfer in Fiber-Optical Parametric Amplifiers," *IEEE Photonics Technol. Lett.*, vol. 22, pp. 386–388, mar 2010.

[90] K. Croussore and G. Li, "Phase and Amplitude Regeneration of Differential Phase-Shift Keyed Signals Using Phase-Sensitive Amplification," *IEEE J. Sel. Top. Quantum Electron.*, vol. 14, no. 3, pp. 648–658, 2008.

[91] M. Sköld, J. Yang, H. Sunnerud, M. Karlsson, S. Oda, and P. A. Andrekson, "Constellation diagram analysis of DPSK signal regeneration in a saturated parametric amplifier," *Opt. Express*, vol. 16, no. 9, p. 5974, 2008.

[92] C. Peucheret, M. Lorenzen, J. Seoane, D. Noordegraaf, C. Nielsen, L. Gruner-Nielsen, and K. Rottwitt, "Amplitude Regeneration of RZ-DPSK Signals in Single-Pump Fiber-Optic Parametric Amplifiers," *IEEE Photonics Technol. Lett.*, vol. 21, pp. 872–874, jul 2009.

[93] M. Matsumoto, "Fiber-Based All-Optical Signal Regeneration," *IEEE J. Sel. Top. Quantum Electron.*, vol. 18, no. 2, pp. 738–752, 2012.

[94] S. M. Friis, Y. Jung, I. Begleris, P. Horak, K. Rottwitt, P. Petropoulos, D. J. Richardson, and F. Parmigiani, "Detailed Phase Matching Characterization of Inter-Modal Four-Wave Mixing in a Two-Mode Fiber," in *Conf. Lasers Electro-Optics*, p. JTu5A.49, OSA, 2016.

[95] K. K. Rottwitt, K. Nielsen, S. M. Friis, and M. A. Castaneda, "Challenges in Higher Order Mode Fiber Raman Amplifiers," in *Opt. Fiber Commun. Conf.*, p. Tu3C.6, OSA, 2015.

[96] S. M. M. Friis and K. Rottwitt, "Noise contributions of linear pump mode coupling in few-moded Raman fiber amplifiers," *submitted to Journal of Lightwave Technology*, 2016.

[97] E. N. Christensen, J. G. Koefoed, S. M. M. Friis, M. A. Usuga, and K. Rottwitt, "Experimental characterization of Raman overlaps between mode-groups," *submitted, revised, and re-submitted to Scientific Reports*, 2016.

[98] N. Bai, E. Ip, Y.-k. Huang, E. Mateo, F. Yaman, M.-J. Li, S. Bickham, S. Ten, J. Liñares, C. Montero, V. Moreno, X. Prieto, V. Tse, K. Man Chung, A. P. T. Lau, H.-y. Tam, C. Lu, Y. Luo, G.-d. Peng, G. Li, and T. Wang, "Mode-division multiplexed transmission with inline few-mode fiber amplifier," *Opt. Express*, vol. 20, p. 2668, jan 2012.

[99] V. Sleiffer, Y. Jung, V. Veljanovski, R. van Uden, M. Kuschnerov, H. Chen, B. Inan, L. G. Nielsen, Y. Sun, D. Richardson, S. Alam, F. Poletti, J. Sahu, A. Dhar, A. Koonen, B. Corbett, R. Winfield, A. Ellis, and H. de Waardt, "737 Tb/s (96 x 3 x 256-Gb/s) mode-division-multiplexed DP-16QAM transmission with inline MM-EDFA," *Opt. Express*, vol. 20, no. 26, p. B428, 2012.

[100] Q. Kang, E. Lim, Y. Jun, X. Jin, F. P. Payne, S. Alam, and D. J. Richardson, "Gain Equalization of a Six-Mode-Group Ring Core Multimode EDFA," in *Eur. Conf. Exhib. Opt. Commun.*, 2014.

[101] R. Ryf, R.-J. Essiambre, J. von Hoyningen-Huene, and P. J. Winzer, "Analysis of Mode-Dependent Gain in Raman Amplified Few-Mode Fiber," 2012.

[102] Y. Weng, T. Wang, and Z. Pan, "Optimization of Mode-Dependent Gain Efficiency based on Intermodal Raman Scattering for Few-Mode Distributed Raman Amplifier," in *Conf. Lasers Electro-Optics*, (Washington, D.C.), p. SW1P.5, OSA, 2016.

[103] R. Ryf, S. Randel, A. H. Gnauck, C. Bolle, A. Sierra, S. Mumtaz, M. Esmaeelpour, E. C. Burrows, R.-J. Essiambre, P. J. Winzer, D. W. Peckham, A. H. McCurdy, and R. Lingle, "Mode-division multiplexing over 96 km of few-mode fiber using coherent 6×6 MIMO processing," *J. Light. Technol.*, vol. 30, no. 4, pp. 521–531, 2012.

[104] L. Grüner-nielsen, Y. Sun, J. W. Nicholson, D. Jakobsen, K. G. Jespersen, R. Lingle, and B. Pálsdóttir, "Few Mode Transmission Fiber With Low DGD , Low Mode Coupling, and Low Loss," *J. Light. Technol.*, vol. 30, no. 23, pp. 3693–3698, 2012.

[105] P. J. Winzer, A. H. Gnauck, A. Konczykowska, F. Jorge, and J.-Y. Dupuy, "Penalties from in-band crosstalk for advanced optical modulation formats," in *37th European Conference and Exposition on Optical Communications*, p. Tu.5.B.7, Optical Society of America, 2011.

[106] B. Ung, P. Vaity, L. Wang, Y. Messaddeq, L. a. Rusch, and S. LaRochelle, "Few-mode fiber with inverse-parabolic graded-index profile for transmission of OAM-carrying modes," *Opt. Express*, vol. 22, no. 15, p. 18044, 2014.

[107] K.-P. Ho and J. M. Kahn, "Mode Coupling and its Impact on Spatially Multiplexed Systems," in *Opt. Fiber Telecommun. Vol. VIB, Sixth Ed. Syst. Networks*, ch. 11, Academic, 6th ed., 2013.

[108] K. Jespersen, Z. Li, B. Pálsdóttir, F. Poletti, and J. W. Nicholson, "Measuring Distributed Mode Scattering in Long , Few- Moded Fibers," in *OFC Tech. Dig.*, p. OTh31.4, 2012.

[109] K. P. Ho and J. M. Kahn, "Mode-dependent loss and gain : statistics and effect on mode-division multiplexing," *Opt. Express*, vol. 19, no. 17, pp. 16612–16635, 2011.

[110] K. P. Ho and J. M. Kahn, "Statistics of group delays in multimode fiber with strong mode coupling," *J. Light. Technol.*, vol. 29, no. 21, pp. 3119–3128, 2011.

[111] K. P. Ho and J. M. Kahn, "Linear Propagation Effects in Mode-Division Multiplexing Systems," *J. Light. Technol.*, vol. 32, pp. 614–628, Feb. 2014.

[112] C. Headley and G. P. Agrawal, "Unified description of ultrafast stimulated Raman scattering in optical fibers," *J. Opt. Soc. Am. B*, vol. 13, p. 2170, oct 1996.

[113] N. K. Fontaine, R. Ryf, M. a. Mestre, B. Guan, X. Palou, S. Randel, Y. Sun, L. Grüner-Nielsen, R. V. Jensen, and R. Lingle, "Characterization of Space-Division Multiplexing Systems using a Swept-Wavelength Interferometer," in *Opt. Fiber Commun. Conf. Fiber Opt. Eng. Conf. 2013*, no. c, (Washington, D.C.), p. OW1K.2, OSA, 2013.

[114] Y. Xiao, R.-J. Essiambre, M. Desgroseilliers, A. M. Tulino, R. Ryf, S. Mumtaz, and G. P. Agrawal, "Theory of intermodal four-wave mixing with random linear mode coupling in few-mode fibers," *Opt. Express*, vol. 22, no. 26, p. 32039, 2014.

[115] A. Mecozzi, C. Antonelli, and M. Shtaif, "Nonlinear propagation in multi-mode fibers in the strong coupling regime," *Opt. Express*, vol. 20, no. 11, p. 11673, 2012.

[116] C. Antonelli, A. Mecozzi, M. Shtaif, and P. J. Winzer, "Random coupling between groups of degenerate fiber modes in mode multiplexed transmission," *Opt. Express*, vol. 21, no. 8, p. 9484, 2013.

[117] L. Palmieri, "Coupling mechanism in multimode fibers," in *Proc. SPIE*, vol. 9009, p. 90090G, Dec. 2013.

[118] J. W. Nicholson, A. D. Yablon, S. Ramachandran, and S. Ghalmi, "Spatially and spectrally resolved imaging of modal content in large-mode-area fibers," *Opt. Express*, vol. 16, no. 10, pp. 7233–7243, 2008.

[119] L. Blanco Castañeda, V. Arunachalam, and S. Dharmaraja, "Some Continuous Distributions," in *Introd. to Probab. Stoch. Process. with Appl.*, ch. 4, pp. 145–189, Wiley, 2012.

[120] K. Rottwitt and A. J. Stentz, "Raman Amplification in Lightwave Communication Systems," in *Opt. Fiber Telecommun. IV A Components* (I. Kaminow and T. Li, eds.), ch. 5, pp. 213–257, Academic, 2002.

[121] E. Ip, M.-j. Li, Y.-K. Huang, A. Tanaka, E. Mateo, W. Wood, J. Hu, Y. Yano, and K. Koreshkov, "146λx6x19-Gbaud Wavelength- and Mode-Division Multiplexed Transmission over 10x50-km Spans of Few-Mode Fiber with a Gain-Equalized Few-Mode EDFA," in *Opt. Fiber Commun. Conf. Fiber Opt. Eng. Conf. 2013*, (Washington, D.C.), p. PDP5A.2, OSA, 2013.

[122] E. L. Lim, Y. Jung, Q. Kang, T. C. May-Smith, N. H. L. Wong, R. Standish, F. Poletti, J. K. Sahu, S. Alam, and D. J. Richardson, "First Demonstration of Cladding Pumped Few-moded EDFA for Mode Division Multiplexed Transmission," in *Opt. Fiber Commun. Conf.*, (Washington, D.C.), p. M2J.2, OSA, 2014.

[123] B. M. Trabold, A. Abdolvand, T. G. Euser, A. M. Walser, and P. S. Russell, "Amplification of higher-order modes by stimulated Raman scattering in H_2-filled hollow-core photonic crystal fiber," *Opt. Lett.*, vol. 38, p. 600, mar 2013.

[124] K. Rottwitt and J. Povlsen, "Analyzing the fundamental properties of Raman amplification in optical fibers," *J. Light. Technol.*, vol. 23, pp. 3597–3605, nov 2005.

[125] S. Savin, M. J. F. Digonnet, G. S. Kino, and H. J. Shaw, "Tunable mechanically induced long-period fiber gratings," *Opt. Lett.*, vol. 25, p. 710, may 2000.

[126] R. H. Stolen, J. E. Bjorkholm, and A. Ashkin, "Phase-matched three-wave mixing in silica fiber optical waveguides," *Appl. Phys. Lett.*, vol. 24, no. 7, p. 308, 1974.

[127] R.-J. Essiambre, M. a. Mestre, R. Ryf, A. H. Gnauck, R. W. Tkach, A. R. Chraplyvy, Y. Sun, X. Jiang, and R. Lingle, "Experimental Investigation of Inter-Modal Four-Wave Mixing in Few-Mode Fibers," *IEEE Photonics Technol. Lett.*, vol. 25, pp. 539–542, mar 2013.

[128] R.-J. Essiambre, M. A. Mestre, R. Ryf, A. H. Gnauck, R. W. Tkach, A. R. Chraplyvy, Y. Sun, X. Jiang, and R. Lingle, "Experimental observation of intermodal cross-phase modulation in few-mode fibers," *IEEE Photonics Technol. Lett.*, vol. 25, no. 6, pp. 535–538, 2013.

[129] M. Schnack, T. Hellwig, M. Brinkmann, and C. Fallnich, "Ultrafast two-color all-optical transverse mode conversion in a graded-index fiber," *Opt. Lett.*, vol. 40, p. 4675, oct 2015.

[130] S. M. M. Friis, Y. Jung, I. Begleris, P. Horak, K. Rottwitt, P. Petropoulos, D. J. Richardson, and F. Parmigiani, "Characterization of inter-modal four-wave mixing in a two-mode fiber," *in preparation for Opt. Express*, Aug 2016.

[131] F. Parmigiani, Y. Jung, S. M. M. Friis, Q. Kang, I. Begleris, P. Horak, K. Rottwitt, P. Petropoulos, and D. J. Richardson, "Study of Inter-Modal Four Wave Mixing in Two Few-Mode Fibres with Different Phase Matching Properties," in *European Conf. on Optical Communication*, p. Tu2D.4, 2016.